The Properties of Super Star Clusters in A Sample of Starburst Galaxies

by

Kelsey Johnson

B.A., Carleton College, 1995

M.S., University of Colorado, 1997

A thesis submitted to the

Faculty of the Graduate School of the

University of Colorado in partial fulfillment

of the requirements for the degree of

Doctor of Philosophy

Department of Astrophysical and Planetary Sciences

2001

This thesis entitled:
The Properties of Super Star Clusters in A Sample of Starburst Galaxies
written by Kelsey Johnson
has been approved for the Department of Astrophysical and Planetary Sciences

Prof. Peter Conti

Prof. John Bally

Prof. Erica Ellingson

Prof. J. Michael Shull

Date

The final copy of this thesis has been examined by the signatories, and we find that both the content and the form meet acceptable presentation standards of scholarly work in the above mentioned discipline.

Johnson, Kelsey (Ph.D., Astrophysics)

The Properties of Super Star Clusters in A Sample of Starburst Galaxies

Thesis directed by Prof. Peter Conti

ABSTRACT

"Super star clusters" are the most massive extreme in the continuum of young star clusters. In this thesis, I examine the properties of such super star clusters in a sample of starburst galaxies with space and ground-based observations and in the optical, mid-infrared, and radio regimes. Using optical photometry, I estimate the ages and masses, as well as construct luminosity functions for the super star cluster systems. Additional Hα observations allow me to place tighter constraints on the burst ages and trace very recent star formation. The super star clusters detected in these galaxies typically have estimated ages $\lesssim 10$ Myr, masses of $\sim 10^{3-6}$ $M_\odot$, and luminosity functions consistent with other super star cluster systems with a slope of $\alpha \approx -2$ ($\phi(L) \propto L^\alpha$).

Next I discuss an even earlier stage of massive star cluster evolution, when super star clusters are still embedded in their birth material. I overview the discovery of "ultra dense H II regions" (UDH IIs) with radio and mid-infrared observations. From the radio observations, I calculate the electron densities, radii, and number of ionizing photons (and therefore number of embedded massive stars). The mid-infrared observations confirm the presence of hot dust cocoons surrounding these objects. These embedded clusters account for at least $\sim 60\%$ of the mid- to far-infrared flux of He 2-10. I also discuss the impact of UDH IIs on the radio to far-infrared flux ratio.

Finally, I present a sample of 35 embedded star formation regions (ranging from the size of small OB-associations to super star clusters) serendipitously detected in nearby galaxies. This sample of objects begins to fill in the continuum of cluster masses between individual UCH II regions and the embedded massive clusters.

Acknowledgements

Perhaps the greatest irony of a thesis text is that the pages most likely to be read are those of the acknowledgments. The weight of these pages is all the heavier because it is precisely the people most likely to read them who most deserve to acknowledged, and I will undoubtedly realize as soon as this thesis has been printed that several important people have been inadvertently left out. My sincere apologies in advance — to everyone who has provided me with kind words, a welcome ear, new ideas, useful criticism, or their invaluable time, I am truly indebted.

A long, and sometimes complicated, path of people and events winds back through the years which have brought me to this academic rite of passage. Most of these events were out of my control, and most of these people I met by chance. The importance of serendipity has not been lost on me, and I must acknowledge that I have been fantastically lucky. Here I will roughly outline, in forward chronological order, the people who come to mind as having a large impact on my academic career.

As an undergraduate at Carleton College, I was surrounded by caring faculty who didn't let me fall through the cracks – most importantly Dr. Cindy Blaha and Dr. Bruce Thomas. My summer job working with Cindy was my springboard into the coming years. This summer job in turn enabled me to work with Dr. Phil Massey in Arizona the following summer — again, a lucky chance which has had a profound impact on my life since that time. Indeed, I have looked to Phil for his infallible advice on both academic issues and those related to real life since that summer. I believe that this work with Phil played a significant role in Dr. Peter Conti recruiting me as a graduate student for the University of Colorado (although I don't think either of them would admit to this).

Peter has provided me with unwavering support during my time as a graduate student, and perhaps most importantly has allowed me room to grow and explore new ideas (many of which never came to fruition). I only hope that someday I have a fraction of his intuition and patience. Along with Peter, Dr. Katy Garmany also had a large role in my academic advising and went significantly beyond the "job description" many times. The unofficial title she held at the University of Colorado of "Graduate Student Godmother" was certainly well deserved.

Upon arriving in graduate school, I briefly overlapped with Peter's previous graduate student, Dr. Margaret Hanson. Margaret is one of the most dynamic women I have had the pleasure to know in astrophysics, and she has served as my primary role model through the years. My officemate, Tanya Ramond, has also been an important part of my graduate life. We have commiserated on many occasions, but have also shared many happy times. My office sometimes seems like a second home, which hasn't been so bad because I've had such a great officemate.

Throughout my graduate student years I have also received a great deal of guidance from afar — Dr. Bill Vacca has generously offered his time as a scientific advisor. He has been exceedingly patient and I count him as one of the few people I am comfortable asking "stupid" questions. As a measure of his conscientious replies to my queries, my email folder entitled "Bill" has more entries than any other.

My work with Peter also led me to meet another valued collaborator and friend, Dr. Chip Kobulnicky. With another nod to serendipity, it was my first interaction with Chip (I needed to use one of his published images in a talk) which led us to discover "ultradense HII regions". These objects form a major part of this thesis and have led to numerous other opportunities for which I am grateful.

Throughout graduate school I have been fortunate to have wonderful support structure among the graduate students. I often question whether I would have survived my first two years in the program without my classmates Sebastian Heinz, Aaron Lewis, and Kevin McLin.

In particular, Kevin's generosity stands out as I recall those years — on several occasions he would do things like spontaneously bring me dinner when I didn't have time to go home myself. He also kept me from completely burying myself in work by coaxing me out for hikes in the mountains. Along with my classmates, Marc DeRosa (DeRosa) and Marc Swisdak (Swisdak) were a fundamental part of my support network. Because DeRosa had his office only a few yards away from my own, he was often the recipient of random questions (both technical and scientific). Swisdak was always willing to think through particularly vexing questions which I wasn't sure how to approach on my own. I greatly admire Swisdak's character for his patience, work ethic, fairness, and compassion, and hold his character up as a standard to which I aspire.

On a non-academic note, the Womprats and Nerfherders (the department's intramural ultimate teams), have provided an invaluable outlet for stress and a wonderful occasion to socialize and get at least a little physical activity in my schedule. These teams even put up with me as captain for several seasons, and it was a great pleasure to be a part of these teams as we evolved from barely fielding a team of beginners to having over thirty players on two teams and winning championships.

Finally, and most importantly, I come to my husband, Rémy Indebetouw. Somehow he stands by me when I am at my worst as well as celebrating with me when I am at my best. He has kept me going on many occasions when I was ready to give up and has diligently protested my complaints of not being smart enough, strong enough, or good enough. Throughout the years we have been together, his influence on my life has helped me grow into a better person, and his presence in my life gives me a sense of peace.

Contents

Chapter

Appendix

Tables

Table

Figures

Figure

Chapter 1

Introduction

“My purpose is to tell of bodies which have been transformed into shapes of a different kind. You heavenly powers, since you were responsible for those changes, as for all else, look favourably on my attempts, and spin an unbroken thread of verse, from the earliest beginnings of the world, down to my own times.”

— Ovid (*Metamorphoses*)

The universe is host to a multitude of physical processes, and an equally diverse collection of material elements, which are continually interacting and evolving. Throughout this cosmic dance, generations of stars have been born, died, and created anew from the ashes. This cycle of life continues even today in our own galaxy, the Milky Way. As we look further and further into the depths of the universe, we see that stars have been forming almost since the beginning of time. As their light crosses the vast expanse of time and space, it carries along encrypted information that we have learned how to decode, and in this way have gained much of our understanding of the universe.

Because this thesis is primarily based on observations, I will begin by providing a basic explanation of how astronomers decode this light from the universe in § 1.1, which is included for the benefit of readers outside of the field. In the remainder of this chapter, I will give a broad overview of topics closely related to the subject of this thesis. The nature of starburst galaxies and their impact throughout the universe is discussed in § 1.2. The state of knowledge about super star clusters, which are typically formed in starburst episodes, is discussed in § 1.3.

1.1 Interpreting the Light From Stars

In nature's endless variety, even stars themselves have a rich family of sub-types and species — in fact, there is literally a rainbow of stellar types. One can think of fire as an analogy, a flame is blue at its hottest and red where it is cool. Likewise, stars have a continuum of colors, with the hottest being blue and the coolest red. For most of a star's life (known as the "main sequence") [1] , its color not only tells us about its temperature, but also about its most fundamental property, mass. The lives of stars are deterministic in this way — the mass with which a star is born virtually dictates the rest of its life (with a few more subtle effects intentionally neglected here). The most massive stars live fast and die young: the more massive a star is, the faster it consumes its fuel and the brighter it burns. While our cool and yellow Sun will live some 10 billion years, by contrast a hot blue star will die at the young age (by astronomical standards) of only a few million years. For this reason, if we see a bright blue star on the main sequence, we know it has to be young.

In this way, we can also use color to learn about collections of stars, such as galaxies. Even if we cannot resolve the individual stars themselves, the medley of stellar light coming from a galaxy tells us something about the stars it contains. Even more can be learned from light if we spread it out into a rainbow or "spectrum". Each type of star (and other astrophysical objects as well) has a unique fingerprint which we can identify in its spectrum. These are the main tools astronomers use to understand the universe with observations. For example, a galaxy with an unusually blue color must have an abundance of blue stars [2] . Since these stars must be young, the galaxy's blue color indicates that it must have recently undergone a tremendous spurt of star formation. These are the galaxies which we call "starbursts".

---

[1] As a star nears the end of its life, it enters the "post main sequence". During post main sequence evolution, a star's color does not directly reflect its mass.

[2] A reader familiar with the field will note that I am neglecting the class of starburst galaxies which are luminous in the infrared due to tremendous amounts of dust which reprocesses the light from the hot blue stars.

1.2 Starburst Galaxies

It has been over 30 years since Sargent & Searle (1970) noted that certain galaxies are undergoing intense episodes of star formation. This extraordinary mode of star formation has come to be know as the starburst phenomenon. The precise definition of a "starburst galaxy" is notoriously ambiguous, and I will not attempt to remedy this situation here. The standard definition one might hear over coffee with an astronomer is something like, "A galaxy which is forming stars at such a rapid rate that the material available to form stars would be used up in a time short compared to the lifetime of the galaxy." Again, ambiguous.

It is perhaps more useful to define what *isn't* a starburst galaxy as, "a galaxy undergoing a normal (or less than normal) rate per unit area of star formation." In this case, "normal" means something like $0.001 - 0.01$ $M_\odot$ yr^{-1} kpc^{-2} (1 pc$= 3.09 \times 10^{18}$ cm), while a typical starburst might have a star formation rate > 1 $M_\odot$ yr^{-1} kpc^{-2} (and there are galaxies with a range of star formation rates between these values). The result of this vigorous star formation in starburst galaxies is an unusually large number of young, bright, massive stars present in the host galaxy at the same time. In practice, this means that starbursts tend to be extremely bright and blue objects, and much of the spectral energy distribution is dominated by the light from massive stars.

While some of the most spectacular starbursts encompass an entire galaxy (a global burst), more commonly regions in a galaxy are bursting (such as a nuclear starburst), while the rest of the galaxy is relatively dormant. This issue only exacerbates the problem of defining a "starburst galaxy", and the situation is quite muddled in the literature. However, if it is the starburst *phenomenon* we wish to study, both large- and small-scale events are of interest. Moreover, even global starbursts have largely been resolved into clusters of bright young stars, a topic to which I will return at length. In this thesis, I will generally refer to starburst "regions", which are typically (but not always) part of a larger starburst event in the galaxies which I discuss.

Starburst galaxies, and the extreme massive star birth events they host, have been an important aspect of star formation throughout the history of the universe. This mode of star formation is so important that, according to Heckman (1998), in the local universe roughly a quarter of all massive stars have been formed in only a small number of starburst galaxies (M82, NGC 253, M83, and NGC 4945). Thus, if we wish to study the formation and evolution of massive stars, starburst galaxies provide an excellent opportunity.

Massive stars themselves play a major role in the dynamical evolution of galaxies: they are responsible for the ionization of the interstellar medium, their stellar winds and supernovae are major sources of mechanical energy, their ultraviolet radiation powers far-infrared luminosities through the heating of dust, and they are a main driver of chemical evolution in the universe through their end stages (with strong stellar winds and supernovae). The resulting metal-enriched outflows and ionizing radiation from massive stars can have a significant impact on the intergalactic medium.

1.2.1 Relevance of Starburst Galaxies to the Early Universe

In the more distant universe, a large number of star forming galaxies have been discovered at redshifts [3] of $z > 3$ (e.g., Steidel et al. 1996). For these high-z galaxies, the ultraviolet (UV) spectrum is redshifted into the optical regime. Integrated spectra of these galaxies indicate the presence of substantial numbers of massive stars, and the overall spectral morphology of these high-z systems is similar to nearby starburst galaxies (e.g., Conti et al. 1996). Hibbard & Vacca (1997) have simulated photometric observations of starburst galaxies at high redshift using local starburst galaxies as templates. They found a strong similarity in spatial morphology, star formation rates, and spectral energy distributions between nearby starburst galaxies and the high-z objects seen in the Hubble Deep Field (Williams et al. 1996), concluding that nearby starbursts are local analogs to the high-z galaxies.

Galaxy mergers, and their resulting starbursts, may be one of the basic building blocks

---

[3] Redshift is a measure of how fast an object (in this case a galaxy) is moving away from us. The expansion of the universe leads implies that the farther away a galaxy is, the faster its relative velocity. Because of this, we can use an object's velocity (or redshift) to obtain a distance.

of structure formation in the universe; in hierarchical models of structure formation, mergers of smaller structures create the massive, elliptical galaxies we observe in the local universe today (e.g., Baron & White 1987). There is growing support in the literature for the idea that merging galaxy systems, and the resulting starburst episodes, had a significant role in the high-redshift ($z > 3$) universe. In their survey of high-redshift radio galaxies, van Breugel et al. (1998) found that the visual morphologies of these systems exhibited substructure in the form of multiple components ~ 10 kpc in size. They concluded that these giant elliptical galaxies were likely formed from the merging of smaller stellar systems. There is also evidence that the implied star formation rates Lyman break galaxies at $z \sim 3$ can be accounted for by the frequency of collision-induced starbursts (Kolatt et al. 1999; Hibbard & Vacca 1997; Lowenthal et al. 1997). The semi-analytical models of galaxy collisions and tidal interactions of Balland et al. (1998) illustrate how both spiral and elliptical galaxies can be created by different types of tidal collisions and can determine the morphologies of galaxies we see at the present epoch. Therefore, at earlier times in the universe, the starburst phenomenon in interacting galaxies likely had a far more dominant role than we observe in the local universe.

Starburst episodes may also play a role in the reionization of the universe at $z > 5$ (Madau & Shull 1996; Madau et al. 1999, and references therein). Furthermore, metals produced and expelled by massive stars in these galaxies may provide an explanation for the heavy element abundances observed in Lyα clouds (e.g., Cowie et al. 1995; Johnson et al. 2000). Therefore, in order to understand the general evolution of matter in the universe, understanding the origin and nature of massive star formation in starburst episodes is of great importance.

1.2.2 Wolf-Rayet Galaxies

Before discussing Wolf-Rayet galaxies, we must first discuss Wolf-Rayet (WR) stars. WR stars are the descendents of the most massive stars (Maeder & Conti 1994). These stars are at the end point of their evolution and show the products of nuclear processing in their spectra due to mass loss and mixing processes. WR stars have extremely strong and dense radiatively driven stellar winds which give rise to broad emission lines of helium and nitrogen (in WN-type Wolf-Rayet stars) or helium, carbon, and oxygen (in WC-type Wolf-Rayet stars). Because WR stars evolve from the most massive stars, this phase of the star's life cycle happens very quickly after the onset of a starbirth event; 3-6 Myr after a burst of star formation, the massive stars will evolve into WR stars.

Wolf-Rayet Galaxies (WR Galaxies) are a subset of starburst galaxies that have such a significant population of Wolf-Rayet stars that the WR star spectral features show up in the integrated spectrum of the galaxy. In particular, WR galaxies are typically classified by the presence of broad He II $\lambda 4686$ emission in their integrated spectra (Conti 1991). Typically WR galaxies are also "emission line galaxies", which also show nebular emission lines in their integrated spectra due to significant numbers of O-type stars. The resulting spectra are often similar to that H II regions (regions of ionized hydrogen), and therefore these galaxies are often referred to as "H II galaxies". Because the WR phase only lasts for a short time, the presence of a large number of WR stars in a galaxy relative to the number of O-type stars allows us to estimate the age of a starburst *a priori*. No other type of galaxy has such a powerful age diagnostic.

According to the most recent catalog of Schaerer et al. (1999b), there are 139 known WR galaxies to date. Of course, we should perhaps use the term "Wolf-Rayet galaxy" with caution — if a spectrum has sufficiently high signal-to-noise, and if this spectrum happens to be taken at precisely the right location, a single WR star could show up in the integrated spectrum of a galaxy! Nevertheless, WR galaxies (with a few exceptions given this caution) provide us with an opportunity to study the early phases of starburst galaxies.

1.2.3 What Causes a Starburst Episode?

It is reasonable to ask why some galaxies flare into starburst episodes, while most galaxies remain relatively quiescent. The main requirement for a starburst episode is a lot of fuel in a small volume. Heckman (1998) argues that even for a modest starburst, energetics imply the presence of at least 10^8 to 10^{10} $M_\odot$ of cold gas is required to fuel a starburst event (assuming 100% star formation efficiency). Furthermore, this gas must be assembled on very short time scales because of the short times scales for gas depletion in the starburst event and disruption by stellar outflows and supernovae. Thus, one is prompted to ask: what mechanisms could be responsible for collecting large amounts of gas on very short time scales?

Perhaps one of the best ways to concentrate the interstellar medium in a galaxy is to remove its angular momentum, which consequently causes an infall toward the gravitational center. Interactions and mergers of galaxies are particularly adept at accomplishing this inflow; in their numerical simulations, Mihos & Hernquist (1996) find that the rapidly varying gravitational torques in a merging pair of galaxies drives a strong inflow of gas toward the gravitational center. Observations are consistent with this picture; for example, observations of the molecular gas in merging systems often show large amounts of molecular gas in the central regions (e.g., Sargent & Scoville 1991). According to the Mihos & Hernquist (1996) models, the longer the timescale for interaction between two galaxies, the more of an effect dynamical friction can have, the more likely the two galaxies are to merge into a single galaxy, and that this process should be accompanied by a spectacular rate of star formation.

1.3 Super Star Clusters

In relatively nearby starburst galaxies, the most vigorous star formation activity has largely been resolved into massive star clusters. While old globular clusters are ubiquitous in the local universe, only over the past decade have we begun to find their younger and bluer siblings in significant numbers. However, the term “super star cluster” began to appear in the literature well before the 1990s. In 1985, “super star cluster” appeared in reference to a cluster in NGC 1569 (Arp & Sandage 1985). Earlier still, the existence of super star clusters (SSCs) was postulated by Schweizer (1982) in order to explain several knots of star formation in NGC 7252. Perhaps the first reference to super star clusters was as early as the 1970s by van den Bergh (1971) where he called bright infrared knots in M82 super star clusters. These authors were prompted to use the term “super star cluster” because the star clusters observed were far more luminous and massive than young star clusters found in our own galaxy.

Nevertheless, it was not until the launch of the Hubble Space Telescope in 1990 that SSCs came into their own as a research field. (Advocates of HST will proudly tell you that observations of the star cluster 30 Doradus, the Rosetta Stone for SSC research, were among the first successful images taken with HST.) The first observations of SSCs made with HST were done by Holtzman et al. (1992) who discovered a population of massive blue compact clusters in NGC 1275 which they claimed may evolve into globular clusters. After this discovery, the field of massive extragalactic cluster research blossomed.

The precise definition of “super star cluster” is a bit ambiguous, although there seems to be a consensus that minimum mass and density thresholds are the primary means of distinguishing SSCs from other objects like open clusters which are loosely bound or unbound aggregates of a few hunderd stars (although this distinction is artificial and there is a continuum of cluster types). Typically SSCs are defined as “an object which is likely to evolve into a globular cluster in several billion years”, which usually translates into SSCs having estimated masses of $\gtrsim 10^5$ $M_\odot$ within radii of $\lesssim 5$ pc and ages $\lesssim 100$ Myr. There are certainly examples of objects called “SSCs” in the literature which fall outside of this region in parameter space, and it is not uncommon to see star clusters with masses $\sim 10^3$ $M_\odot$ included in samples of SSCs. One might also argue that only clusters with ages less than ≈ 10 Myr should be considered “super star clusters”, as this is the age by which all of the massive stars have died.

1.3.1 Where are Super Star Clusters Found?

Since their discovery, SSCs have been observed in over 50 galaxies including the work presented here (see the review of Whitmore 2000), and this number is still growing. I am often asked if there are any SSCs in the Milky Way, and I believe the answer is no, although the Arches and Quintuplet clusters near the galactic center might provide the most local analogs with masses of $\sim 10^4$ $M_\odot$ (Figer et al. 1999). However, in such a hostile environment, these clusters are not likely to survive to the ripe old age of a globular cluster (e.g., Takahashi & Portegies Zwart 2000). The next most nearby "analog" to an SSC is the 30 Doradus (30 Dor) cluster in the Large Magellanic Cloud which has been extensively studied because, unlike more distant clusters, its stellar content can largely be resolved. The 30 Dor cluster has become such a popular comparison for larger clusters that "30 Dor" often appears as a dimensional unit when describing other systems!

However, to find a genuine SSC, one must look farther away. SSCs are predominantly found in starbursting and merging galaxy systems, although some SSCs candidates have also been found in barred galaxies, tidal tails, and a handful of candidates in relatively normal spiral galaxies. The most well known SSC system is that found in the "Antennae" galaxies (NGC 4038/4039) (Whitmore & Schweizer 1995), a prototypical early stage merger at a distance of ~ 30 Mpc. Several hundred SSC candidates were identified in this system, which spawned a host of follow-up observations in virtually every wavelength regime with every possible instrument. To date, SSCs have been identified at least as far away as ~ 80 Mpc (NGC 3921, Schweizer et al. 1996), but Burgarella & Chapelon (1998) estimate that NGST will allow us to observe SSCs out to a redshift of $z \approx 9$, which will provide an unprecedented opportunity for directly observing globular cluster formation.

1.3.2 The Initial Mass Function and Cluster Mass Estimates

In order to really address the question of whether SSCs are "proto globular clusters", it is critical to determine their masses and densities. To this end, it is also important to determine the slope of the stellar initial mass function. The initial mass function (IMF) can be thought of as the probability of a star with a given mass being formed in a star forming region. The standard IMF commonly used in the literature is the Salpeter value of $\Gamma = 1.35$ (where $n(m) \propto m^{\Gamma}$). Knowledge of the IMF in the extreme star forming regions of super star clusters is critical to understanding their evolution — if there are not enough low mass stars, a cluster will evaporate on timescales short compared to the age of the universe because mass loss via stellar evolution will leave a cluster gravitationally unbound (e.g., Takahashi & Portegies Zwart 2000).

An accurate understanding of the stellar IMF is one of the most important and least understood parameters that affects our understanding of star formation throughout the universe. Some of the questions we wish to answer include: Is the IMF universal? If not, on what parameters does it depend? Is there a limit on the maximum stellar mass which can form? Is there a low-mass cut-off when high mass stars are present? These questions are currently a subject of much discussion in the literature, and a great deal of this discussion has focused on the IMF in clusters of stars — if the IMF does vary, it seems likely that this variation would be the most obvious in extreme star birth events, such as the formation of SSCs.

The primary difficulty in accurately determining the stellar IMF in clusters is that spectroscopy must be obtained for each of the high mass stars in the cluster in order to classify it and thus determine its mass. This necessity immediately limits us to only the clusters in the Milky Way, Magellanic Clouds, and under excellent observing conditions perhaps some of the closest Local Group galaxies. For the highest mass and most luminous stars in a cluster, accurate spectroscopy is relatively trivial. Lower mass stars can in principle be classified with photometry alone. However, because of the crowding and their inherently lower luminosities, obtaining accurate observations for low mass stars in a cluster is exceptionally difficult.

Thus, several authors have turned to the nearest super star cluster analogs in order to address the IMF issue. Figer et al. (1999) attempted to determine the IMF for the Arches and Quintuplet clusters near the Galactic center. They find that these clusters have IMFs flatter (i.e. relatively more massive stars) than the Salpeter IMF above $\sim 10\ M_{\odot}$. Strictly interpreted, Figer et al. (1999) note that this IMF might reflect the affect of strong tidal sheer inhibiting low-mass star formation. However, Kim et al. (1999) point out that mass segregation due to stellar relaxation is likely to take place in these clusters on very short times scales, and consequently we are now seeing the *present day* mass function and not the *initial* mass function. Using the superb spatial resolution of HST, Massey & Hunter (1998) measured the IMF in 30 Dor down to $2.8\ M_{\odot}$ and found that it is consistent with a standard Salpeter IMF. However, Sirianni et al.

(2000) obtained HST data ~ 1 magnitude deeper than the Massey & Hunter observations, and claim that the IMF is normal above ~ 2 M$_\odot$, but flattens at lower masses.

The stellar IMF has a direct relation to the masses of SSCs. In §1.3.1 I quoted a rough lower mass limit of $\approx 10^5$ M$_\odot$ for a cluster to be considered an SSC. However, typical mass estimates for super star clusters are dependent on the adopted IMF. By far the most common technique for determining the mass of a super star cluster (which I will employ later in this thesis) is to estimate its mass based on the observed luminosity and estimated age in combination with models, such as those of Leitherer et al. (1999). However, while this method is the simplest and can be applied even to systems the farthest away, it has the obvious pitfalls of being dependent on the model assumptions (perhaps most importantly the IMF) and the (typically unknown) extinction value.

Alternatively, it is possibly to measure the mass relatively directly if a cluster is sufficiently isolated and has a high enough apparent brightness. In this case, one can measure the mass relatively directly with spectroscopy and infer an IMF based on the mass to luminosity ratio. With this method, line widths are used to determine the stellar velocity dispersion (typically using intrinsically narrow absorption lines from the atmospheres of cool supergiants), which in turn are used to estimate the mass (assuming virial equilibrium).

This technique has only been applied to a handful of clusters meeting the above criteria — such measurements have been made for clusters in NGC 1569 (Ho & Filippenko 1996a), NGC 1705 (Ho & Filippenko 1996b), and M82 (Smith & Gallagher 2001). The clusters that have been directly probed with this method have masses in the range of a few $\times 10^5$ to a few $\times 10^6$ M$_\odot$. Smith & Gallagher (2001) find that, while the IMF for the cluster in NGC 1705 has a steeper than Salpeter IMF, the clusters in both NGC 1705 and M82 appear to either be flatter or truncated at a mass of $1 - 3$ M$_\odot$.

The uncertainties in the IMF determinations are still large, and while there are suggestions of variations in the IMF (as above), there is no conclusive evidence for variations at the present time. Nevertheless, in many areas of astrophysics, an IMF must be assumed as it cannot

Table 1.1: Sample of Cluster Luminosity Functions

Galaxy	Distance[a]	N[b]	α[c]	Reference
He 2-10	9 Mpc	76	-1.7	Johnson et al. (2000)
NGC 4038/4039	22 Mpc	800	-2.1	Whitmore & Schweizer (1995)
NGC 3256	37 Mpc	> 1000	-1.8	Zepf et al. (1999)
NGC 1741	51 Mpc	314	-1.9	Johnson et al. (1999)
ESO 565-11	63 Mpc	700	-2.2	Buta et al. (1999)
NGC 7252	63 Mpc	499	-1.8	Miller et al. (1997)
NGC 3921	78 Mpc	102	-2.1	Schweizer et al. (1996)

[a] Distance assuming $H_0 = 75$ km s^{-1} Mpc^{-1}.
[b] Number of super star clusters detected.
[c] Slope of power-law luminosity function for detected clusters.

directly be measured (such is the case in the work presented here), and a standard Salpeter IMF remains arguably the most logical choice.

1.3.3 The Luminosity Function of Super Star Clusters

The luminosity functions for entire systems of SSCs typically have a power law form of $\phi(L) \propto L^{\alpha}$, where the measured values of α are very closely clustered around $\alpha \approx -2$ (see Table 1.1). It is interesting to note that this power-law slope is similar to that observed for Galactic H II regions (McKee & Williams 1997) and molecular clouds (Harris & Pudritz 1994). However, this power-law behavior is not consistent with the luminosity function for galactic globular clusters, which exhibit roughly a lognormal distribution with a peak at $\approx M_V = -7.5$ (Harris 1991) [4] . Opponents of the theory that SSCs are proto-globular clusters have used this as evidence for the two types of objects coming from inherently different processes (e.g., van den Bergh 1995).

However, SSCs are likely to have a significant “infant mortality rate”, preferentially affecting the least massive and least dense clusters. Several destruction mechanisms have been proposed, including 2-body relaxation, tidal shocking, and stellar mass loss. Using simple ana-

---

[4] Some studies have found weak evidence that, over the high luminosity range, a power-law distribution fits the globular cluster luminosity function marginally better than a lognormal distribution (e.g., Secker 1992).

lytical models to account for cluster disruption, Zhang et al. (2000) find that over a wide variety of initial conditions, power law mass functions will evolve into the lognormal distribution similar to that observed for Galactic globular clusters.

Finally, some of the SSC systems show evidence for having a flatter power law at fainter magnitudes (e.g., Whitmore et al. 1999). The break in the power law corresponds to roughly a mass of $\sim 10^5$ $M_\odot$, which Whitmore (2000) has pointed out is similar to the typical globular cluster mass. This loosely suggests that the lower mass SSCs may have already undergone some amount of destruction, and we are beginning to see a hint of the peak in the globular cluster distribution.

If the present-day luminosity function of globular clusters does, in fact, reflect the dissociation of lower mass clusters over approximately a Hubble time, then as we observe globular cluster systems in the earlier universe we should see evidence of this evolution. In particular, the peak of the globular cluster luminosity function should shift to fainter luminosities as we look farther away. To date, we lack the instrumentation with high enough spatial resolution and sensitivity to carry out this experiment.

1.3.4 Formation of Super Star Clusters

It appears that the majority of star formation takes place in clusters or associations of some kind. In surveys of molecular clouds, typically 50% to 90% of the stellar populations appear to be formed in a clustered environment (Clarke et al. 2000, and references therein). Remarkably, massive star clusters, open clusters and associations, and molecular clouds all appear to have initial power-law mass distributions with a slope of ~ -2. Elmegreen & Efremov (1997) have put forth a “universal formation mechanism” for star clusters, arguing that scale-invariant structure in turbulent interstellar gas would naturally result in this observed power law distribution. However, most of these birth clusters will dissociate over relatively short times scales.

While forming stars in clusters (of some kind) appears to be a common mode of star formation, forming bound massive clusters must require physical conditions which are not typical in normal galaxies given the dearth of massive clusters which appear to be forming in such environments. Two main ingredients appear to be required in order to form bound massive clusters — high star formation efficiency and high pressure. The need for high star formation efficiency is due to the violently disruptive effect massive stars have on the interstellar medium; if a significant fraction of a cluster's initial mass remains in the form of gaseous material when the massive stars are formed, this material will be expelled from the cluster by stellar winds and supernovae, and the cluster will become unbound. Star formation efficiencies greater than ~ 0.2 to 0.5 appear to be required in order to avoid this fate (e.g., Hills 1980).

If mass loss occurs quickly compared to the dynamical time of the cluster, $\tau_D \sim (\mathrm{G}\rho)^{1/2}$ (where ρ is the mass density), then the cluster's stars do not have time to virialize and are left with a higher velocity dispersion than the potential well can compensate for, consequently causing the stars to escape the cluster. An obvious mechanism for reducing this effect is for the cluster to remove the gaseous material only over long timescales in order for the cluster to have time to react adiabatically. Alternatively, angular momentum could act to stabilize the cluster mass loss, but it would also inhibit star formation [5] . Magnetic fields could also protect the cluster from undergoing catastrophic mass loss by essentially storing kinetic energy as the cluster material collapses out of the ISM, compressing the magnetic field. In the final virialized state, the kinetic energy of the cluster would be lower, thus resulting in a lower stellar velocity dispersion at the time of mass loss.

Finally, a high pressure environment can help a cluster to remain bound for several reasons. First, if the virial velocity dispersion of a cluster is large compared to the velocity at which massive stars can drive an outflow (~ 10 km s^{-1}), the gaseous material is more resistant to dispersal (Elmegreen et al. 2000a). Assuming a virialized velocity distribution of roughly,

$$\langle v^2 \rangle \sim \frac{\mathrm{G\ M}}{\mathrm{R_{eff}}}, \tag{1.1}$$

---

[5] For example, the Toomre criterion (Toomre 1964) predicts that the critical surface density for star formation in a collisionless disk is proportional to the epicyclic frequency.

for a hypothetical cluster with a mass of $\mathrm{M} = 10^6\ \mathrm{M}_\odot$ and effective radius of $\mathrm{R}_{\mathrm{eff}} = 3$ pc, the resulting virial velocity is ~ 30 km s^{-1}. If the pressure is roughly $\mathrm{P} \approx \rho v^2$, these parameters imply a necessary pressure of $\mathrm{P} \approx 10^{10} k_B$ cm^{-3} K. Along this same line of reason, higher pressures will result in virialized clusters with higher binding energies.

Another benefit of forming a cluster in a high pressure environment is that the star formation process can happen on a shorter timescale. Very heuristically, one can think of this increased rate of star formation as simply being due to the higher density of material which has been compressed, or also due to the increased sound speed allowing for the star formation to take place more quickly over larger scales. The more quickly star formation takes place, the better chance the interstellar medium can be transformed into stars before the young massive stars begin to have a significant impact on the remaining gaseous material, thus potentially increasing the star formation efficiency. A related effect is that, if the surrounding region has a high pressure, it may help to contain the gaseous material after the onset of massive star formation.

In relation to the “universal formation mechanism” proposed by Elmegreen & Efremov (1997), it seems the main difference between the formation of bound massive clusters and other types of clusters is a high pressure environment. To test this prediction, let us return to 30 Dor as a local analog. Chu & Kennicutt (1994) measure a density and velocity of the central cluster in 30 Dor which imply a pressure of $\mathrm{P}/k_B \sim 10^7$ cm^{-3} K, which is 3 to 4 orders of magnitude higher than typical pressures in molecular clouds in the Galaxy of $\mathrm{P}/k_B \sim 10^3$ to 10^4 cm^{-3} K (Jenkins et al. 1983). Elmegreen & Efremov (1997) note that similarly high pressures would result if interstellar media with a densities of ~ 10 atoms cm^{-3} collided at a typical galactic orbital speed of ~ 200 km s^{-1}. It seems clear that the formation of bound massive clusters requires pressures much higher than those typically found in molecular clouds in the Galaxy, but which may be commonplace in merging and interacting galaxies.

1.4 The Birth Environment of Massive Star Clusters

After the criteria for massive star cluster formation have been achieved and star formation has commenced, the newly born stars will remain swaddled in the material from which they were formed for some time. The timescale over which a massive star will pass through the early stages of development is not well characterized, however the early stages of massive star evolution must take place on faster time scales than low mass stars. As a lower limit, Kurtz et al. (2000) have suggested the free-fall time of $\gtrsim 10^4$ years for an individual massive star.

In the very earliest stages of massive star evolution, the massive proto-star is an extremely dense clump of warm material known as a "hot core". Hot cores are physically defined by densities $\gtrsim 10^7$ cm^{-3}, and temperatures $\gtrsim 100$ K (Kurtz et al. 2000). These objects are typically detected with high density molecular tracers, such as CS, which have critical densities (below which they are not observable) $\gtrsim 10^5$ cm^{-3}, and many examples of hot cores have been found in the Galaxy.

As the proto-star evolves toward its main sequence lifetime, it will also begin to ionize the surrounding interstellar medium. The resulting H II regions are very dense and compact and have come to be known as "ultra compact H II regions" (UCH IIs). This UCH II phase is also not observable in optical or UV wavelengths, but rather they are generally detected by their mid- to far-infrared or radio spectral energy signatures. UCH IIs are commonly associated with other phenomena such as maser emission or molecular outflows, both of which are additional signs of star formation activity.

It is likely that massive star clusters follow a similar evolutionary sequence to that of the individual massive stars of which they are made. However, this area of research has only recently opened up with radio and mid-infrared instrumentation gaining the sensitivity and spatial resolution necessary to study these objects in an extragalactic context. Indeed, Chapters 4 and 5 of this thesis will focus on these recent developments.

1.5 Thesis Outline

The goal of this thesis is to examine the nature of super star clusters throughout their evolutionary development in starburst galaxies. The globular clusters abundant in the local universe are analogous to fossils on earth and provide a valuable historical record of star formation in the universe. However, unlike archaeologists, we have the ability to make expeditions to pockets of the universe which are earlier in their evolutionary sequence than our own surroundings. In this sense, the chapters of this thesis travel backward in time — beginning with super star clusters which are well into their adolescence and continuing to follow the chronology to a sample of super star clusters which are still embedded in their birth material.

In Chapter 2, I examine several starburst galaxies in the Hickson Compact Group 31 with both Hubble Space Telescope and ground-based data. A large number of super star clusters are identified, and the photometry of these objects indicates that they have a median age of ~ 4 Myr. The luminosity function of these clusters is consistent with that found in numerous other starburst galaxies. The star formation rate and burst environment are also discussed. Perhaps the most striking result of this chapter is the discovery of a dwarf galaxy in the group which shows no sign of previous star formation and may have only recently collapsed out of the intergalactic medium.

A similar case study of the starburst galaxy Henize 2-10 is presented in Chapter 3 using data from the Hubble Space Telescope. The numerous super star clusters identified in this system also appear to have typical ages $\lesssim 10$ Myr. The luminosity function for this system is in accord with the canonical value found elsewhere (and in Chapter 1). A unique result from this Chapter is the detection of a high velocity outflow (~ 360 km s^{-1}) which could potentially have a dramatic impact on the surrounding intergalactic medium.

Chapter 4 provides an overview of the discovery of "ultra dense H II regions" (UDH IIs) with radio and mid-infrared observations. These UDH IIs represent the earliest stage of massive star cluster evolution observed to date. From the radio observations, the electron densities, radii, and number of ionizing photons (and therefore number of embedded massive stars) are estimated. The mid-infrared observations confirm the presence of hot dust cocoons surrounding these objects. These embedded clusters account for at least $\sim 60\%$ of the mid- to far-infrared flux of the entire galaxy. Finally, the impact of UDH II s on the well known radio to far-infrared flux ratio is discussed.

Inspired by the discovery of UDH II s, I searched the literature for possible serendipitous detections which were not classified as such. Chapter 5 presents the result of this search, which resulting in the detection of 35 UDH II candidates in the galaxies M33, NGC 253, and NGC 6946. This sample of objects begins to fill in the continuum between individual UCH II s and the embedded massive clusters. The properties of this sample are analyzed, such as the electron densities, radii, and number of ionizing photons. Finally, the connection to UCH II complexes in the Galaxy (such as W49) is discussed, and luminosity functions are presented.

Chapter 6 overviews the directions in which I hope my future research will take the field of massive star cluster formation and evolution. Given the very recent discovery of UDH II s, a large number of questions remain to be addressed. I discuss the possibilities for expanding the sample of UDH II s, determining the physical properties of their birth environments, developing an evolutionary scenario, and the need for more sophisticated modeling efforts.

Chapter 2

The Case of Hickson Compact Group 31

2.1 Background

Compact groups of galaxies provide a rich environment in which to study galaxy interactions and merger events. Compact groups of galaxies are among the densest concentrations of galaxies known, comparable to the centers of rich galaxy clusters. However, unlike galaxy clusters, compact groups have relatively low velocity dispersions ($\sigma \approx 200 - 300$ km s^{-1}), increasing the likelihood of gravitational interactions between group members. Hickson compact groups were selected by a systematic search of the Palomar Sky Survey prints (Hickson 1982). The criteria required that the groups have ≥ 4 galaxies within three magnitudes of the brightest member, the groups must be compact based on the surface brightness within θ_G (where θ_G is the angular diameter of the smallest circle containing the galaxies), and the groups must be must be isolated such that no other galaxies within the given magnitude range (or brighter) were within $3\theta_G$.

The nature of compact groups has been a subject of considerable discussion ever since it was realized that such systems should be dynamically unstable. Hickson et al. (1977) investigated the relationship in compact groups between the velocity dispersions, densities, and size of galaxies. They found that the time scales in which the groups should be destroyed via dynamical friction are “disturbingly short”; given the small sizes of these groups and low velocity dispersions, dynamical friction should cause these systems to be destroyed via galaxy mergers in times short compared to the age of the universe. Therefore, it is unlikely that the observed number of compact groups could exist without continuously evolving from another class of objects, such as loose groups.

Supporting the idea that the morphology of compact groups, and their subsequent evolution, is altered by dynamical effects, Hickson et al. (1992) found a significant correlation between the crossing time and the fraction of gas-rich galaxies in a group — groups that are likely to have undergone more interactions and mergers in their history have a smaller fraction of spiral and irregular galaxies. Further support for the frequency of galaxy interactions in the compact group environment comes from the large amount of tidal debris found within such groups by Hunsberger et al. (1996). The luminosity, mass, morphology, and dynamics of many compact groups support current theories for the formation of a single large elliptical galaxy from the merger process (Rubin et al. 1990; Barnes 1989). Since compact groups must be continually undergoing such transformations, these dynamical processes may have played an important role in creating the distribution of galaxy morphologies observed today. Because of their relative proximity, compact groups provide us with a unique environment to study the possible conditions in which a substantial amount of galaxy formation took place at high redshift.

On the low end of the galaxy mass spectrum, some dwarf galaxies may also form during compact group evolution in the tidal debris of the interacting galaxies. These objects are known as Tidal Dwarf Galaxies (TDGs) and have been observed in a number of systems (Mirabel et al. 1991, 1992; Duc & Mirabel 1994; Elmegreen et al. 1995; Hunsberger et al. 1996, 1998). There are two main models that attempt to explain the formation of TDGs: In stellar dynamical models, stars are tidally removed from the parent galaxies, form concentrations, and ambient gas may then fall into the potential well (Barnes & Hernquist 1992). Alternatively in hydro dynamical models, concentrations of gas have a larger gravitational impact than stars, local instabilities in the tidal tails form giant molecular clouds, and star formation may be triggered by the subsequent collapse (Elmegreen et al. 1993). To date, there is no conclusive evidence favoring either of these scenarios as the dominant mechanism.

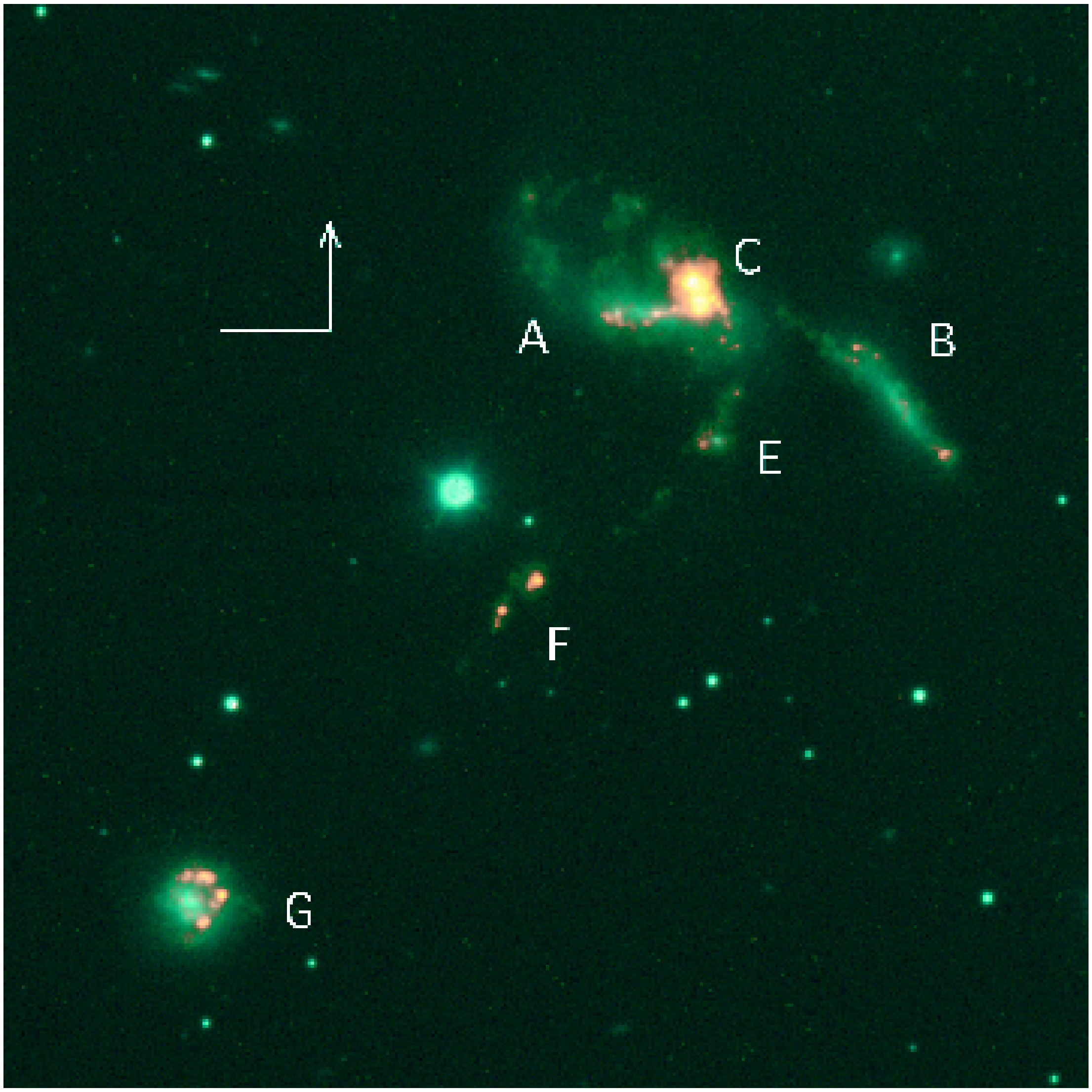

Figure 2.1: Color image of HCG 31 constructed using the narrow-band Hα and continuum images from the WIYN telescope. A blue-green color is indicative of continuum emission, while a red-orange color is representative of Hα emission. North and east are indicated on the image, with north having the arrowhead.

The Hickson Compact Group 31 (HCG 31), at a distance of 51 Mpc ($H_0 = 75$ km s^{-1}Mpc^{-1} Vacca & Conti 1992, hereafter VC) is one of the most well-studied compact groups because of the peculiar morphology of its members and the prominent starbursts its brightest galaxies (see Figure 2.1). Members with similar redshifts include galaxies A, C, B, E, F, and G (Mrk 1090); galaxy D is a background object (Rubin et al. 1990). Galaxies A and C are an interacting pair of galaxies known as NGC 1741 (= Mrk 1089 = Arp 259), and for the remainder of this work I refer to them together as galaxy “AC”. The entire group is within a common envelope of gas with a total hydrogen mass of $2.1 \times 10^{10} M_{\odot}$ (Williams et al. 1991). The peak H I emission is at the location of galaxy AC with a column density of 2.9×10^{21} atom cm^{-2}; slightly weaker emission peaks of 1.9×10^{21} atom cm^{-2} are coincident with galaxies F and G. Galaxies E and F could be considered to be TDGs. Very nice ground based photometry, at a lower spatial resolution than will be presented in this chapter, has been published by Iglesias-Paramo & Vilchez (1997). NGC 1741 (galaxies A and C) is one of the most luminous W-R galaxies ($M_B = -20.3$) in Conti’s catalog of Wolf-Rayet galaxies (Conti 1991).

Previous ground-based Hα imaging of NGC 1741 indicates two dominant starburst regions aligned NNE–SSW in galaxy C, the southern one located at the intersection with galaxy A; another starburst region is found at the eastern end of galaxy A (Iglesias-Paramo & Vilchez 1997). Galaxies B, E, F and G *all* also show starburst activity with strong Hα emission. In accordance with its classification as a W-R galaxy (Conti 1991), the optical spectrum of NGC 1741 shows broad emission line features due to W-R stars (Kunth & Schild 1986). VC detected W-R stars in the *southern* but not the *northern* starburst region in galaxy C (VC label the former NGC 1741B). The strong nebular emission line spectra of both regions indicates that substantial numbers of O stars are present; the presence of W-R stars suggests the star formation activity could be very recent, only a few Myr old. The metallicity of the starburst regions analyzed by VC (1992) is $Z \approx 0.25$ Z$_{\odot}$.

A straightforward way to gain insight into the physical conditions in very distant galaxies, as well as in very young globular clusters, is to examine galaxies that are close enough to have resolvable morphologies, yet with conditions similar to those young galaxies at $z \approx 3$. SSCs can be analyzed for parameters such as age, duration of burst, initial mass function, star formation rate, and extinction using spectroscopy and photometry combined with population synthesis models such as those of Leitherer et al. (1999). In this chapter I present an analysis of recent high-resolution HST optical images of HCG 31 as well as ground-based Hα images obtained with the WIYN telescope on Kitt Peak.

2.2 Observations and Data Reduction

2.2.1 WFPC2 Data

Optical images of HCG 31 were obtained on 1995 July 10 using the WFPC2 camera aboard the Hubble Space Telescope. Images were acquired through four broad-band optical filters: F439W, F555W, F675W, and F814W. In each filter, two dithered sets exposures were taken as follows: F439W (2×400 s, 30 s; 600 s, 350 s, 30 s), F555W (2×300 s, 30 s; 2×300 s, 30 s), F675W (2×400 s, 30 s; 2×300 s, 30 s), F814W (2×400 s, 30 s; 2×400 s, 30 s). Dithering is necessary to regain some of the spatial information lost due to the under-sampling of the HST PSF by WFPC2. The shorter (30 s) exposures were taken in case of saturation on the images with longer exposures; however, none of the images reached saturation levels, and the 30 s exposures were not analyzed.

Galaxies A and C (NGC 1741) were located on the planetary camera (PC), while galaxies E and F were imaged on the wide field camera #4 (WF4). Galaxies B and G were unfortunately not located in the field of view. The PC and WF4 images were reduced following the standard pipeline procedures (including the application of bias, dark, and flatfield frames) using the Image Reduction and Analysis Facility (IRAF) and the Space Telescope Science Data Analysis System (STSDAS). The STSDAS task GCOMBINE was used to combine pairs of long exposures and remove hot pixels and cosmic rays. Additional cosmic rays and hot pixels were identified by visual examination and removed. A correction for geometric distortion was applied as prescribed by Holtzman et al. (1995a). The dithered images were then combined using the "shift and add" technique: the images were block-replicated, shifted by an integer number of pixels (dithered offsets were determined from the STSDAS task CROSSCOR), and then the dithered pairs were combined. This process resulted in final images with sizes of 1600 pix × 1600 pix and a scale of 1 pixel = $0.02277''$ on the PC and 1 pixel = $0.0498''$ on WF4. I have not analyzed the WF2 and WF3 regions of the images.

WFPC2 is known to have a charge transfer efficiency problem (Holtzman et al. 1995b) which causes objects at the top of the chip to appear fainter than when they are observed at the bottom. The effect is at the 4% level over a blank field, however, this effect appears to be significantly reduced (0 - 1.5%) in the presence of a moderate background. Given the variable nature of the background in NGC 1741, with many of the objects in regions with backgrounds greater than 10 counts per pixel, application of the standard linear ramp correction would introduce unnecessary errors in my photometry, and I have not applied any correction to these data. The photometric zeropoints were determined from the PHOTFLAM keyword in the image header, with resulting magnitudes in the STMAG system. These magnitudes were then shifted to a Vega zeropoint. In order to facilitate comparisons with previous work published in the Johnson-Cousins system, the F555W and F814W magnitudes were converted to V and I passband magnitudes in the Johnson-Cousins system, following the prescription given by Holtzman et al. (1995a). However, this conversion increases the amount of error in the magnitudes; therefore, unless otherwise noted, I have adopted the HST system magnitudes with a Vega zeropoint, which I refer to as B_{ST}, V_{ST}, R_{ST}, and I_{ST}.

A number of point sources were identified in each of the images of HCG 31 using the IRAF task DAOFIND, whose parameters were adjusted to detect sources $\geq 5\sigma$ above the local background level; lowering this detection threshold resulted in an unacceptable number of spurious detections. The four filter images were then visually inspected to check the resulting source identifications, and sources were added to or deleted from the list by hand. However, it is possible that some of these sources could be individual supergiants that are luminous enough to be detected at the distance of HCG31. Based upon an analysis of the photometry of the most luminous stars by Sohn & Davidge (1996) and following Whitmore et al. (1999), I adopt $M_V = -8.5$ as an effective *upper* limit to single star absolute magnitudes (fainter than this value stars begin to appear in significant numbers). Thus all sources brighter than this magnitude are assumed to be SSCs in what follows, although there are almost certainly SSCs that are fainter than this cutoff.

For galaxies E and F on the WF4 camera, this process resulted in a total of 39 detections present in each filter image with 19 objects associated with galaxy E, 16 with galaxy F, and 4 objects among the remaining tidal debris (although it should be noted that there is a great deal of amorphous material between galaxies E and F which was not “detected”). For the larger starburst system, NGC 1741, this process resulted in 144 source detections in the B_{ST} image, 314 in the V_{ST} image, 329 in the R_{ST} image, and 300 in the I_{ST} image. The identifications from the four passbands were then cross-identified, with the final list consisting of 434 individual sources, which I label as super star clusters, detected in one or more of the four filters.

Completeness limits for each filter image were determined by adding artificial stars of known input magnitudes to each image and attempting to recover these stars with the same detection procedures and thresholds used for identifying real objects in the original images. The stars were created with the PSF generated from the images, with input magnitudes randomly distributed in a 2-3 mag range around an estimated completeness limit. Fifteen thousand of these artificial stars were added, one at a time, at randomly selected positions, to each image and recovery of each star was attempted using DAOFIND. The fraction of stars with input magnitudes between m and $m + 0.1$ mag that were recovered as a function of m was determined with this procedure. The results are presented in Table 2.1. The completeness limit I have adopted is defined to be the magnitude at which the recovered fraction is > 0.90. Obtaining completeness limits $> 90\%$ is limited by confusion in the crowded starburst regions, and the completeness was typically $< 95\%$ even for the brightest objects.

Table 2.1: Completeness limits found in each of the four filters for NGC 1741 as described in the text.

Completeness Level	Image B_{ST}	V_{ST}	R_{ST}	I_{ST}
$\geq$ 0.50	23.7	24.5	24.3	23.9
$\geq$ 0.75	23.6	24.4	24.1	23.8
$\geq$ 0.90	23.5	24.3	24.0	23.6
$\geq$ 0.95	23.3	24.1	23.9	23.0

Using the Schlegel et al. (1998) maps of infrared dust emission, I infer a Galactic extinction of E(B-V) = 0.05 at the position of HCG 31. In what follows, I have adopted this foreground extinction and a distance modulus of 33.54. Local reddening is likely variable across the individual galaxies and the compact group, and no correction for internal extinction has been applied to these data.

Photometric measurements were made with both PSF-fitting and aperture photometry routines. HCG 31 has both a variable background and severe crowding in the two main starburst regions of NGC 1741. These factors would naturally lead one to use PSF-fitting routines to determine photometric magnitudes; however, there are no Galactic foreground stars present on the PC images from which a PSF could be constructed. Consequently, the PSF for NGC 1741 was determined by assuming that some of the SSCs were, in fact, point sources at this spatial resolution (radii will be discussed in §2.3.4). Both photometric methods were used, as described below, in order to determine the robustness of the resulting magnitudes subject to these complications.

Aperture photometry was carried out using the IRAF task APPHOT with a source aperture of 3 pixels and a background annulus of 8-10 pixels. These aperture sizes were chosen by inserting 50 artificial sources into the images and determining which combination of aperture and annulus most closely reproduced the input magnitudes. Aperture corrections were calculated based on the results of the PSF fitting procedure, which was performed with the IRAF task DAOPHOT. For NGC 1741 the PSFs in each filter were created from seven super star clusters which were found to be relatively isolated and which had FWHMs consistent with artificial PSFs created using the STSDAS program TINY TIM V4.0 (Krist 1993). For the galaxies on WF4, PSFs in each filter were built using several foreground stars in the images.

The functional form of the PSF was found by fitting several standard profiles (with different fitting radii) to the PSF derived from the images. For the PC, a Moffat15 profile was found to have residuals with a mean closest to zero and the smallest standard deviation. For the WF4, a Lorentz profile was found to have the smallest standard deviation and was adopted in order to determine the aperture corrections in each filter. The resulting PSFs have encircled energy curves which are consistent with those published by Holtzman et al. (1995b).

The magnitudes determined from the two photometry methods agree well within the errors for most of the super star clusters brighter than 19th magnitude. Many of the magnitudes found for the fainter SSCs also have a similarly high level of correspondence; however, in some cases the two methods yield results that differ by as much as $\sim$1 magnitude for these faint sources. In these instances the SSCs were found to be located in crowded regions and/or to have a high and variable backgrounds, properties which suggest that the magnitudes derived from the aperture photometry method are not reliable. Consequently, for consistency, I have adopted the magnitudes determined from PSF fitting. The resulting errors as a function of magnitude for each filter are shown in Figure 2.2a for the PC and Figure 2.2b for WF4.

The multi-color image of NGC 1741 (shown in Figure 2.3) was constructed using the IRAF package RGBSUN and the B_{ST}, V_{ST}, and I_{ST} images. The color scales have been enhanced to illustrate the *differences* in color throughout the galaxy; if “true color” were used, the entire galaxy would appear blue-white (Wray 1988). In order to show a greater dynamic range, I have used logarithmic intensity mapping. The range in color for galaxies E and F is not as large, and I have opted to show grayscale V_{ST} images of these galaxies instead; galaxies E and F are shown in Figure 2.4. These images will be discussed in § 3.3.1.

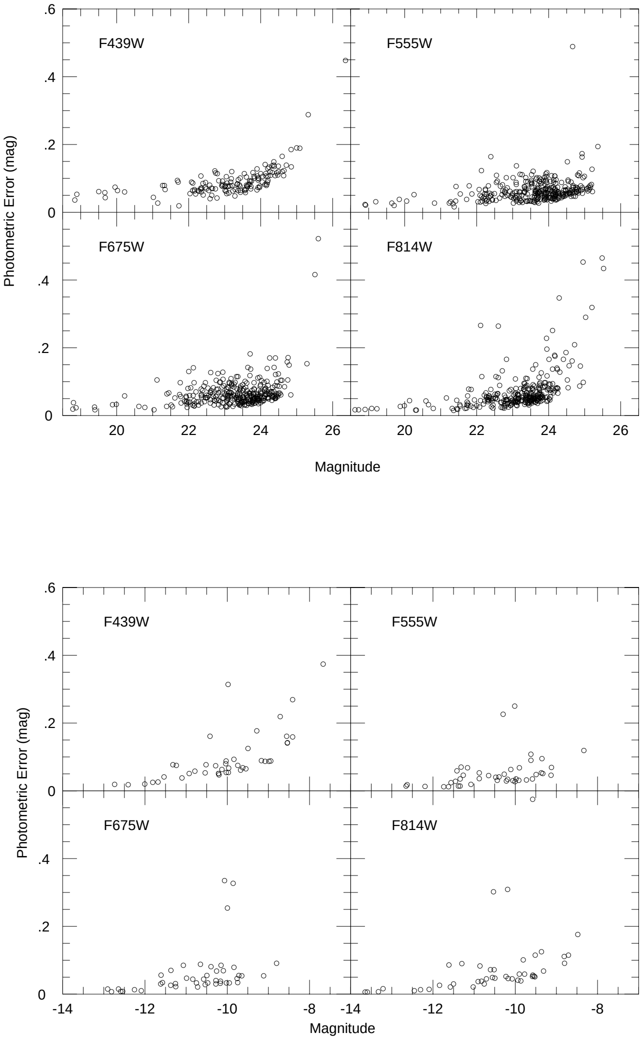

Figure 2.2: Uncertainties as a function of magnitude for the F439W, F555W, F675W, and F814W filters. (top) galaxies A and C; (bottom) galaxies E and F.

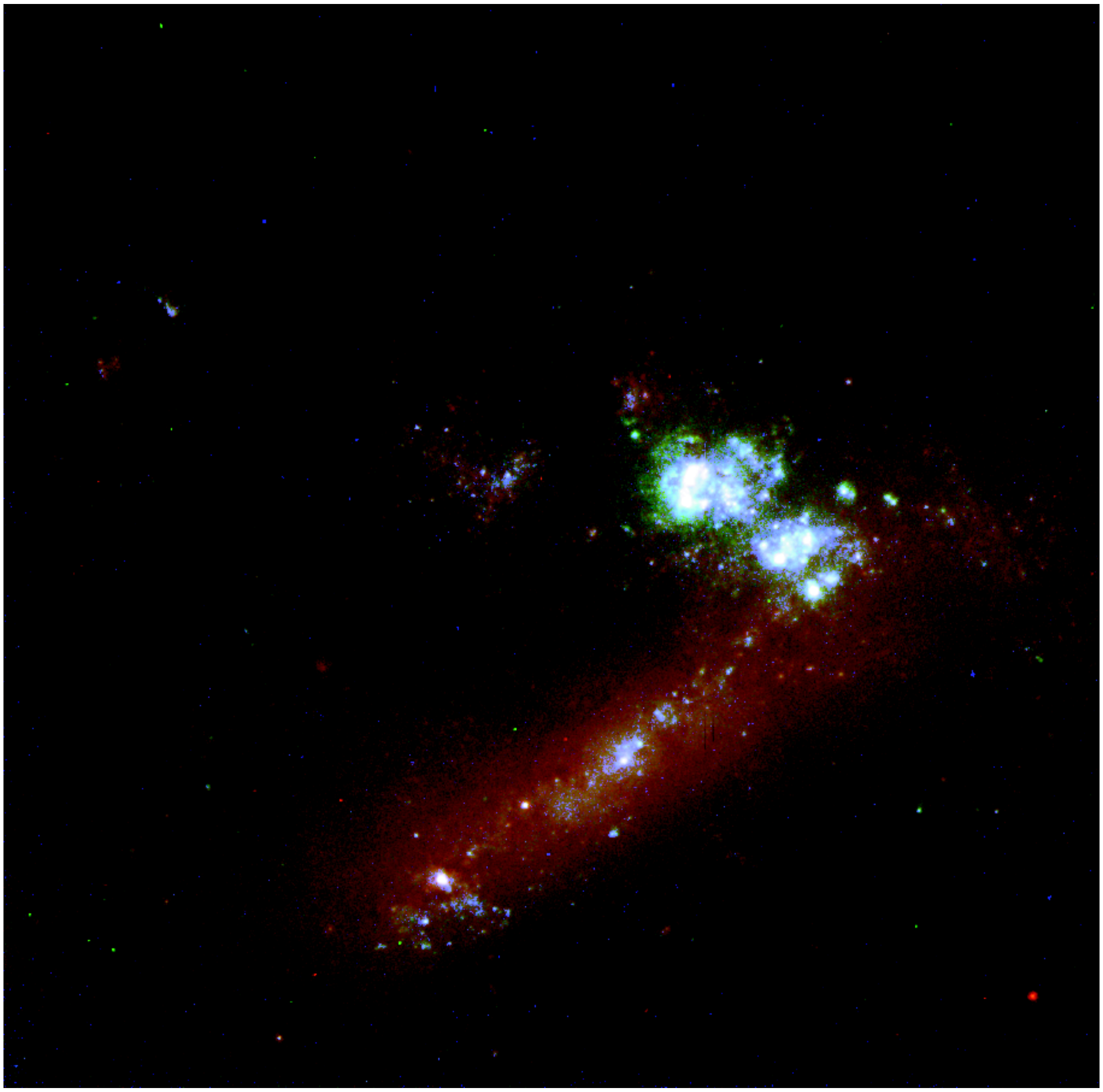

Figure 2.3: Color image of NGC 1741 constructed using the B_{ST}, V_{ST}, and I_{ST} images from HST. The color scales have been enhanced to illustrate the *differences* in color throughout the galaxy, however if true color were used the entire galaxy would appear blue-white.

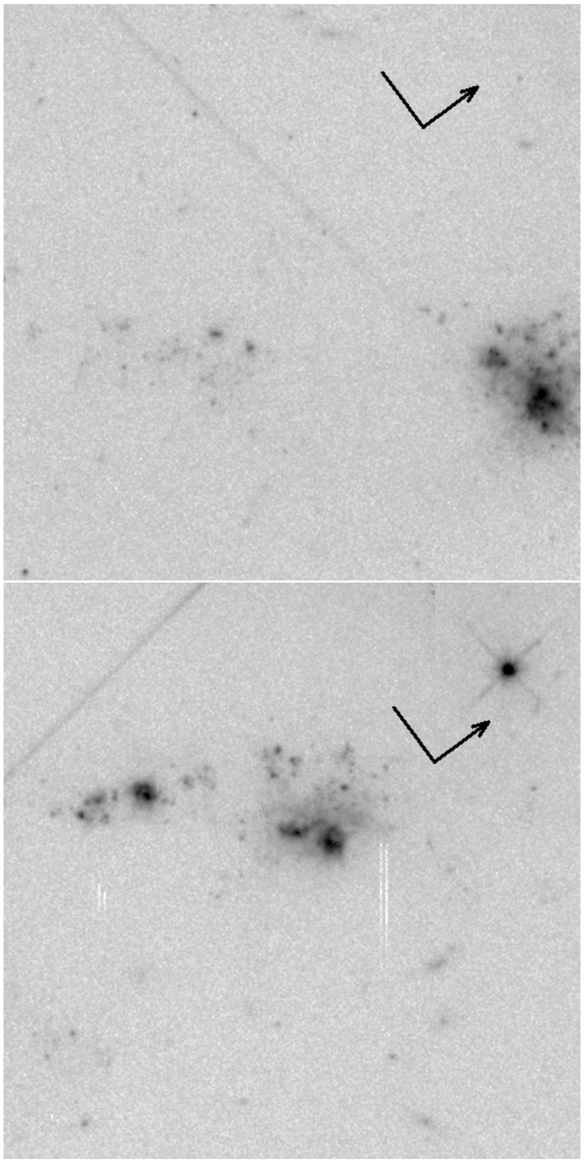

Figure 2.4: V_{ST} images of (top) galaxy E and (bottom) galaxy F from HST. North and east are indicated on the images, with north having the arrowhead. Both images are shown at the same physical scale.

2.2.2 WIYN Data

Narrow band Hα and continuum images of HCG 31 were obtained on 1998 January 19 using the WIYN 3.5 m telescope on Kitt Peak through the queue observing program. I used the S2KB detector, which has a plate scale of $0''.197$ pixel^{-1} and total field of view of $6'.7 \times 6'.7$. The W15 and W16 filters were used, which have central wavelengths of 6570 Å and 6618 Å and FWHMs of 73 Å and 72 Å respectively, and throughputs of around 86%. Two sets of dome flats were taken during the 2 hour queue program, each consisting of 5 exposures in each of the filters. Data reduction followed the standard procedures (including application of the bias and flat-field frames) using the IRAF task CCDPROC. Unfortunately, the weather conditions were not photometric, with scattered cirrus present during the observations, and therefore absolute photometry can not be determined. However, the seeing was excellent, with the FWHM of stellar objects in the field measured to be $0''.7$ to $0''.8$.

In order to obtain equivalent width (W(Hα)) measurements of the star forming regions I followed the method of Iglesias-Paramo & Vilchez (1997) and scaled the continuum and Hα images until the fluxes of the non-saturated field stars were equal in both frames. Using 74 stars, the average flux ratio was found to be Flux(6618 Å)/Flux(6570 Å) = 1.03 with a standard deviation of 0.06. Because the scaling determined by this method was less than the error associated with it, I adopted the initial scaling of the images as adequate, and the uncertainty as a function of W(Hα) is shown in Figure 2.5.

A color image of HCG 31 using the narrowband Hα and continuum filters was created with the IRAF task RGBSUN and is shown in Figure 2.1. A blue-green color in the image should be interpreted as continuum and red-orange should be interpreted as Hα. Therefore, regions in this image which appear red-orange are the areas which have most recently undergone (or are currently undergoing) star formation.

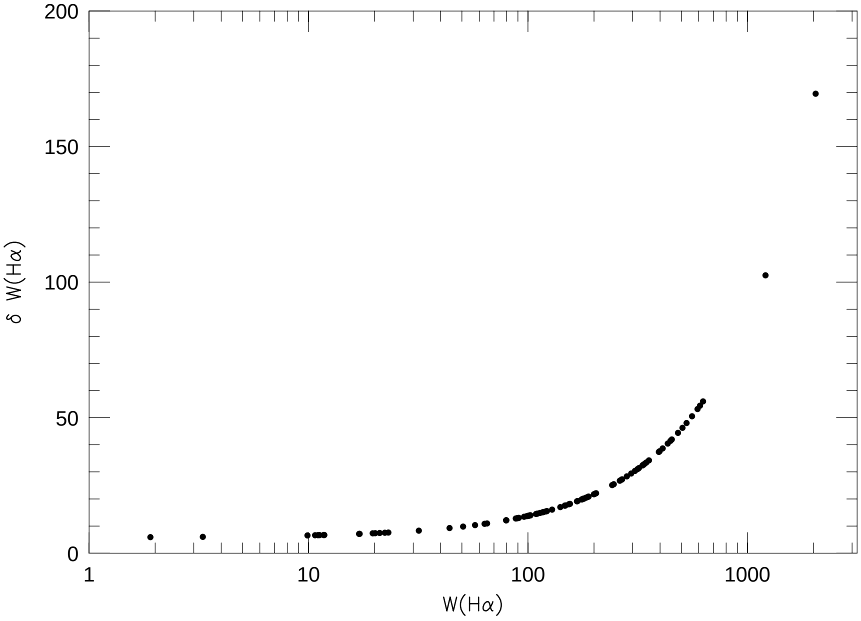

Figure 2.5: Uncertainties as a function of W(Hα) (in Å) for the WIYN data.

2.3 Results

2.3.1 Optical Morphology

Hα emission traces recent star formation activity, and the W(Hα) can be used to estimate the ages of recent episodes of star formation (Leitherer & Heckman 1995). As a stellar population ages, the rate at which it produces H-ionizing photons decreases. For a case B ionization bounded nebulae, the decrease in ionizing photons results in a decrease of the re-emitted Balmer series photons relative to the continuum photons, and the W(Hα) will diminish over time.

The morphology of the Hα emission in the galaxies of HCG 31 is highly irregular and disturbed (Figure 2.1). The interaction site of galaxies A and C has the most prodigious Hα emission of the group, although there are several other locations with substantial values. As well as the main starburst region in AC, there is also star formation on the eastern end of the bar corresponding to galaxy A and some weaker Hα emission coming from the ends of the tidal tails extending to the north-east. The HST images resolve the main starburst region in AC into numerous individual star clusters. Star clusters are also apparent at this resolution throughout the entire body of AC. In addition, possible dust lanes and clumps are present in galaxy A, which allow for the possibility of continued star formation. The star formation in galaxy B has been resolved in several regions, most of which lie in the outer regions of the galaxy closest to and furthest from galaxy AC — thus strongly indicative of the recent star formation in galaxy B being due to tidal activity.

Galaxy E is connected to galaxy AC by a string of star-forming regions that may be too small to be called galaxies themselves, but are not clearly associated with either galaxy AC or galaxy E. Galaxy E itself appears to have two components — on the eastern side there is a region of very recent star formation, and on the western side there is a region which has no Hα emission, and seems to be composed solely of an older generation of stars (possibly lending support, in this case, for the stellar dynamical model of TDG formation). The HST images resolve these two components into numerous SSCs and reveal that the younger region is actually much smaller in spatial extent.

Galaxy F is the shy wall-flower of HCG 31, which has been too near a bright star to the north-east to be studied until these high spatial resolution images became available. This “galaxy” has two distinct components which are contained in the same peak of the H I emission (Williams et al. 1991), but which do not appear to be physically connected by either continuum or Hα emission. In fact, the entire galaxy is very faint in the continuum image, but has W(Hα) measures that rival those of the starburst region in galaxy AC. As with galaxy E, the HST images also resolve the two components into several SSCs. The lack of any evidence for an underlying older stellar population may lend credence to the hydrodynamical theories of TDG formation in this case (contrary to galaxy E).

Galaxy G has a roughly spherical shape in the continuum image, but is very asymmetric in its Hα emission with the star forming regions forming a U-shape along the north-west side. There is some Hα emission from the central region of this galaxy, but it is much less intense than the regions along the north-west rim of the galaxy. It has been suggested previously by Iglesias-Paramo & Vilchez (1997) that the strange star formation morphology is created by a pressure/stripping mechanism, similar to the star formation seen in galaxies that are moving through a high pressure medium. Here I propose an alternative way of looking at this mechanism: gas may be preferentially inflowing to galaxy G from the direction of the main body of the H I cloud in which HCG 31 is embedded, regardless of the direction of motion of galaxy G relative to the ambient gas.

There are several small, low surface brightness features with only continuum light between galaxies E, F, and G. As above, these regions are not obviously associated with any of the galaxies in the group, and due to their lack of Hα emission, I interpret them as older populations of stars that were tidally removed from one or more of the galaxies in the group.

2.3.2 Properties of the Super Star Clusters Compared to Models

2.3.2.1 Broad band magnitudes and colors

The colors of SSCs in combination with population synthesis models can yield information about their ages, masses, and extinctions. The best population synthesis models available for interpreting the colors of SSCs are those of Leitherer et al. (1999). Unfortunately, these models do not include the contributions to the filter magnitudes from nebular line emission. Since nebular lines can be very strong for starburst ages less than 10 Myr, and I suspect that many SSCs in NGC 1741 may have such young ages (due to the presence of W-R features, see VC and CLV), nebular line emission may significantly affect the colors. Therefore, we [1] have developed new models based on work presented by Leitherer & Heckman (1995) that include nebular line emission. This has an impact on the colors, particularly colors constructed from the F555W filter. This filter is wider than Johnson V and includes the [OIII]$\lambda\lambda$4959,5007 lines that make substantial contributions to the F555W band flux at ages $\lesssim 4$ Myr.

In Figure 2.6 the $B_{ST} - R_{ST}$ and $V_{ST} - I_{ST}$ color-color plot is shown. In Figures 2.7, the observed $V_{ST} - I_{ST}$ color vs V_{ST} magnitude of the SSCs in NGC 1741 and galaxies E and F are plotted along with the predicted colors and magnitude as a function of age given by the new models containing nebular line emission. I have also plotted the model predictions for stellar light only (i.e., without the nebular line emission). The reddening vector shown is for $A_V = 1$ adopted from the Calzetti et al. (1994) extinction law for starburst galaxies. Since these data *have not* been corrected for internal reddening, one would correct for reddening by moving the data points in the direction of the arrow.

While the locations of many of the SSCs in the color-color plot are consistent with the models that include nebular line emission, the colors of some clusters are not consistent with either set of models. Furthermore, the colors of all the brightest clusters are reproduced by only those models which do not contain nebular line emission. Metallicity (Z) can have a

---

[1] This work was carried out by C. Leitherer, and is presented in Johnson et al. (1999).

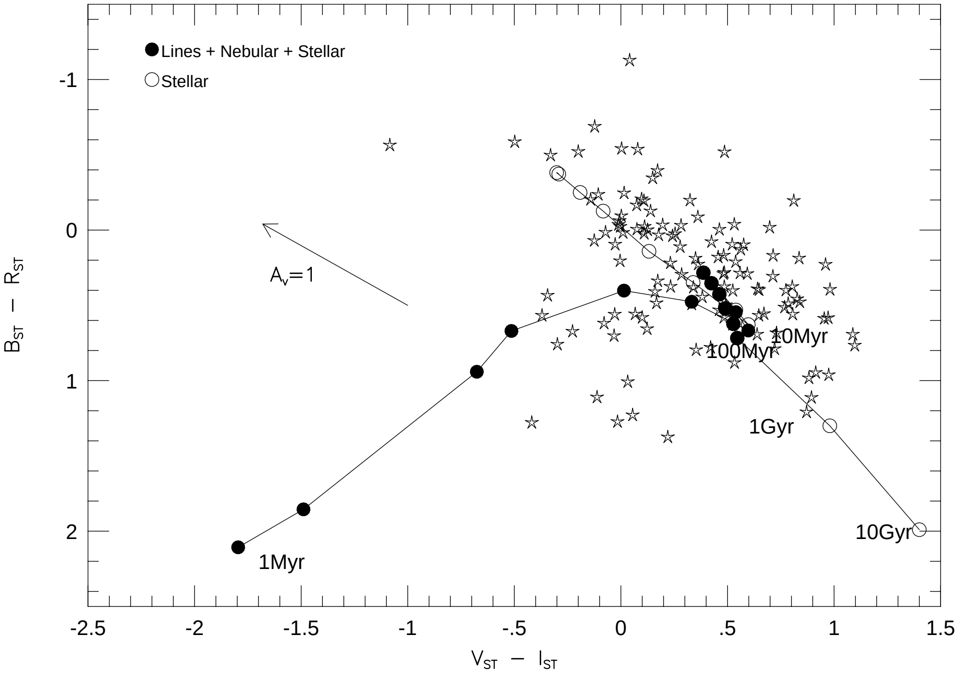

Figure 2.6: Color-color plot for NGC 1741 in the HST magnitude system with a Vega zeropoint. The model including only stellar light are shown with open circles, and the model including stellar and nebular line emission is shown with filled circles.

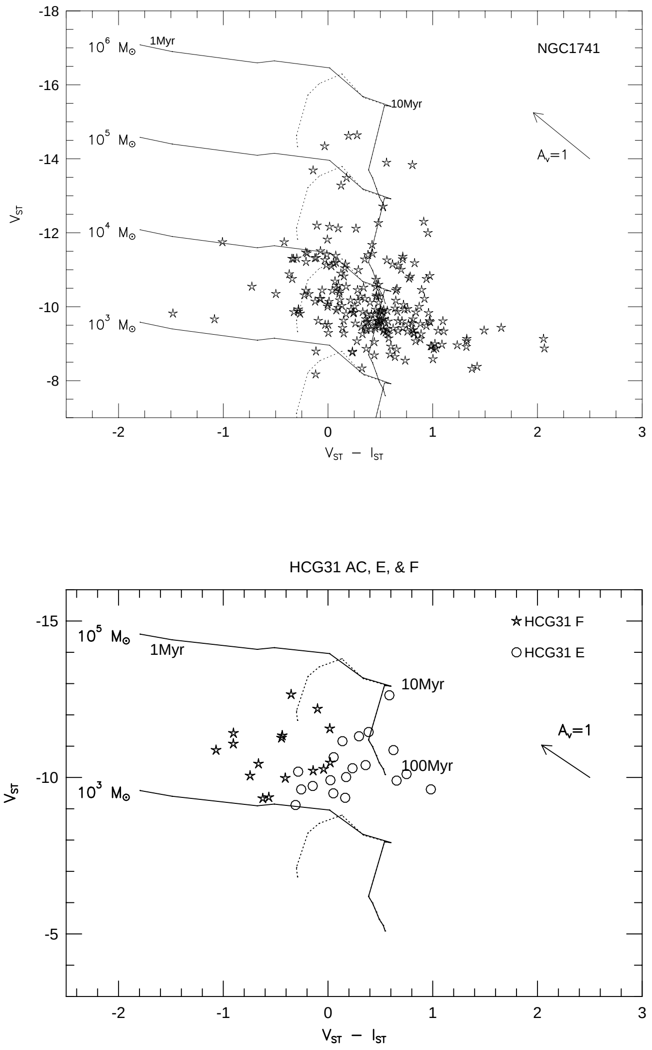

Figure 2.7: V_{ST} vs $V_{ST} - I_{ST}$ plot for the SSCs in HCG 31 (galaxy AC top, galaxies E and F bottom). The burst models for both stellar light and nebular emission are shown for masses of $10^3, 10^4, 10^5$, and 10^6 M$_\odot$, with the models for only stellar light being shown with a dotted line. The youngest and oldest ages of the models shown are 1 Myr and 10 Myr, respectively, with the younger ages being bluer.

significant effect on the colors of starburst galaxies. Cervino & Mas-Hesse (1994) have shown that, for ages between 3 and 10 Myr, M_B and M_V are sensitive to the colors of red supergiants, which in turn are dependent on the metallicity of the galaxy; lower metallicity will tend to make the colors bluer (see also Leitherer & Heckman 1995)). The models plotted here are for 0.25 $Z_\odot$ (the value derived from the [O III] λ4363 line; see VC). It is also important to note that stellar evolution models for red supergiants are notoriously uncertain (Mayya 1997), and the predictions of evolutionary synthesis models with metal-poor red supergiants may not be correct. A second explanation for the anomalous colors of some of the SSCs could be a diffuse nebular *background*, which would be subtracted in V_{ST} (due to the presence of [O III] and Hβ) but *not* in I_{ST} – therefore tending to make the $V_{ST} - I_{ST}$ color redder. This effect would be important if the SSCs had blown away much of their surrounding material in our line of sight, they were not optically thin to the background nebular emission, or we are primarily seeing SSCs on the near side of the galaxy due to extinction.

It is evident from the color-color plots that most of the SSCs in NGC 1741 which have been detected are younger than $\approx$ 10 Myr, regardless of which model is adopted. To estimate the ages, extinctions, and masses of the clusters, I have developed a program that attempts to fit magnitudes derived from population synthesis models (adjusted for reddening) to the observed filter magnitudes. For each source, the age, reddening, and mass are determined from the best fitting (in a least squares sense) model. Using this method, I find the median extinction of the SSCs to be $A_V \approx 0.6$ (E(B-V) ≈ 0.2), which is in reasonable agreement with other studies, the median age to be $\approx$ 4 Myr, and the median mass $\approx 3 \times 10^4$ $M_\odot$. However, one should bear in mind that these are only average values and not representative of any specific SSC.

Although it is possible to put some limits on the ages and extinctions of SSCs using this method, it is not possible to absolutely disentangle age and reddening for any given SSC using only the broad-band colors for two reasons. First, the effects of age and reddening are nearly degenerate. The reddening vector in Figure 2.7 is nearly parallel to the model that includes only stellar continuum, and therefore the colors of older SSCs and more reddened SSCs would be nearly identical to each other in this region. Second, if the SSCs are density bounded rather than ionization bounded, it is not possible to determine *a priori* how much nebular continuum and line emission should be included in the model for a given SSC.

In Figure 2.7, the V_{ST} *vs* $V_{ST} - I_{ST}$ color-magnitude diagram for the SSCs is plotted along with the predicted evolutionary tracks for super star clusters with a range of masses as derived from both sets of theoretical models (purely stellar light and stellar-plus-nebular emission). Note that the models including nebular line emission have simply been scaled to different masses without varying the ionization parameter. The youngest ages are bluest, with $V_{ST} - I_{ST} \approx -1.7$ for models including nebular emission, and $V_{ST} - I_{ST} \approx -0.3$ for the models including only stellar light, at an age of 1 Myr. The models turn over at 10 Myr as the hottest stars from the initial burst die away, and are plotted until 100 Myr. From this plot it is clear that most of the SSCs detected in NGC 1741 have masses between $\approx 5 \times 10^3$ and 10^6 M$_\odot$ depending on the amount of extinction adopted (one should note that these results are for a Salpeter IMF between 1 and 100 $M_\odot$; if the IMF extends below 1 $M_\odot$, these mass estimates will be correspondingly higher). Given the differential extinction in NGC 1741, with quoted values ranging from $0.1 \lesssim E(B-V) \lesssim 0.4$ (Iglesias-Paramo & Vilchez 1997), and the obvious variation in environments throughout the galaxy as seen in Figure 2.3, it is probably inappropriate to assume a single value for the entire galaxy; therefore, I have not applied any correction for intrinsic extinction in the host galaxy.

In Figure 2.7, it is clear that both galaxies E and F have undergone substantial star formation in the past 10 Myr. Moreover, the V_{ST} - I_{ST} colors of the SSCs in galaxy F are offset blueward from those in galaxies A, C, and E. There is no indication of SSCs older than about 4 Myr in galaxy F, and most of the SSC colors are *only* consistent with the models including nebular line emission. The requirement for nebular line emission not only implies that the SSCs are very young, but also suggests there is little, if any, leakage of Lyman continuum photons from them. The mean V_{ST} - I_{ST} color of SSCs in HCG31E is similar to that of HCG31A and C, although there is less of a spread in color. The narrower color dispersion could be due to a smaller range in extinction or a smaller range in ages, both of which are plausible. The V_{ST} magnitudes of each of the 19 SSCs in galaxy E and 16 SSCs in galaxy F imply masses up to $\sim 10^4$ to 10^5 $M_\odot$. These masses are comparable to that of the 30 Dor cluster in the LMC (Meylan 1993, and reference therein). If the amount of star formation scales with the mass of the star clusters, then the total amount of star formation in each of galaxies E and F (the sum of the star formation in their SSCs) is an order of magnitude greater than in 30 Dor.

2.3.2.2 Hα measures

In Figure 2.8 I show the distribution of W(Hα) (in Å) measurements for the SSCs in HCG31 along with the model prediction of W(Hα) with burst age from Leitherer et al. (1999). The predicted W(Hα) decreases rapidly from a value of log(W(Hα)) ~ 3.2 at an age of $\sim$ 1 Myr to a value of log(W(Hα)) ~ 0.3 at an age of $\sim$ 10 Myr. I should stress that these ages are really upper limits due to geometrical dilution — the models are derived for a single stellar population, but any underlying older population in the aperture will contaminate the measurement causing the W(Hα) to decrease.

The W(Hα) sources are predominantly very young (less than 10 Myr) with a peak in the distribution corresponding to ages of about 5 Myr. Figure 2.9 illustrates the W(Hα) distribution from each of the galaxy components. Galaxies AC, B, and G all show signs of star formation over the the past $\sim$ 10 Myr, with each of them showing a peak in the W(Hα) distribution corresponding to star formation about 5 Myr ago (consistent with the average result found from broad band photometry). Galaxy B also shows a second peak in the W(Hα) distribution which is indicative of substantial star formation in its SSCs about 10 Myr in its past. Galaxies E and F are both much smaller and have not experienced star formation on as large a spatial scale as the other group members. The distribution of W(Hα) present in the SSCs of galaxy E show evidence for star formation as recent as 1 - 3 Myr ago as well an older population similar to the ages found in galaxies AC, B, and G. Galaxy F, however, has *only* very strong W(Hα)s, indicating substantial star formation less than 4 Myr ago.

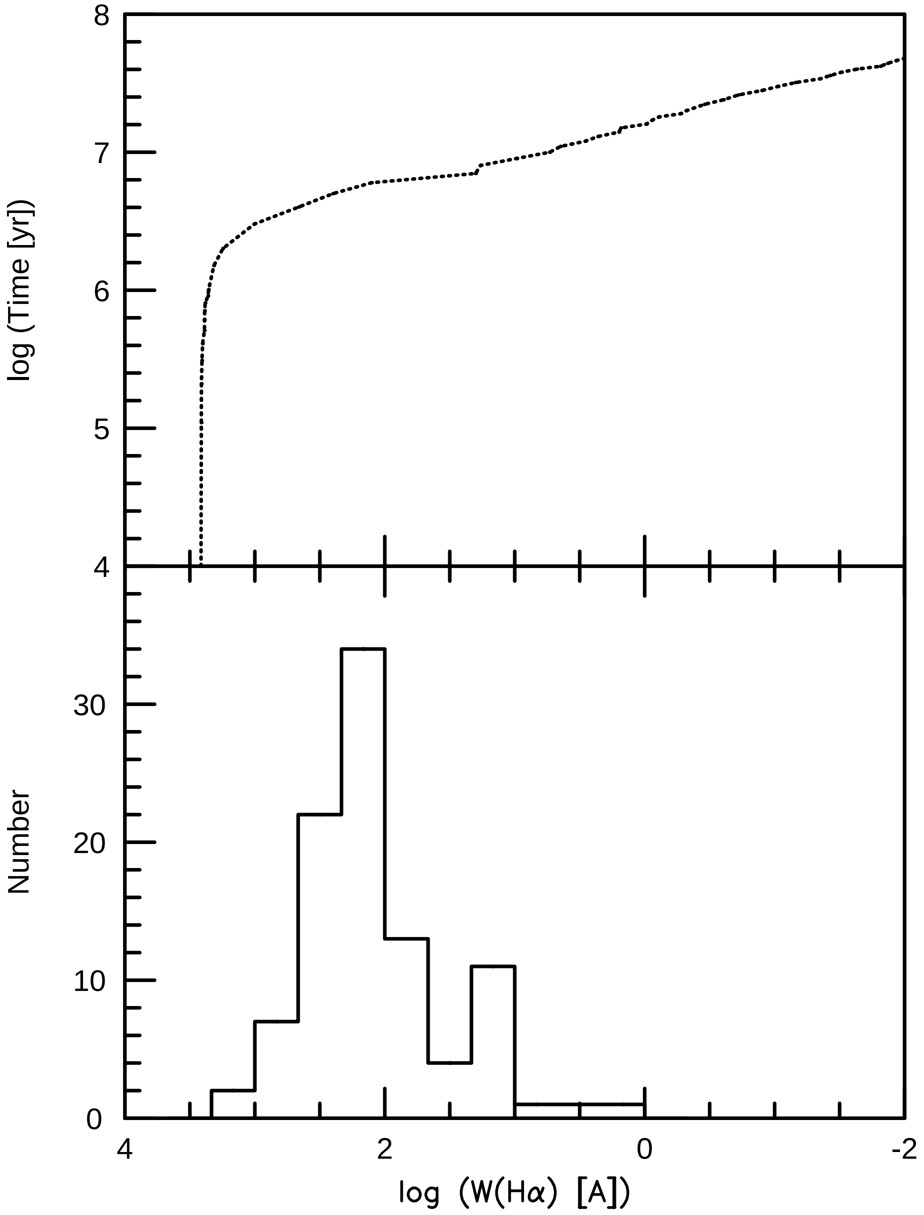

Figure 2.8: Model predictions from Leitherer et al. (1999) for W(Hα) vs. age are shown (top) along with a histogram of the W(Hα) values for SSCs in HCG31 (bottom).

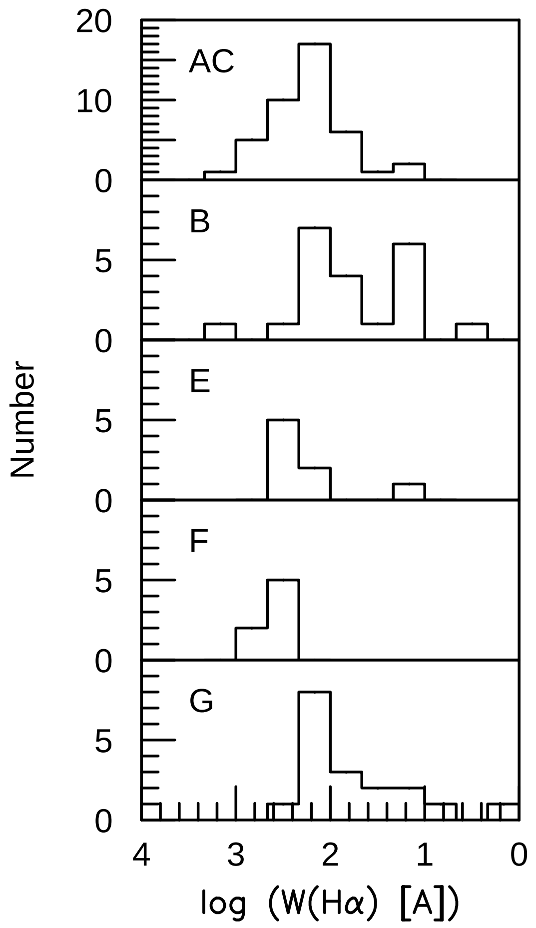

Figure 2.9: A histogram of the W(Hα) values for SSCs in each of the member galaxies of HCG31. Higher W(Hα) values correspond to younger ages.

Because the observing conditions were not photometric, I was not able to determine absolute Hα luminosities; I refer the reader to Iglesias-Paramo & Vilchez (1997) where they measured Hα luminosities for several starburst regions in HCG31.

2.3.3 Luminosity Functions of the Super Star Clusters

The V-band luminosity function (LF) for the SSCs in NGC 1741 is shown in Figure 2.10 with magnitudes presented in the Johnson system to facilitate comparisons with previous work (the small number of SSCs in galaxies E and F undermine the statistical usefulness of performing this exercise on these galaxies). Detections beyond the completeness limit are shown by a dotted line. The dashed line shows a power-law fit of the form $\phi(L) \propto L^{-\alpha}$ over the range from $M_v = -15.2$ mag to the completeness limit of $M_v = -9.4$ mag, where I also expect the brightest individual stars of NGC 1741 to start contributing to the LF (see below). No attempt has been made to account for confusion, but it is possible that confused sources may flatten the LF by a small amount. The best fit was determined by the method of least squares with the data weighted by Poisson statistics. The best-fit power-law index was found to be by $\alpha = 1.85 \pm 0.04$. There is no indication of a turnover in the luminosity function brightward of our completeness limit.

In Figure 2.11 the Johnson $V - I$ color distribution for the SSCs is shown. The mean value was found to be $V - I = 0.41$ with a dispersion of 0.49. As will be discussed in § 3.4, these values can be used to place the SSCs in NGC 1741 in context with other starburst galaxy cluster systems.

2.3.4 Cluster Radii

The radii of the sources were estimated in a manner similar to that of Whitmore et al. (1993). First I created artificial Gaussian “sources” with effective radii in the range of 0.01-10 pixels. These artificial sources were then convolved with the PSFs of the three filters to mimic how the sources would appear in the HST images. The magnitudes of these test objects were

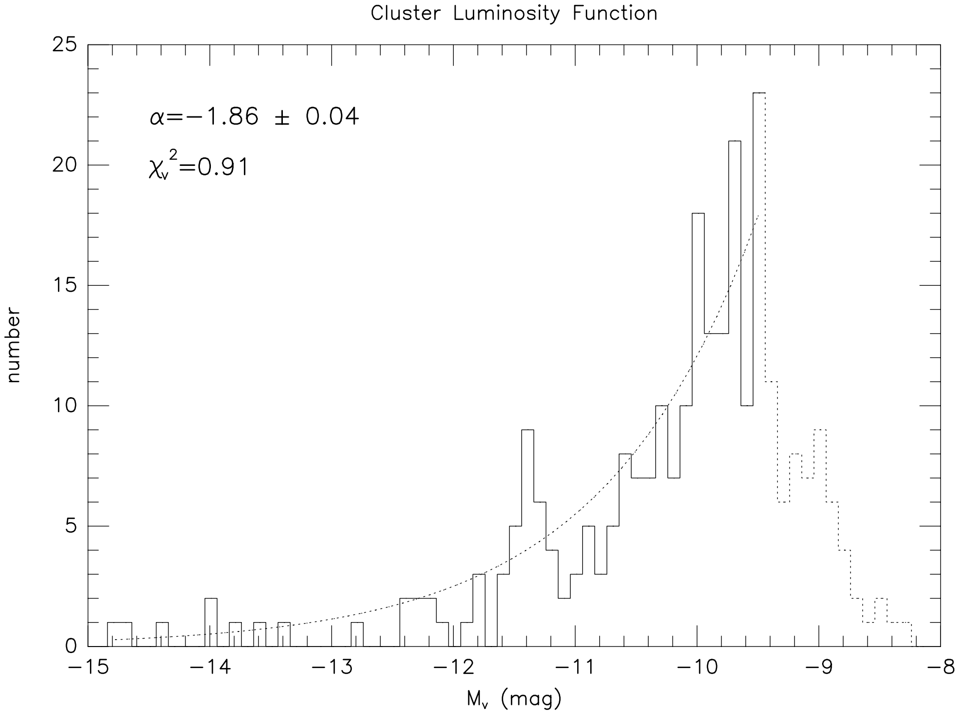

Figure 2.10: The V luminosity function of the SSCs in NGC 1741 in the Johnson-Cousins system. Magnitudes fainter than the completeness limit are shown with a dotted line. For M_V less than the completeness limit, the LF is well fit by a power law of the form $\phi(L) \propto L^{-\alpha}$.

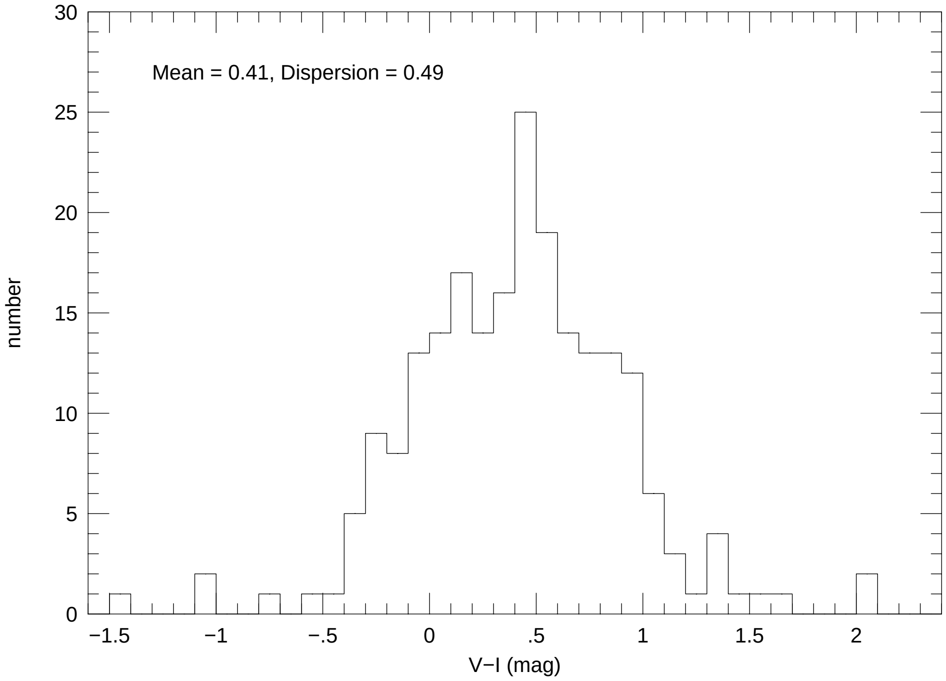

Figure 2.11: The $V_{ST} - I_{ST}$ histogram in the Johnson-Cousins system. No internal reddening correction has been applied.

then measured for several aperture values, and the differences in magnitude between apertures of varying size were computed to determine which combination of apertures could best be used to estimate the true size of the sources. In accord with Whitmore et al. (1993), I found that the difference between the radii of r=0.5 and r=3 pixel apertures gave good results. However, at radii values $\gtrsim 3$ pixels, this magnitude difference becomes nearly degenerate, and radii larger than this value have extremely large uncertainties. The relation between the $\Delta_{0.5-3}$ magnitudes and the effective radii for the F555W image is shown in Figure 2.12.

These test objects were then inserted into the actual F555W, F658N, and F814W images at 50 random locations, and $\Delta_{0.5-3}$ was measured to determine whether this method would be reliable for the sources. The $\Delta_{0.5-3}$ values found from this procedure had standard deviations of ~ 0.1, with the most inconsistent results coming from crowded regions or locations with sharply varying backgrounds — both of which will tend to cause the sources to appear larger than they actually are. However, overall this method proved to be quite reliable. The radii measurements determined for the sources in the F555W filter are shown in Figure 2.13. Most (90%) of the sources have radii values smaller than 3 pc, consistent with most of them being unresolved. As Whitmore et al. (1993) and others have found, the effective radii of the brighter SSCs appear to be larger near the central starburst region; there is also some evidence for this trend in the present data. However, because of the substantial crowding and variable background present almost ubiquitously in strong starbursts, I believe this to be an artifact of the method and not likely to reflect the physical sizes.

2.3.5 The Burst Luminosity

The percentage of the total luminosity due to the SSCs can be determined by summing the total flux of the clusters, and dividing by the total flux of the underlying galaxy. However, there are two complicating factors. As the luminosity function illustrates, there is no indication of a turnover at or above our completeness limit, and the number of fainter SSCs present but not detected may continue to rise below our completeness limit. Due to the number of fainter SSCs

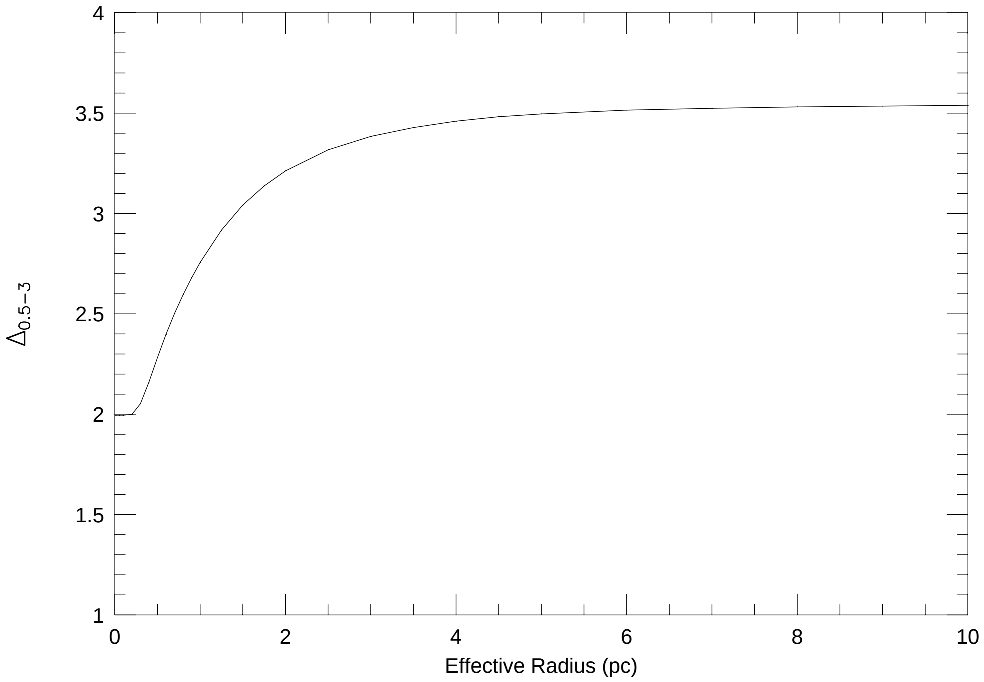

Figure 2.12: The relation between the $\Delta_{0.5-3}$ magnitudes and the effective radii for the V_{ST} filter.

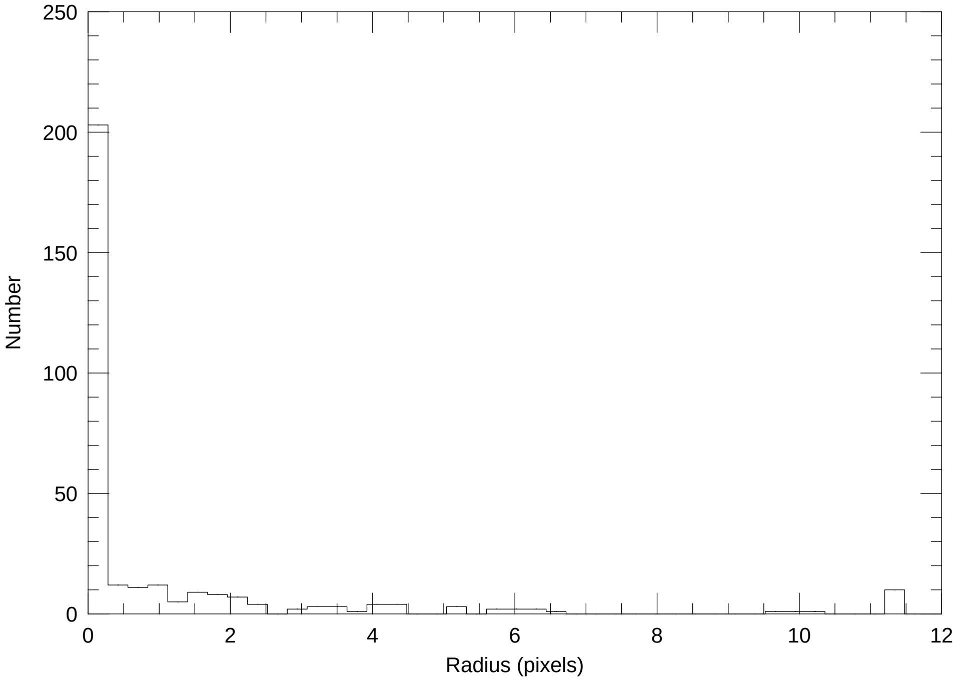

Figure 2.13: The radii estimated for the super star clusters in NGC 1741 in the V_{ST} filters using the method described in the text. Most of the sources are clearly unresolved. Although a few may be marginally resolved, they are consistent with being point sources within the uncertainty. As shown in Figure 2.12, the method used to estimate these radii is strongly degenerate for radii greater than approximately 3 pc.

which may be excluded from this sample, the total burst luminosity is uncertain and should be treated as a lower limit. The second complication is that defining the boundary of the galaxy is not straightforward. Customarily the Holmberg radius (the level at which the surface brightness is 26.5 mag arcsec^{-2}) is used to determine the boundary. In his original survey to catalog compact groups of galaxies, one of Hickson's criteria was that the mean surface brightness be $<$ 26.0 (Hickson 1982), therefore for many galaxies within Hickson Compact Groups it is not possible to use the Holmberg radius. In the case of NGC 1741, the surface brightness never drops below this threshold anywhere on the PC chip. Another method commonly used is to define the 3σ contour as the boundary of irregular galaxies. However, this method depends on the signal to noise of the observation and therefore cannot be a consistent and reliable method for the purpose of defining the boundaries of galaxies.

Hickson (1982) determined that the average surface brightness on red photographic plates of HCG 31 is 21.9 ± 0.5 mag arcsec^{-2}. This value was used to differentiate between galaxy flux and background flux. The flux inside this contour was calculated and the resulting colors are consistent when converted to the same magnitude system with those previously published (Iglesias-Paramo & Vilchez 1997), $B_{ST} - V_{ST} = -0.02, V_{ST} - I_{ST} = 0.61, B_{ST} - R_{ST} = 0.50$. However, these values are highly dependent on the isophotal contour used to define the galaxy as shown in Figure 2.14. The percentage luminosity of the starburst clusters is 5.1% in B_{ST}, typical of what has been found for other starburst systems. Meurer et al. (1995) measured the fractional light contribution to the total light at 2200 Å of 85 star clusters in 9 starburst galaxies. On average, $\sim$20% of the UV light comes from clusters. Since super star clusters are bluer than the main body of the galaxy, this fraction is expected to decrease at longer wavelengths. Therefore the 5% contribution in B_{ST} by clusters in NGC 1741 is quite typical of that for starburst galaxies.

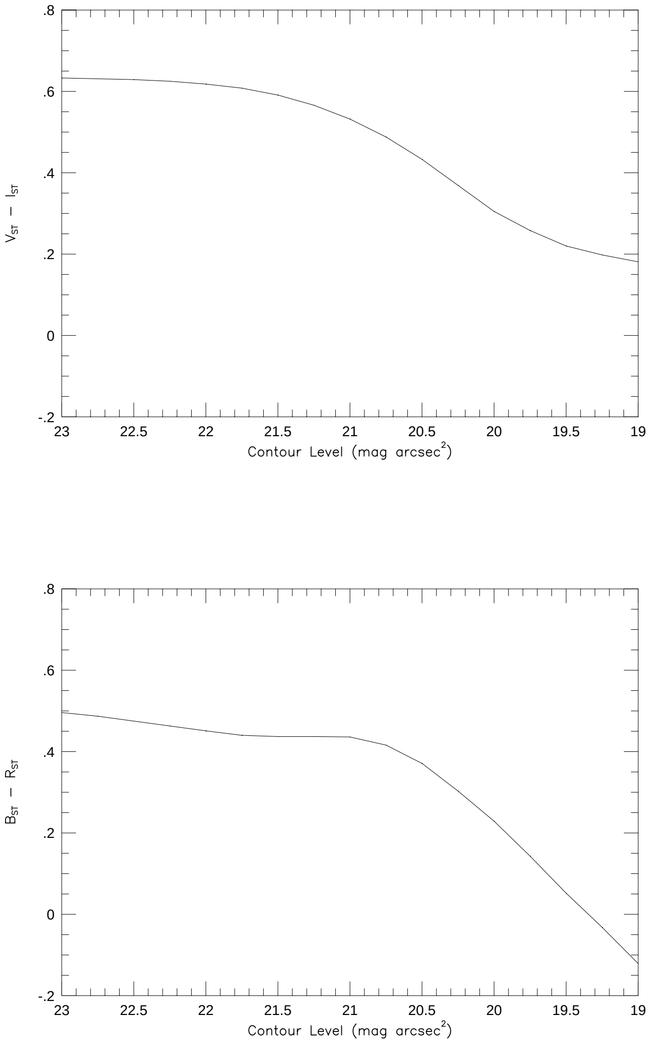

Figure 2.14: The isophotal dependence of the $V_{ST} - I_{ST}$ and $B_{ST} - R_{ST}$ colors for the integrated light from NGC 1741. It is clear that the derived colors of the galaxy are dependent on the boundary used.

2.4 Discussion

I now address several issues concerning the galaxies in HCG 31, including their dynamical state, the properties and future of the SSCs, and the relevance to galaxies recently discovered at redshift $z \approx 3$. Although broad-band imaging alone does not allow us to address in detail some of the interesting issues involving star formation in HCG 31, it is possible to gain substantial insight from the estimates provided by the results presented in this chapter.

2.4.1 The Star Formation History of HCG 31

It was previously noted by Iglesias-Paramo & Vilchez (1997) that all of the galaxies in HCG 31 appear to have undergone their most recent episode of star formation almost simultaneously; they suggest the interaction of galaxies A and C was the triggering mechanism. The results in this chapter would also seem to support contemporaneous star formation ~ 5 Myr ago. However, it is unclear how instantaneous star formation could occur on such a short time scale over such a large volume. Given the size of HCG 31 (~ 50 kpc), it would take ~ 1 Gyr for a super sonic shock speed of 50 km s^{-1} to propagate from one side of the group to the other (at a typical sound speed of ~ 10 km s^{-1} this propagation would take correspondingly longer; for a discussion of star formation triggered by shocks see Vanhala & Cameron 1998, and references therein). Furthermore, an interaction time scale of ≈ 400 Myr can be derived based on the length of the tidal tails and the rotation velocity (J. Hibbard, private communication).

Therefore, if this merger has been occurring for the past 400 Myr we are left with four alternatives: (1) the group-wide recent peak in star formation is a coincidence; (2) the formation of starbursts is a relatively recent event in the merger process, which implies there is a very special time during the merger process; (3) there is some mechanism at work which does not rely on shock propagation that has caused simultaneous and recent star formation throughout HCG31; or (4) we are seeing only the most recent star formation, although star formation has been occurring all along.

Although the first interpretation cannot be ruled out with certainty, *something* had to trigger star formation in galaxies F and G that are quite distant from the main site of interaction in galaxy AC. This is irrespective of whether the star formation has been occurring all along in the HCG31 history or is a recent event.

Given the undoubtedly complicated history of HCG 31, the second interpretation is plausible, but puzzling. For example, the complex velocity field of HCG 31 (Rubin et al. 1990) suggests that neutral hydrogen flows are likely to intersect at speeds of several hundred km s^{-1}, shock-heating the gas that then expands to fill the potential well of the group (Barnes 1997). If the gas was too tenuous to cool rapidly, star formation could have been abated and/or delayed. Under these conditions, it is possible that HCG 31 is undergoing a small scale cooling-flow similar to those inferred for some large galaxy clusters (see Fabian 1994, and references therein). This physical scenario might also be reflected in numerical simulations that have shown that tidal material can remain bound to the merger system and return at later times (Barnes 1988; Hernquist & Spergel 1992; Hernquist 1992, 1993). This process might lend support to the third possibility that star formation has been simultaneously triggered by something other than shocks.

The fourth possibility, that the older regions of star formation are simply not detected, is undoubtedly true to some degree. The galaxies in the group almost certainly been undergoing some level of star formation during the last crossing time of the group as the ambient gas was torqued, shocked, and rapidly cooled thereby fueling star formation (Barnes & Hernquist 1991, 1996). From the population synthesis models it is possible to estimate the amount a starburst will fade due to evolution. For ages between 10 and 100 Myr, a cluster will fade by $\approx$ 3 magnitudes; therefore, anything initially fainter than $M_V \approx -11.5$ will be fainter than our completeness limit at 100 Myr. Thus, many SSCs at that age are unlikely to be detected. However, several SSCs brighter than $M_V \approx -11.5$ are detected in NGC 1741 at this time and there are relatively few SSCs with ages consistent with $\gtrsim$ 10 Myr. Moreover, by the time a burst has aged to 10 Myr, there will be virtually no Hα emission, and the continuum emission will have also faded by $\sim$ 1 magnitude from its initial value (see the model predictions shown in Figures 2.7 and 2.8). In fact, because the affects of age and reddening cannot be unambiguously disentangled, several of the SSCs in galaxies AC and E are not inconsistent with having ages $>$ 10 Myr (Figure 2.7). However, the bulk of them are young. The broad band colors of galaxy F show no sign of star formation that could be older than $\sim$ 4 Myr. Nevertheless, the possibility that we are not dectecting the older star forming regions is viable within the completeness limit.

2.4.2 On the Youth of Galaxy F

As I have briefly discussed above, galaxy F appears to be the youngest galaxy in the group. The broad-band colors of its SSCs are *only* consistent with a burst age of less than $\sim$ 4 Myr and it is the only galaxy in the HCG 31 that has only strong W(Hα) measurements indicative of SSC ages no older than $\sim$ 4 Myr. The fact that the broad-band colors might be affected by some internal reddening and that the W(Hα) measurements may have been geometrically diluted only serves to decrease the age of the starburst in galaxy F.

If galaxy F was seeded from tidal debris in the inter-group medium, then it is likely that there is some older, underlying stellar population that was stripped from a parent galaxy in the group. We can neither confirm nor deny this possibility with our current data. However, in color images constructed from the WFPC2 filters, galaxy F is uniformly blue, even in lower surface brightness regions with no SSCs. In contrast, galaxies AC and E, for which I have also made three-color images, have blue starburst regions, but also show an underlying red (and therefore older) stellar population. It would be useful to obtain deep far red or near IR spectra of galaxy F in order to look for signatures of an older stellar population. Galaxy F may be a good example of star formation triggered by collapse of molecular cloud material in the tidal tails, as proposed by Elmegreen et al. (1993).

2.4.3 Globular Cluster Formation?

The characteristics observed for HCG 31, including the enhanced star formation, complex morphology (including tidal tails), large-scale gradients in the H I map, and low velocity dispersion of the group, suggest that HCG 31 is in the process of forming a single galaxy. In fact, simulations (e.g., Barnes 1989) have shown that loose groups will evolve into compact groups, which then typically merge into an elliptical galaxy. Such a scenario has direct implications for the interpretation of the SSCs in HCG 31. It has been observed that the number of globular clusters per unit galaxy luminosity varies with the morphological type of the host galaxy, with elliptical galaxies typically having a factor of 5 increase from the number seen in late-type spirals. van den Bergh (1995) has argued based on the conservation of globular clusters, that elliptical galaxies are not the merger remnants of spiral galaxies. However, if globular clusters are formed during merger events, it may provide a simple explanation for the observed abundance of globular clusters in ellipticals (Ashman & Zepf 1992).

In fact, there is now growing evidence that globular clusters (GCs) are indeed formed in galactic interactions and mergers (Whitmore et al. 1993; Whitmore & Schweizer 1995; Meurer et al. 1995; Schweizer et al. 1996). One question I wish to address is how the properties of SSCs compare to those of GC systems of various ages. An evolutionary scenario relating SSCs to GCs is developing in the literature based on luminosity functions, colors, radii, and masses of observed systems in a variety of evolutionary states. I now add NGC 1741 to this picture as a critical point for understanding the earliest stages of globular cluster formation.

The luminosity function of SSCs in NGC 1741 is well fit by a power law of the form $\phi \propto L^{-1.85\pm0.04}$, and shows no sign of turning over brightward of the completeness limit at $M_V = -9.4$. This is consistent with the luminosity functions of other young clusters, with exponents $\alpha \approx 1.7 - 2.1$ (Vacca 1997; Schweizer et al. 1996; Whitmore & Schweizer 1995). The luminosity function of galactic halo-type globular clusters with ages of ≈ 15 Gyr is roughly Gaussian, with a peak magnitude of $M_V \approx -7$, and therefore the lack of a turnover observed in young systems such as NGC 1741 is significant. If globular clusters evolved from SSCs, evolutionary models predict a peak at $M_V \approx -10$ to -12 (depending on the amount of extinction and the Hubble constant), which is at least 1.6 magnitudes brighter than our completeness limit. However, there is no evidence for this turnover in our data.

One explanation for the lack of a turnover in our data is that most of the SSCs with $M_V \gtrsim -10$ may be disrupted as they age and evolve. Possible mechanisms for disruption include two-body relaxation, tidal shocking, and dynamical friction. The time scale for an SSC to disperse can be estimated by the dynamical time based on the virial theorem given by

$$t_{dyn} \approx 0.15(R_{eff}^3/M_5)^{0.5} \text{ Myr}$$

where R_{eff} is the effective radius in pc and M_5 is the mass of the SSC is units of $10^5 M_\odot$ (Vacca 1997). Given that the SSCs in NGC 1741 are unresolved, it is possible only to put an upper limit on the radii of ≈ 17 pc. However, resolved SSCs typically have radii of ≈ 10 pc or less (Schweizer et al. 1996; O'Connell et al. 1995; de Marchi et al. 1997) and this value is adopted. As Figure 2.7 illustrates, the masses of the SSCs in NGC 1741 for a Salpeter-type IMF with an upper and lower mass cutoff of $100 M_\odot$ and $1 M_\odot$ typically range between $5 \times 10^3 M_\odot < M < 10^6 M_\odot$, consistent with the value of $10^5 M_\odot$ recently derived by Smith & Gallagher (2001) for SSCs using velocity dispersions and the assumption of virial equilibrium. For our mass range, the equation for t_{dyn} yields dynamical times of 20 Myr and 1.5 Myr respectively. Since SSCs with ages older than the dynamical time can be considered bound, certainly some of SSCs I have observed fit this criterion. However, most of the SSCs in NGC 1741 are younger than 20 Myr, and it is not possible to demonstrate whether they are bound using this method.

2.4.4 Comparison to Other Starburst Systems

It is useful to compare the properties of HCG 31 with those of other starbursts that have been observed with HST. Schweizer et al. (1996) have observed a trend among merger systems in which the mean $V - I$ color of SSCs shifts from blue to red as the state of the merger progresses. The mean value of $V - I = 0.41$ for the SSCs found in NGC 1741 is bluer than the youngest system currently available in their sample, NGC 4038/39, which has a mean $V - I = 0.34$ after a reddening correction of -0.26 mag. It is important to note that the values for NGC 1741 have *not* had any reddening correction applied. Therefore, NGC 1741 provides some of the youngest SSC systems currently available for study.

How does the star formation rate in NGC 1741 compare that in other starburst galaxies? Gallagher et al. (1984) showed that the absolute blue luminosity is a useful tracer of this quantity, although this method suffers from the obvious drawback that it must underestimate the star formation rate to some extent due to the absorption of blue light by intervening dust. However, the longer wavelength light (which is less likely to be extincted) also includes an increasingly larger contribution from the older, evolved stellar population — therefore causing an overestimation of the recent star formation rate. Using the Starburst99 models of Leitherer et al. (1999), I can directly translate the B magnitude of NGC 1741 into a star formation rate. The B magnitude of the entire galaxy system (galaxies A + C) is $M_B = -20.3$. If the star formation has been continuous over the last 10 Myr, this magnitude implies a star formation rate of 11.4 $M_\odot$ yr^{-1}. If I estimate the projected surface area of NGC 1741 to be $\sim$ 40 kpc^2, I find a star-formation rate per unit surface area of 0.3 $M_\odot$ yr^{-1} kpc^{-2} for a Salpeter IMF between 1 and 100 $M_\odot$ (again note that if the IMF extends below 1 $M_\odot$, these star formation rates will be correspondingly higher). However, the "burst" of star formation in NGC 1741 is not globally distributed in the galaxy, rather it is predominantly taking place at the region of interaction between galaxies A and C. The blue magnitude of this region alone is $M_B = -19.8$ over an area $\approx$ 10 kpc^2. The corresponding star formation rate for this region is 7.2 $M_\odot$ yr^{-1} or 0.7 $M_\odot$ yr^{-1} kpc^{-2}.

Meurer et al. (1995, 1997) found that UV bright starburst galaxies have a very narrow range in areal star-formation rate. In particular, they find an upper limit of 1.5 $M_\odot$ yr^{-1} kpc^{-2} (M_{low} = 1 $M_\odot$). The burst region in NGC 1741 follows the relationship of Meurer et al. The areal star-formation rate of 0.7 $M_\odot$ yr^{-1} kpc^{-2} is comparable to those found for the dwarf starbursts NGC 3991 (0.8 $M_\odot$ yr^{-1} kpc^{-2}) or Tol 1924-416 (1.2 $M_\odot$ yr^{-1} kpc^{-2}). Furthermore, this burst region of NGC 1741 has a star formation rate comparable to the typical values for the total star formation rates of $\approx 10\ h_{50}^{-2}$ $M_\odot$ yr^{-1} for the high-redshift sample of Steidel et al. (1996) and Lowenthal et al. (1997) (moduli the surface areas of the galaxies in those samples) , which justifies the status of NGC 1741 as a local template. For comparison, the star-formation rates per unit surface area in normal disk galaxies (including the Milky Way) are about three orders of magnitude lower (Meurer et al. 1997). NGC 1741 is a genuine starburst indeed!

Chapter 3

The Case of Henize 2-10

3.1 Background

Another galaxy in which we can study the starburst phenomenon and the formation of super star clusters in Henize 2-10 (He 2-10). He 2-10 is a blue compact dwarf galaxy with strong nebular features first detected in an Hα survey of the southern sky (Henize 1967) and was initially believed to be a planetary nebula. It has been the subject of numerous investigations since Allen, Wright, & Goss (1976) first found the signatures of W-R stars in its integrated optical spectrum, thus making He 2-10 the first known "Wolf-Rayet galaxy". At a distance[1] of 9 Mpc ($H_0 = 75$ km s^{-1}Mpc^{-1}; Vacca & Conti 1992), He 2-10 is relatively nearby, and has an optical diameter of $\sim$ 2.8 kpc. He 2-10 has a high molecular gas content of $\gtrsim 10^8$ M$_\odot$ (Kobulnicky et al. 1995) and correspondingly high metallicity $\gtrsim 1 Z_\odot$ (Kobulnicky et al. 1999).

The starburst activity in He 2-10 is concentrated in two regions, A and B (Vacca & Conti 1992), separated by $8''$ ($\sim$ 350 pc); the former is roughly at the optical center of the galaxy, the latter almost directly east. W-R features were found in region A but not in region B (Vacca & Conti 1992; Schaerer et al. 1999a). Using HST FOC images of He 2-10, Conti & Vacca (1994) found that both starburst regions were composed of intense knots of (massive) stars. Recent narrow band Hα images of Méndez et al. (1999) reveal a kiloparsec-scale bipolar outflow centered on region A, the most intense star forming region in the galaxy. This result indicates

---

[1] Distances have been suggested between 6 Mpc (Johansson 1987) and 14 Mpc (Allen et al. 1976) depending on the choice of Virgocentric inflow model and H_0.

that the recent starburst episode in He 2-10 has had a significant effect on its interstellar medium and local environment.

The nature and history of the starburst in He 2-10 has been a subject of considerable discussion in the literature. Johansson (1987) proposed that this starburst was the result of two merging dwarf irregular galaxies. However, based on the smooth elliptical envelope well fit by an $r^{1/4}$ law, Corbin et al. (1993) argued that the starburst activity is within a single dwarf elliptical galaxy undergoing stochastic star formation. Kobulnicky et al. (1995) detected a molecular cloud extending to the south-east of the center of the galaxy, which is possibly falling into the center of the galaxy and triggering the star formation.

Although the UV images of Conti & Vacca (1994) revealed the presence of SSCs in the center of He 2-10, the estimation of their masses and ages required several assumptions, not the least of which was the correction for internal extinction. Furthermore, ground-based images of this object lack the resolution needed to study the properties of the individual knots. In §3.2 I present high spatial resolution optical images of He 2-10 obtained with HST. I determine some of the parameters of the SSCs and consider the dust morphology of the starburst regions in §3.3 using optical photometry. I will discuss the results, including the effect He 2-10 may have on the intergalactic medium, in §3.4.

3.2 Observations and Data Reduction

Optical images of He 2-10 were obtained on 1997 March 4 using the Wide Field and Planetary Camera (WFPC2) aboard the Hubble Space Telescope (HST). Images were acquired through two broad-band optical filters (F555W and F814W) and one narrow-band filter (F658N), which corresponds to redshifted Hα. In each filter, a set of exposures (2×400 sec and 1×30 sec) were taken at each of two dithered positions. The 30 sec exposures were taken in case of saturation on the 400 sec exposures; however, none of the galaxy images were saturated in the region of interest, and the 30 sec exposures were not used. The dithering was done to regain some of the spatial information lost by the under-sampling of the point spread function (PSF) by WFPC2.

Both star-forming regions He 2-10 are completely contained on the PC, so we have not analyzed the WF region of the images. The PC images were reduced following standard pipeline procedures (including the application of bias, dark, and flat field frames) using the Image Reduction and Analysis Facility (IRAF) and the Space Telescope Science Data System (STSDAS). A correction for geometric distortion was applied to the images as prescribed by Holtzman et al. (1995a), and the pairs of 400 sec images were combined using the STSDAS task GCOMBINE, which also removes hot pixels and cosmic rays. The dithered images were then combined using the "shift-and-add" technique: the images were block-replicated, dithered offsets between these images were determined by the STSDAS task CROSSCOR, the images were shifted by an integer number of pixels, and then the dithered pairs were combined. This process resulted in final images of sizes 1600 × 1600 pixels with 1 pixel $= 0''.02277$. The PHOTFLAM keyword in the image header was used to determine the photometric zeropoints, with resulting magnitudes in the STMAG system. These magnitudes were then shifted to a Vega zero point in order to facilitate comparisons, and we refer to them as V_{ST} Hα_{ST} and I_{ST} (Holtzman et al. 1995a).

Using the Schlegel et al. (1998) maps of infrared dust emission, we infer a Galactic extinction of E(B-V) = 0.11 at the position of He 2-10 (which has a Galactic latitude of $l = 8.7^{\circ}$). In what follows, we have adopted this foreground extinction and a distance modulus of Δm$= 29.8$. As we only have two broad-band magnitudes, no correction for internal extinction has been applied to these data. Local reddening is likely to be highly variable across He 2-10, as is evidenced in Figure 3.1 and will be discussed in §3.3.1.

Several hundred (mostly point-) sources were identified in each of the filters using the IRAF task DAOFIND. A detection criterion of $\geq 5\sigma$ above the local background level was used to identify sources; below this threshold the number of spurious detections was uncomfortably large (more than $\approx$ 15% would have been rejected upon visual examination). The detections in each filter were then visually inspected to check the identification, and a few sources were

Figure 3.1: A multi-color image of He 2-10 constructed using the F555W, F814W, and F658N images. F658N is shown in red, and therefore a blue-green color in the image should be interpreted as continuum. The scale of this image is approximately 1.3 kpc on a side.

added or deleted from the list. This process resulted in 649 detections in the F555W image, 144 in the F658N image, and 698 in the F814W image. The identifications in the three filters were then cross-identified, with the final list consisting of 855 individual sources detected in one or more of the three filters.

The sources *a priori* can be either SSCs or luminous supergiants (as discussed in Chapter 2)). Following Whitmore et al. (1999), I adopt $V_{ST} = -8.5$ as an effective *upper* limit to single star absolute magnitudes. This limit is also in accord with the estimated magnitudes of the brightest stars in nearby spiral galaxies (Sohn & Davidge 1996). Thus all sources brighter than this magnitude are assumed to be SSCs in what follows. There are undoubtedly fainter SSCs in our source sample but they cannot unequivocally be separated from individual supergiants. I find 76 sources sufficiently bright to be called SSCs.

Since the only Galactic foreground star in the images is saturated (even on the 30 s exposures in the F555W and F814W filters), a PSF could not be constructed using field stars. In the case of the F555W and F814W filters, PSFs were built using six images from the PSF library taken closest to the time of our observation. No library images were available for the F658N filter, so we used those of a stellar field taken with this filter found in the HST archive close to the date of our exposures. Photometric measurements were made using the aperture photometry routine PHOT with an aperture size of 4 pixels and a background annulus of 8-10 pixels, and aperture corrections were applied based on the PSFs for each filter. Errors as a function of magnitude for V_{ST} and I_{ST} are shown in Figure 3.2.

Completeness limits were determined for each filter by a method similar to that described in Chapter 2. Artificial "stars" were created using the PSF with known magnitudes distributed randomly in magnitude space spanning a range of 2-3 magnitudes over our estimated completeness limit. For each magnitude bin, 500 of these artificial stars were added to the image using the IRAF task ADDSTAR, one at a time, at randomly selected coordinates, and avoiding the exact coordinates of previously identified objects in the field. We then attempted to recover each star using the DAOFIND parameters originally used to identify objects in each filter. The

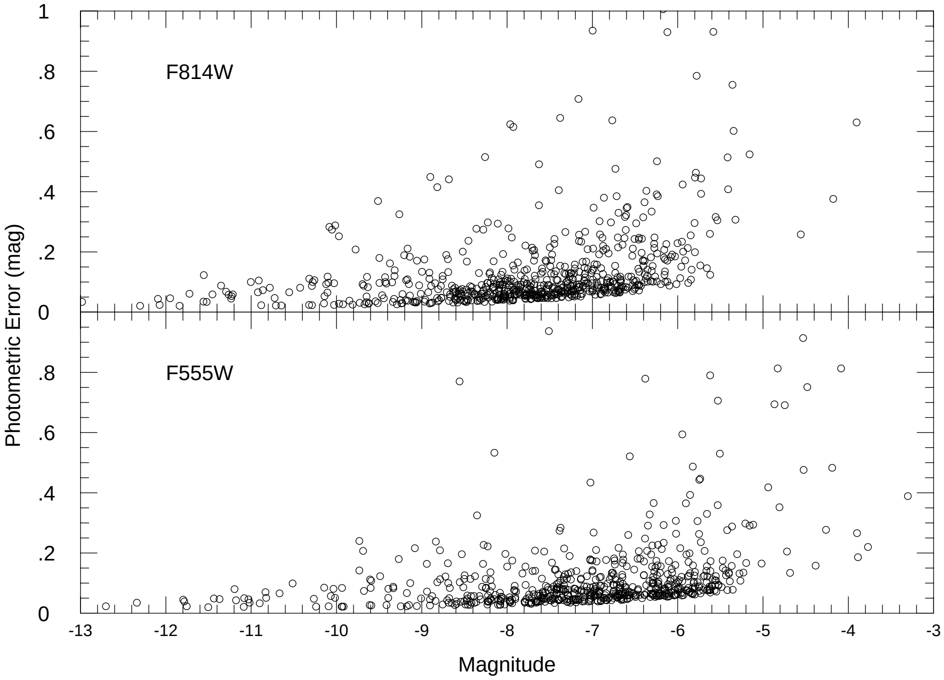

Figure 3.2: Errors as a function of magnitude for the F555W and F814W filters.

fraction of stars recovered in each magnitude bin was determined, and the results are listed in Table 3.1. We have adopted the completeness limit to be the magnitude at which the 90% of the artificial stars were recovered. In all three filters used, the completeness limits are significantly fainter than the magnitude cutoff of $V_{ST} = -8.5$ we have imposed to minimize the contribution of supergiant stars to the SSC sample; therefore, no corrections for completeness need to be made to our sample.

Table 3.1: Completeness limits found in each of the three filters as described in the text.

Completeness Level	Image F555W	 F658N	 F814W
$\geq$ 0.50	24.4	23.3	24.3
$\geq$ 0.75	24.2	23.1	23.9
$\geq$ 0.90	24.0	22.9	23.3
$\geq$ 0.95	23.0	22.8	23.0

A multicolor image of He 2-10, created with the IRAF task RGBSUN, is shown in Figure 3.1. The F555W, F658N, and F814W filters are represented by blue, red, and green respectively. A blue-green color in the image should be interpreted as continuum and red should be interpreted as Hα. An W(Hα) map (Figure 3.3) of He 2-10 was created by interpolating between the F555W and F814W filters to estimate the contribution from the stellar continuum to the flux in the Hα filter. These images will be discussed in §3.3.1.

3.3 Interpretation of Optical Images

3.3.1 Optical Morphology

The high spatial resolution of the HST allows for the examination of the detailed morphology of He 2-10. One of the most striking features is the appearance of (blue) continuum light (and some starburst knots) outside of the nucleus (region A). This luminous material has a spatial morphology reminiscent of tidal tails in merging galaxies, where region B would com-

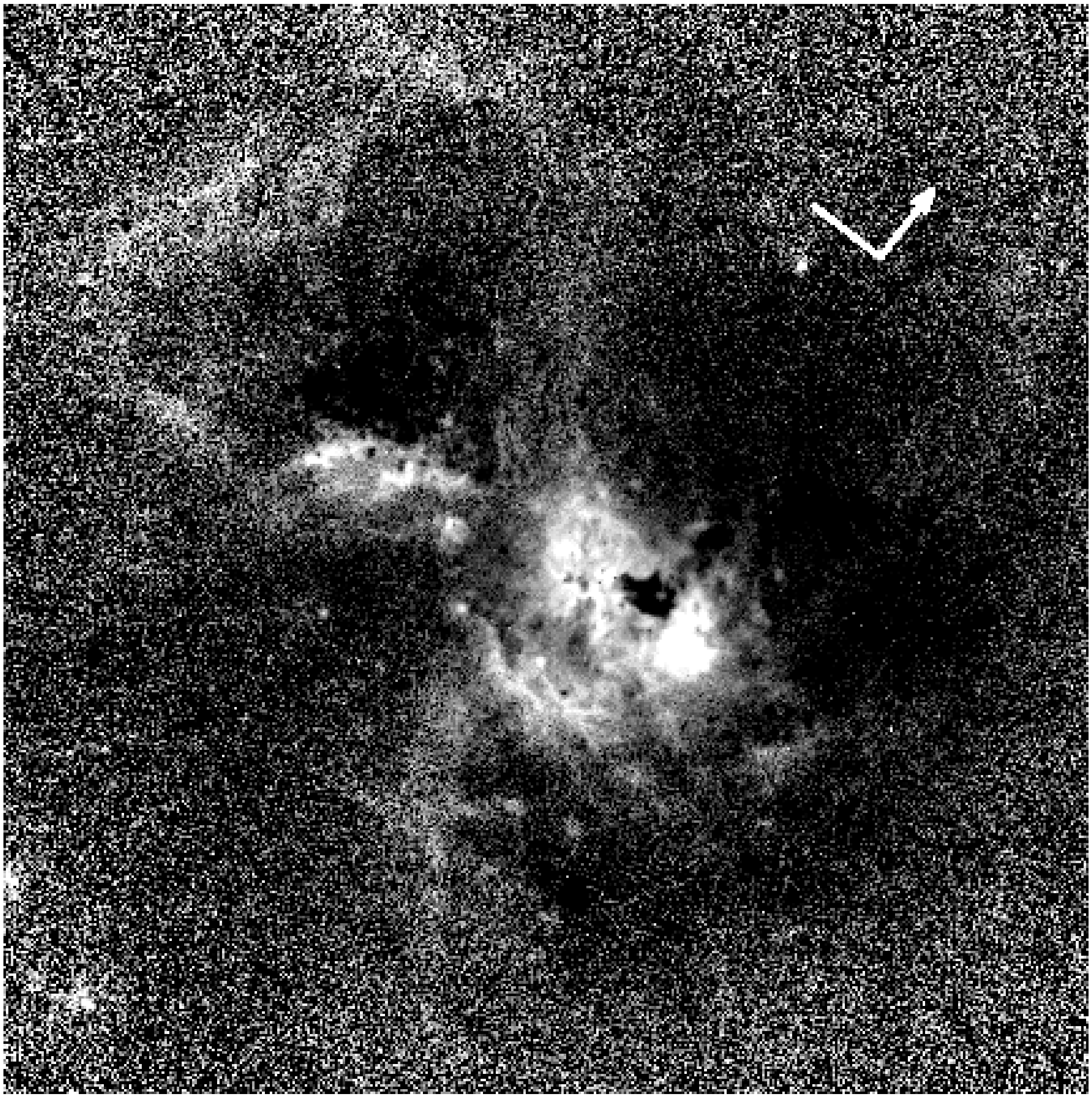

Figure 3.3: A map of the W(Hα) in He 2-10, where the brighter colors correspond to larger equivalent widths. North and east are indicated on the image, with north having the arrowhead. This image is shown with the same scale and orientation as Figure 3.1 — the length of the compass arms is approximately 100 pc.

prise one “tail” (which Johansson 1987, proposed was the interacting dwarf galaxy companion), and a smaller “tail” stretching to the north-west. The multicolor image, Figure 3.1, also reveals several features which appear to be dust lanes, including an extensive lane between regions A and B and another WNW of region A. The former is located near the position of the densest region of the molecular cloud detected at radio wavelengths by Kobulnicky et al. (1995). The interpretation of these features as dust lanes is further strengthened by moderate spatial resolution ground-based infrared images, which reveal large $J - K$ colors in these regions (Vacca 2000, private communication). The HST data suggests that the apparent galaxy morphology (e.g., the separation between the two galaxy components and the “tidal tail” morphology) is primarily a result of a dust lane blocking the light from part of the galaxy behind it, a possibility which calls into question the interpretation of region B as a separate dwarf galaxy. While there is no compelling evidence for an interacting second stellar system within He 2-10, the trigger for the starburst activity in this object could be the elongated molecular cloud found by Kobulnicky et al. (1995). This cloud is $30''$ in length, is aligned south-east, and appears to be falling into the center of the galaxy. Admittedly, this material is within the volume of the dwarf elliptical, not a usual location for tidal material, but its geometry is suggestive.

The dust lanes might be hiding other star forming regions. Indirect evidence for large and highly variable amounts of local dust obscuration with A_V of up to about 17 magnitudes has been found by Kawara et al. (1989) (see also Phillips et al. 1984; Beck et al. 1997). In addition, Kobulnicky & Johnson (1999) have detected five thermal radio sources that are highly obscured and not present in optical images but which have luminosities similar to those of the known SSCs, which will be discussed in Chapter 4. Nevertheless, since both starburst regions are visible in the optical and UV (Conti & Vacca 1994) the extinction cannot be uniformly high in those directions, although dust might hide activity on the far side of the galaxy center.

The Hα emission is distributed diffusely throughout the galaxy. The morphology in the W(Hα) (Figure 3.3) image is strikingly different from that seen in the F555W image in Figure 3.4. Filaments extending from the south and to the east of region A can be seen in the

W(Hα) image, but are not apparent in the broadband images. Ground-based imaging of Méndez et al. (1999) shows that these filaments trace parts of a kiloparsec-scale, bipolar superbubble centered on region A.

Figure 3.5 shows the F555W and W(Hα) images zoomed in to better illustrate the detail in the nuclear region of He 2-10. The region of large W(Hα) values is substantially more extended than the visible SSCs; values of W(Hα) typically greater than 100 are found throughout region A. There is also a "hole" in the Hα emission, reflected in the W(Hα) map, co-spatial with (and also directly north of) several prominent SSCs (which are roughly in a line oriented east-west), and the suggestion of a "breakout" from this region with a finger of Hα emission extending to the north-west. It is also interesting to note that the region of highest W(Hα) is located to the west of the main starforming region A and is not associated with any SSCs seen in the optical images. This region of large W(Hα), and its location offset from the nucleus of He 2-10, has been noted by Hutsemekers & Surdej (1984) and Sugai & Taniguchi (1992).

3.3.2 The Burst Luminosity

The percentage of the total luminosity due to the current starburst episode can be determined by summing the total flux in the SSCs in regions A and B and dividing by the total flux of the underlying galaxy, measured within a 3σ contour level corresponding to a surface brightness of 21.4 mag arcsec^{-2}. While using the 3σ contour level is dependent on the signal-to-noise of the observations (as discussed in Chapter 2), it appears to contain the entire optical galaxy, and we adopt it as adequate for this purpose. The SSCs brighter than V_{ST} = -8.5 account for $\approx$ 11% of the total flux, which is slightly higher than values found in other starburst systems (e.g., NGC 1741, Chapter 2). Meurer et al. (1995) found that on average, $\approx$ 20% of the UV light in starburst galaxies comes from clusters. Since this percentage should drop off at longer wavelengths, a 11% contribution from clusters in V_{ST} is within the expected range of values.

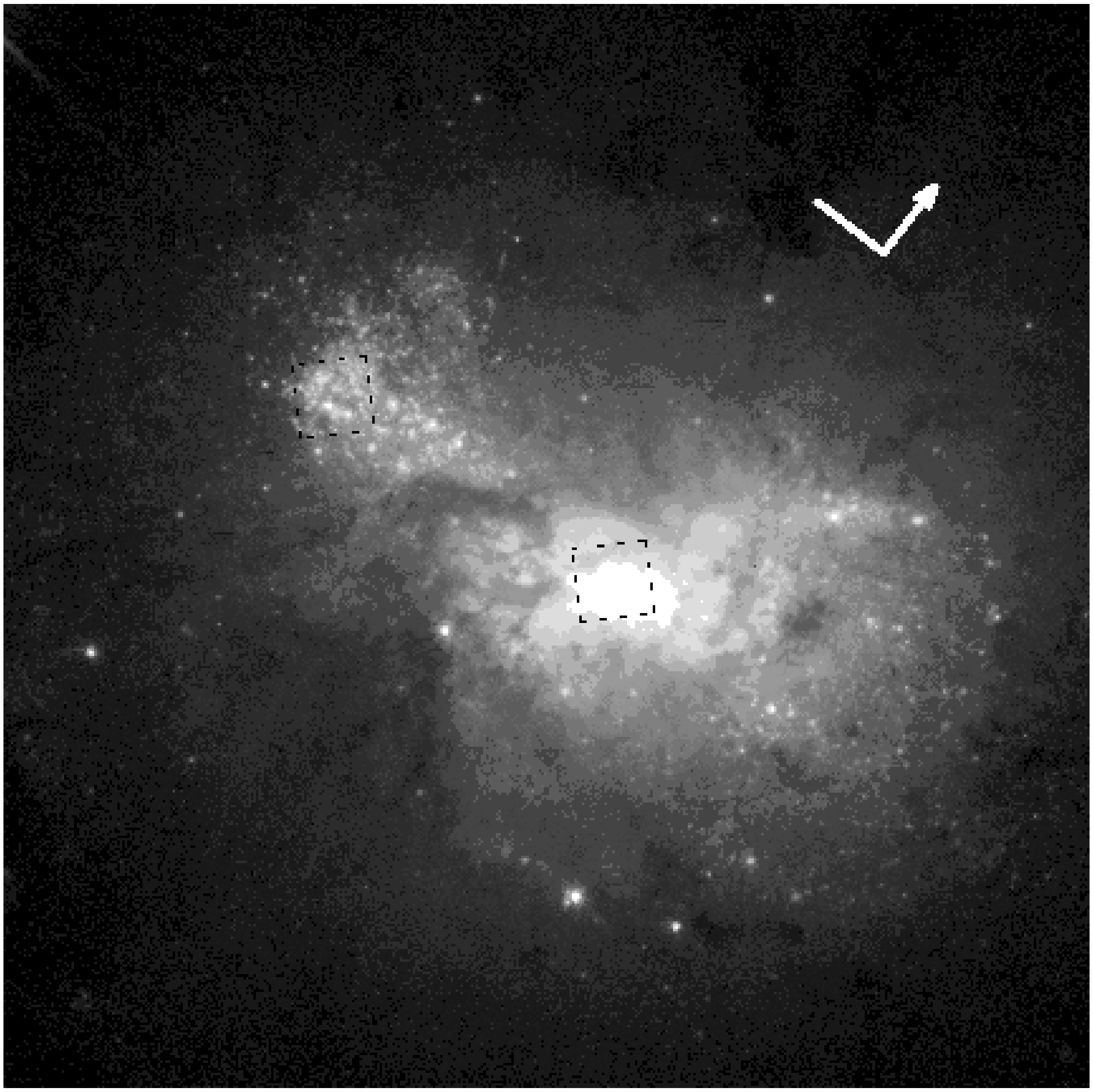

Figure 3.4: A F555W image of He 2-10 with the GHRS apertures used in Johnson et al. (2000) ($1.74'' \times 1.74''$ or approximately 75 pc × 75 pc) overlaid on starburst regions A (west) and B (east). North and east are indicated on the image, with north having the arrowhead. Note that this image has the same scale and orientation as Figure 3.1 and Figure 3.3.

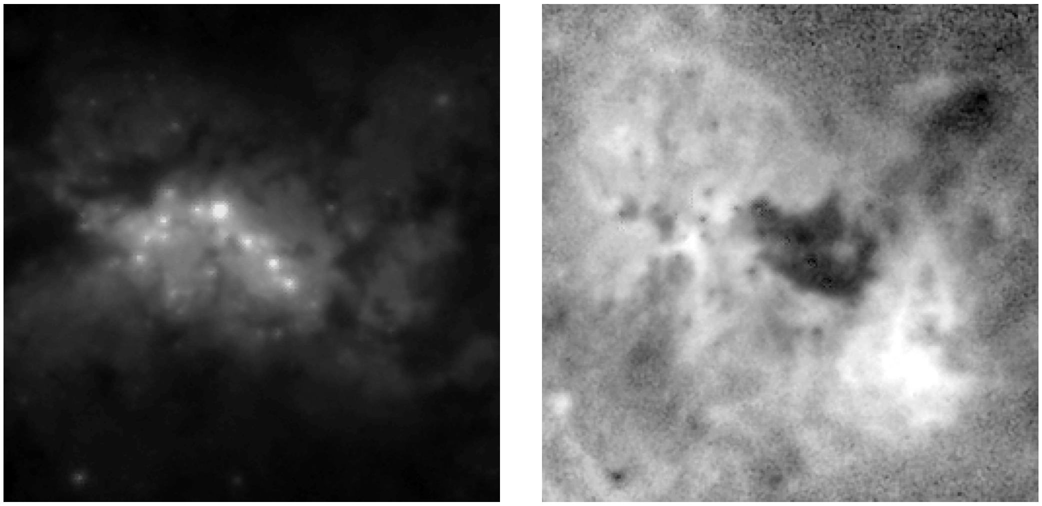

Figure 3.5: The nuclear region of He 2-10 shown in F555W (left) and W(Hα) (right) where brighter colors correspond to SSCs and stellar background in (a) and larger equivalent widths in (b). These images are registered to each other and shown in the same orientation as Figures 3.3 and 3.4, and are approximately 250 pc on a side.

3.3.3 Properties of the Super Star Clusters Compared to Models

3.3.3.1 Broad band magnitudes and colors

In order to obtain information about the SSCs from their magnitudes and colors, I again adopt the models of Leitherer & Heckman (1995) and Leitherer et al. (1999) (see also Johnson et al., 1999, for a description of the nebular line contribution to the models). In Figure 3.6 I plot the V_{ST} magnitude versus the V_{ST} - I_{ST} color of the SSCs brighter than $M_V = -8.5$ in He 2-10. The data have been corrected for Galactic foreground extinction but not for instrinsic extinction within the He 2-10 itself; the vector plotted in Figure 3.6 shows the direction the data points would move on this plot if they were corrected (de-reddened) for an intrinsic reddening of 1 magnitude in V_{ST} . I have also included in this figure the predictions from models which include *only* stellar light (dashed line) and both stellar light and *nebular* line emission (solid line). Only a few SSCs appear to have sufficiently strong Balmer line emission as to require the latter models. These very young objects lie to the left of the dashed lines (models without Balmer emission) in Figure 3.6. This is to be contrasted with NGC 1741 F, in which all of the SSCs have very strong Hα and lie well to the left in a similar plot (Chapter 2).

From 1 to 10 Myr, the models evolve at nearly constant M_V but with increasingly redder $V - I$. From 10 to 100 Myr, M_V drops precipitously but at nearly constant color. More massive SSCs are more luminous and have correspondingly brighter M_V. Thus, without additional information, there is no way to tell whether the SSCs with M_V between -11 and -12 and $V - I$ colors near 0.5 (for example) are relatively old (near 100 Myr) with masses of 10^5 M$_\odot$ or relatively young (near 10 Myr) with masses of 10^4 M$_\odot$. There is an additional ambiguity due to reddening — the SSCs could be younger and more massive than would be assumed based on their colors and magnitudes. However, as we show in the next section, nearly half of the SSCs in Figure 3.6 have Hα emission and cannot be older than 10 Myr.

The V_{ST} magnitudes of these SSCs then imply that the SSCs have masses from 10^3 M$_\odot$ up to 10^5 M$_\odot$ (for a Salpeter IMF between 1 and 100 M$_\odot$), although, depending on the amount

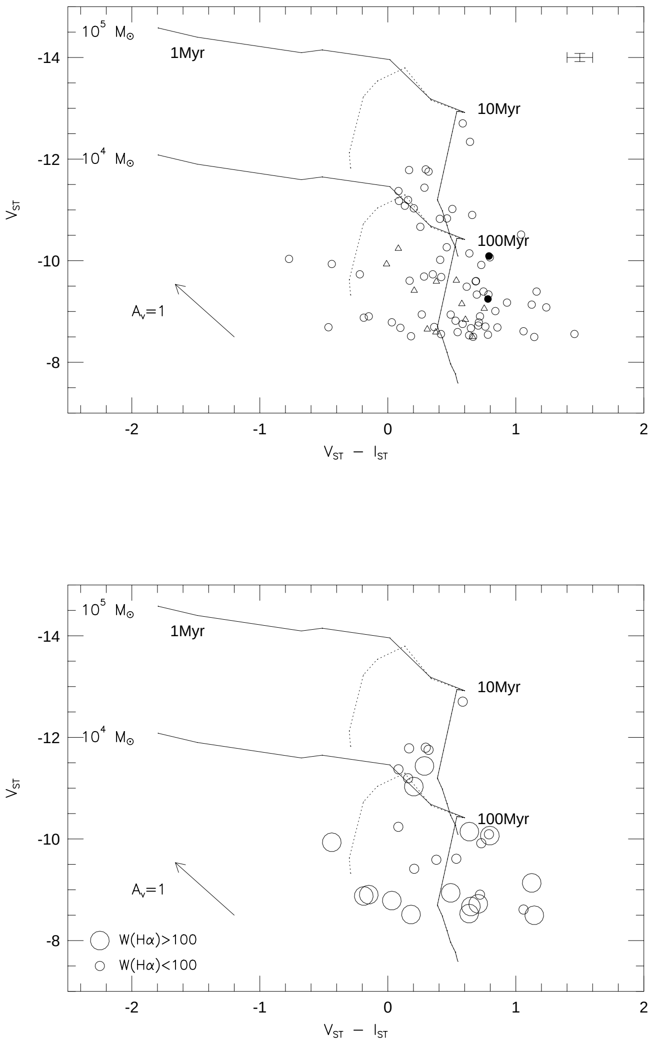

Figure 3.6: The V_{ST} magnitude and V_{ST} - I_{ST} colors of the SSCs brighter than $V_{ST} = -8.5$ in He 2-10 along with the models including *only* stellar light (dashed line) or including both stellar light and *nebular* line emission in blue (solid line). (a) SSCs found in region A are shown as open circles, region B as triangles, and the extension to the north-west of region A as filled circles. The ages are labeled along the 10^5 M$_\odot$ only, but the lower mass track behaves similarly. No correction for internal reddening in He 2-10 has been applied, but a de-reddening vector of A$_V$ = 1 is shown for reference. Typical uncertainties are indicated in the upper right corner. (b) The SSCs detected in the F658N filter are shown with W(Hα) $>$ 100 as large circles and W(Hα) as small circles.

of internal extinction, the apparent mass range could shift upward somewhat. The SSCs in region A (open circles) exhibit a larger range in color than those in region B (triangles). This could be due to SSCs in region A having a larger range in ages or a greater variation in extinction. The latter effect seems certain to play a role, given the appearance of dust features near the center of the galaxy. The locations of two SSCs found in the north-west extension of region A (filled circles) are also plotted in Figure 3.6; these SSCs appear to either be older or more heavily reddened than typical SSCs found in regions A or B.

3.3.3.2 Hα measures

Not all of the SSCs show Hα emission; the majority are bluish in Figure 3.1, which indicates that their SEDs are dominated by continuum emission. In the F658N filter we detect only about 40% (33/76) of the sources detected in F555W or F814W above our imposed magnitude cutoff of $M_V = -8.5$. Note that the magnitude limit is several magnitudes brighter than the F658N filter completeness limit. The Hα equivalent width was determined by interpolating between the broad-band filters to determine the value of the “continuum” flux in the F658N filter. The W(Hα) values are plotted along with model values for ages between 0.01 and 100Myr in Figure 3.7. Because we are using broad-band filters to establish the continuum level, systematic uncertainties due to the presence of flux from an older population (e.g., red supergiants) in the F814W filter and the Hβ and [O III] lines in the F555W filter will both tend to cause an *over-estimation* of the continuum value in the F658N filter, and therefore an *underestimation* of the W(Hα). For our values, we could be underestimating the W(Hα) by as much as ≈ 50%.

As Figure 3.7 illustrates, nearly all of the SSCs that were detected in the F658N filter are very young (less than 10 Myr) objects. In Figure 3.8 we show the locations of the SSCs detected in the F658N filter, which are almost exclusively in the starburst regions A and B and the feature extending northwest from region A. All of the SSCs with W(Hα) > 100 are located in the starburst region A, which we interpret as being the current center of the starburst activity in He 2-10, and therefore younger than region B.

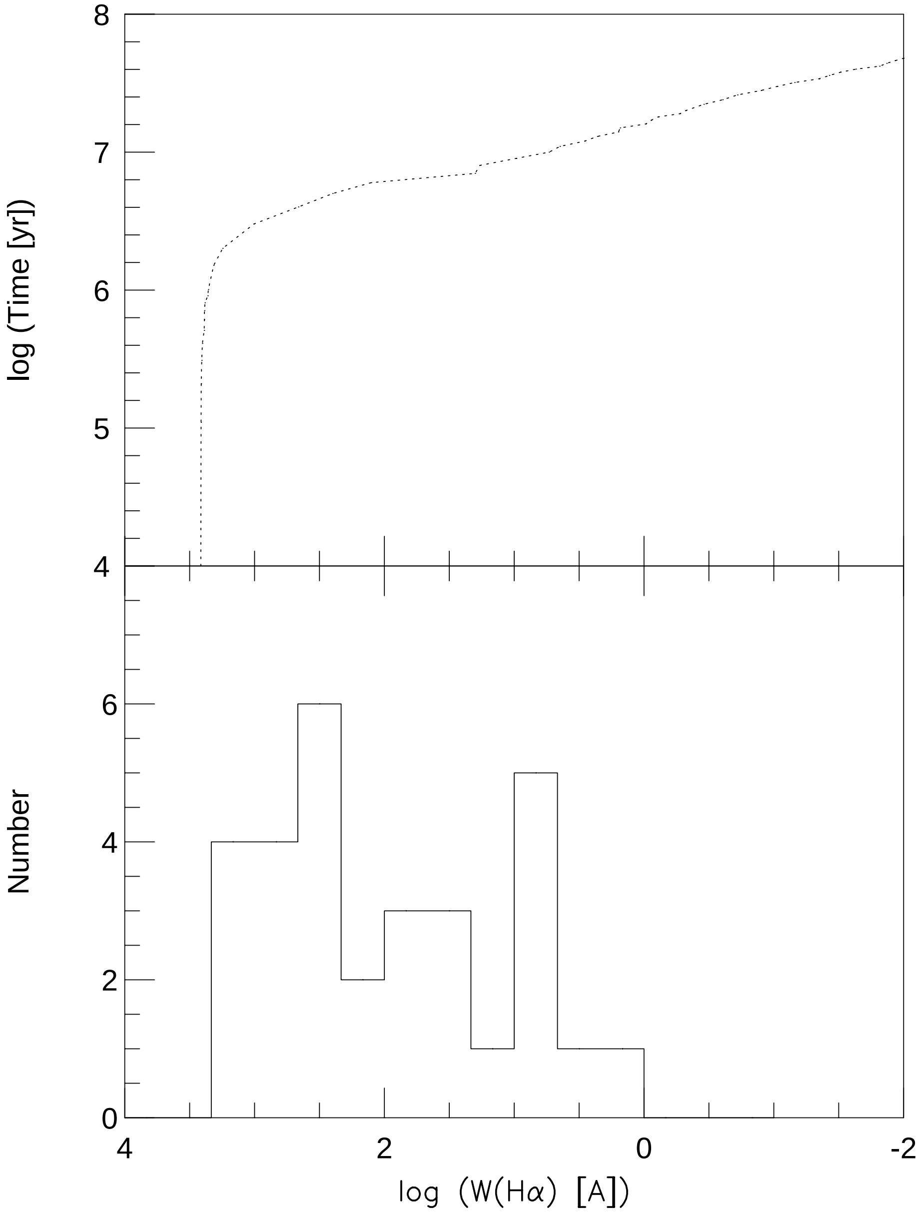

Figure 3.7: A histogram of the W(Hα) values for SSCs in He 2-10 is shown (bottom) along with model predictions (top) from Leitherer et al. (1999) for W(Hα) vs. age.

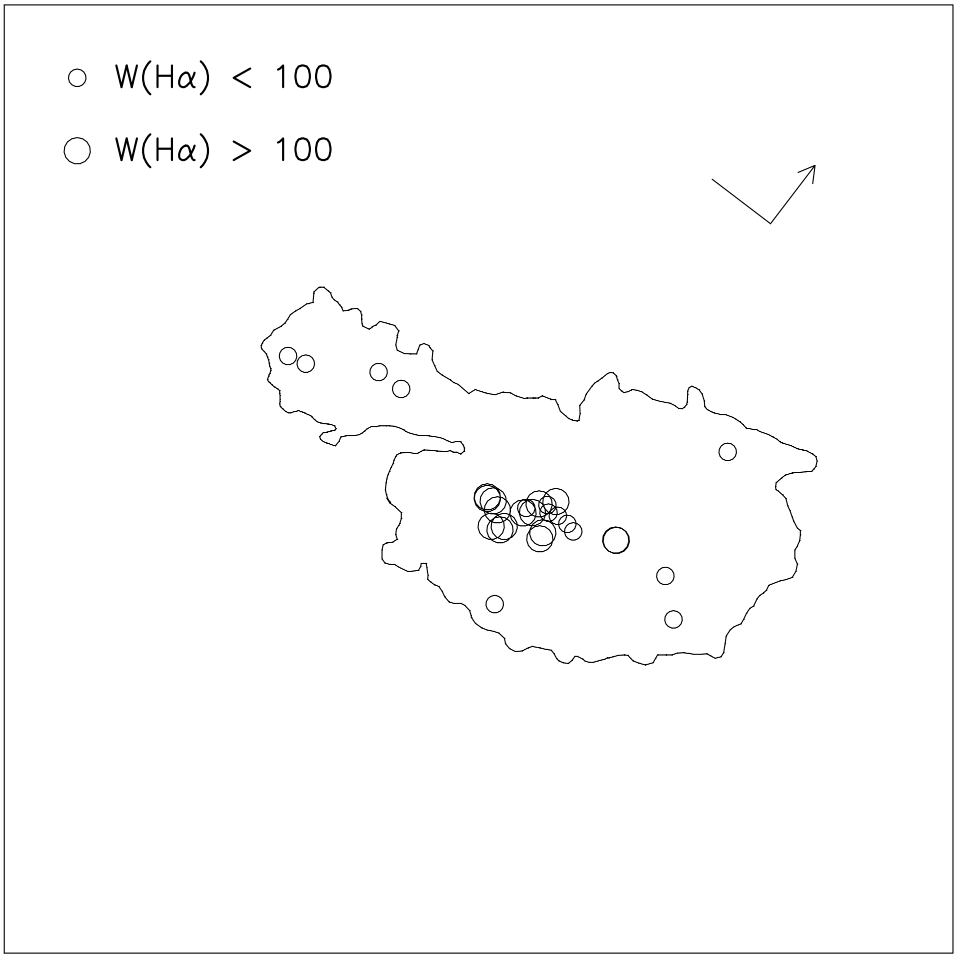

Figure 3.8: The locations of the SSCs detected in the F658N filter are shown. The plot has the same dimensions and orientation as Figures 3.1, 3.3 and 3.4. An optical contour is also shown for reference. Because of their larger W(Hα), the central SSCs in region A must be younger than those in region B.

In Figure 3.6b we show the locations of the SSCs detected in the F658N filter on the same color magnitude diagram used in Figure 3.6a. Since all of the SSCs with W(Hα) $>$ 100 must be young (less than 10^7 years), all of the points which lie to the right of the models must be heavily reddened — in some cases by at least 1.5 magnitudes. This provides additional evidence for areas of thick and patchy extinction in He 2-10. In comparing this plot with Figure 3.6, it is curious that two of the SSCs which lie to the left of the model incorporating only stellar light (and which therefore should have nebular emission) are not detected in the F658N image. We have examined each of these SSCs individually, and found that in the case of the SSC with the bluest color, it *does* have associated Hα emission, but this emission is diffuse in nature and was not identified as a point source. In the second case, the SSC has no associated Hα emission, but the uncertainties of its magnitudes are just large enough to put it in agreement with the model incorporating only stellar light.

The 43 SSCs that were not identified in the F658N filter could be undetectable for several reasons. Some SSCs could be too old to produce a significant amount of Hα flux, which is not inconsistent with some of their V_{ST} - I_{ST} colors. Several SSCs have associated Hα emission which is diffuse in nature and therefore these objects were not identified as point sources on the F658N image. These objects were left out of the sample in order to maintain consistent identification and photometry procedures in all three filters; it should be kept in mind, however, that *more* than the 33 sources identified in the F658N filter have associated Hα emission. It is also possible, given the large amount of local dust, that some ionizing photons are absorbed and do not produce Hα. Finally, given the diffuse distribution of Hα throughout the galaxy, it is plausible that some of the ionizing photons are leaking from the SSCs into the immediate vicinity (Figure 3.5). There may also be leakage of thermally produced Lyman continuum photons from the starburst regions (Figure 3.3). From the Hα detection statistics ($> 33/76$) I conclude that more than 40% of the SSCs must be young, with ages no more than 10 Myr according to Figure 3.7.

3.3.4 Luminosity Functions of the Super Star Clusters

The luminosity function (LF) of the SSCs and the fainter sources in He 2-10 was determined by counting the number of objects within half-magnitude intervals; the LF was then fit by the method of least squares with the data weighted by Poisson statistics. In Figure 3.9 the V_{ST} LF of the SSCs for He 2-10 is shown, which is well fit by a power law of the form $\phi(L) \propto L^{-1.7}$ for magnitudes brighter than $M_V = -8.5$. As I will discuss in §3.4 (and was discussed in Chapter 2), this power law index is typical of other systems observed. For magnitudes in the range $-8.5 < M_V < -6.8$ the data are fit by a slightly steeper power law of the form $\phi(L) \propto L^{-1.8}$. A steepening of the luminosity function at fainter magnitudes is expected because of the increasing contribution of red and blue supergiants which contaminate the samples and eventually dominate the statistics. This has been seen previously by Whitmore et al. (1999) in the “Antennae” galaxies where they found the LF in the range $-9 < M_V < -6$ to be $\phi(L) \propto L^{-2.9}$. I speculate that the difference between the two exponents (this value and that of Whitmore et al.) is primarily due to our completeness limit being almost an entire magnitude brighter than that of Whitmore et al. (1999); not as many individual stars are contaminating in this sample.

The V_{ST} - I_{ST} color distribution of the SSCs in He 2-10 is shown in Figure 3.10. The mean value of the distribution was found to be 0.48 with a dispersion of 0.39. This is very blue compared to SSCs in other starbursts, a point to which I will return in §3.4.2.

3.3.5 Radii

The radii of the sources were estimated the same manner described in Chapter 2 using $\Delta_{0.5-3}$. The radii measurements determined for the sources in the F555W filter are shown in Figure 3.11. Most (90%) of the sources have radii values smaller than 3 pc, consistent with most of them being unresolved. Within uncertainty, the remaining sources are also unresolved. Therefore, it is reasonable to adopt 3 pc as an upper limit to the radii of the SSCs in He 2-10.

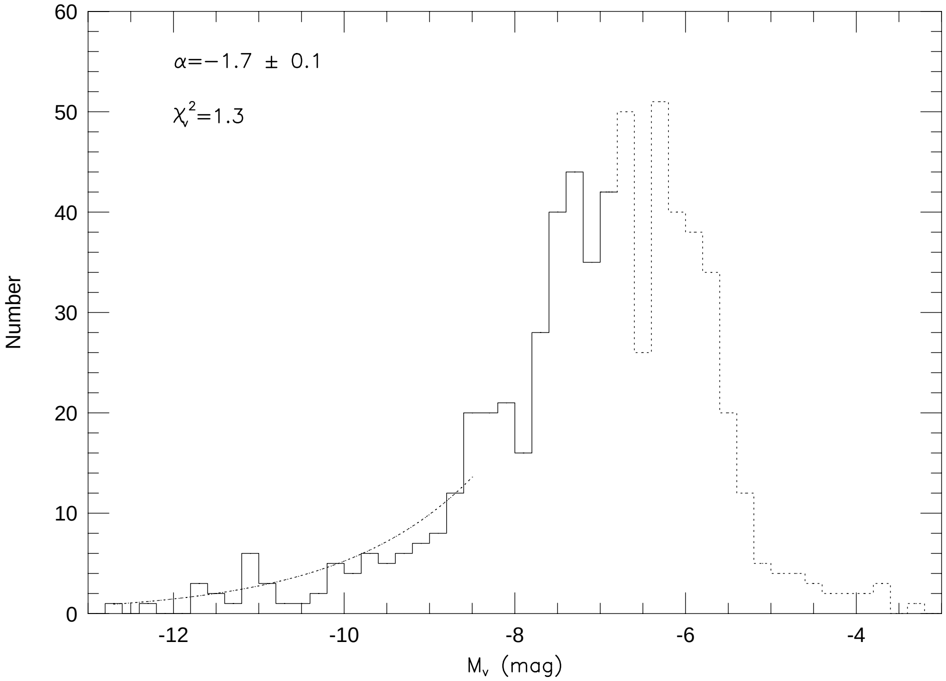

Figure 3.9: The V_{ST} luminosity function of the SSCs in He 2-10 shown with a solid line brightward of the completeness limit. The power law fit brighter than $V_{ST} = -8.5$ is shown with a dashed line. No correction for internal reddening in He 2-10 has been applied.

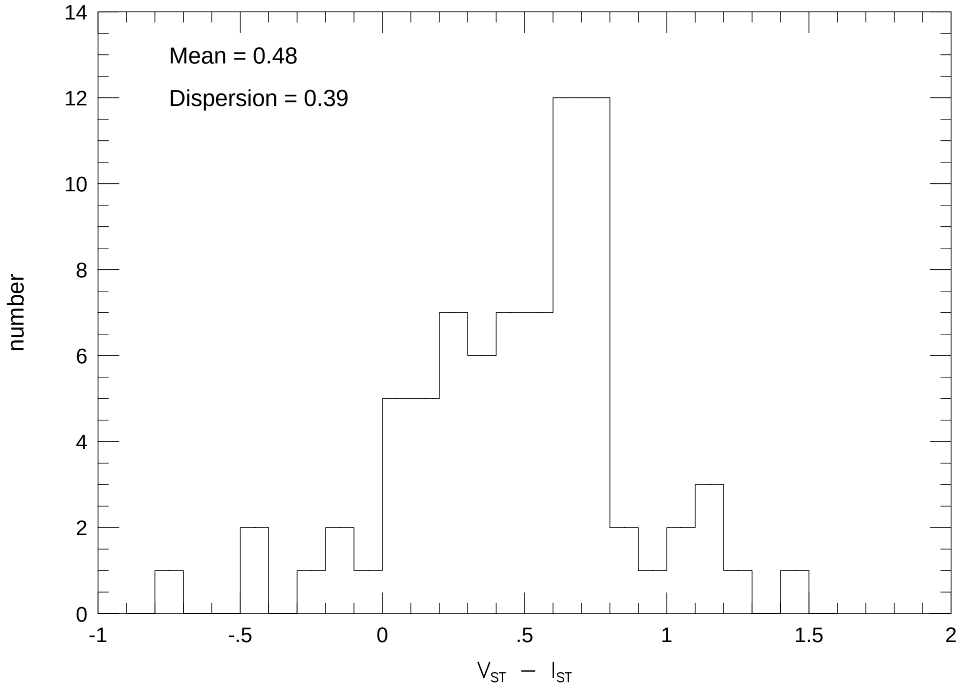

Figure 3.10: The V_{ST} - I_{ST} plot for the SSCs in He 2-10. No correction for internal reddening in He 2-10 has been applied.

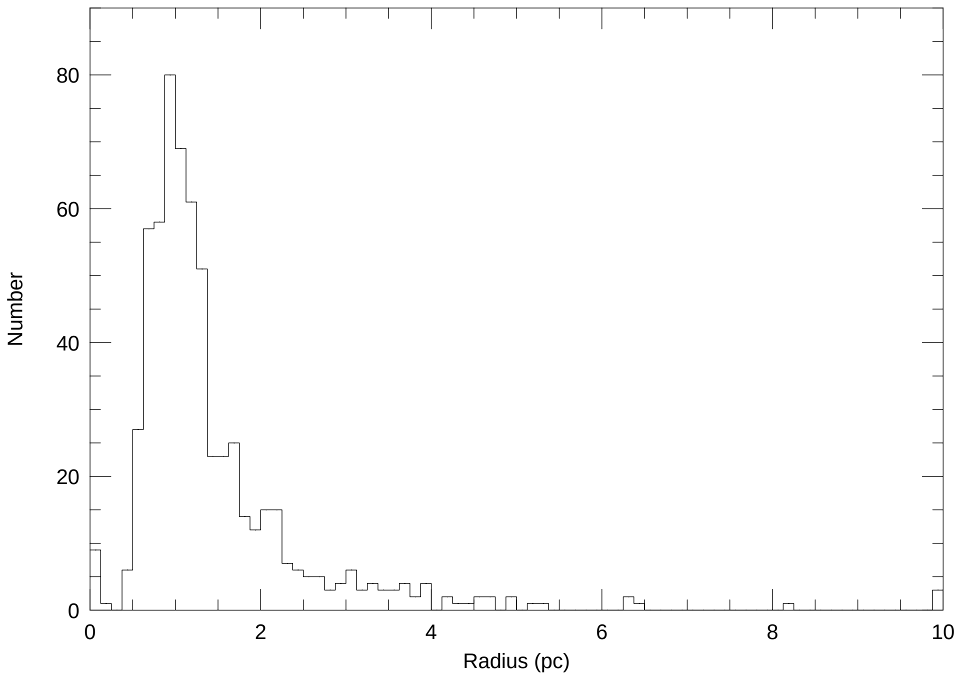

Figure 3.11: A histogram of the radii measured using the $\Delta_{0.5-3}$ magnitudes for the sources in He 2-10.

3.4 Discussion

3.4.1 On the Universality of SSC Luminosity Functions

As discussed in Chapter 1, a universal mechanism for cluster formation has been proposed by Elmegreen & Efremov (1997) who argue that the initial mass spectrum for star clusters is naturally a power law with a slope of ~ -2. This slope is the result of the hierarchical distribution of structure in turbulent gas, and the primary differences between various types of clusters (i.e., open clusters and globular clusters) are due to pressure differences in the cluster birth environments.

The observed slope of the luminosity function for SSCs is dependent on the initial mass spectrum of clusters, the ages of the SSCs, and the stellar initial mass function (IMF). In the case of W-R galaxies, such as He 2-10, the age of the burst can be constrained *a priori* to $\sim$ 3 to 6 Myr using evolutionary synthesis models [2] . Therefore, if we take the stellar IMF to be universal, as recent work has suggested (see Massey et al. 1995; Massey & Hunter 1998), and the luminosity functions of the SSCs W-R galaxies are compared, any similarities or differences provide direct information about the initial mass spectrum of clusters. In Chapter 2 another W-R galaxy was studied, NGC 1741, and found a power law slope of -1.9 ± 0.1, in close agreement with the value for He 2-10 of -1.8 ± 0.1. Observations of other starburst galaxies yield similar exponents for the LF of SSCs ($\alpha \approx 1.7 - 2.1$; Vacca 1997; Schweizer et al. 1996; Whitmore & Schweizer 1995; Meurer et al. 1995, see Table 1.1). Obviously more examples need to be obtained, but this technique may be providing us with evidence of a constant initial mass spectrum of SSCs.

---

[2] It should be noted that even in the case that star formation is *not* relatively instantaneous (as in a burst), if clusters are formed with the same power law distribution at all times, the time integrated distribution will evolve with the same power law distribution as that of an instantaneous burst.

3.4.2 Comparison to Other Starburst Systems

The mean $V - I$ color of SSCs in interacting galaxies is predicted to shift from blue to red with time (see Schweizer et al. 1996). Although He 2-10 is not an interacting system in the classical sense, it does show evidence of interaction with a 10^8 $M_\odot$ molecular cloud (a disturbed morphology and possible tidal tails), and it is appropriate to compare its star formation history with other merger systems. The mean color of $V - I = 0.48$ is among the bluest values found for SSCs in interacting systems studied to date. This can be interpreted to mean that the SSCs in He 2-10 are among the youngest identified. As discussed in Chapter 2, NGC 1741 is another example of extremely young system of SSCs with a mean color of $V - I = 0.41$, before including any correction for internal reddening. In the sample studied by Schweizer et al. (1996), the galaxy system with the bluest color distribution is NGC 4038/39 with a mean $V - I = 0.34$ *after* a reddening correction of -0.26 magnitudes. It is important to reiterate here that our magnitudes of the SSCs in He 2-10 have *not* been corrected for internal reddening. Furthermore, it is important to note that many of the knots seen in the optical WFPC2 images are very bright in the FOC 2200 Å image obtained by Conti & Vacca (1994). The strong UV flux from these knots is an additional indicator of their young ages. Hence, He 2-10 provides an example of some of the most recently formed SSCs ever observed, a point which I will expand upon in Chapter 4.

How does the star formation rate in He 2-10 compare to other starburst systems? As in chapter 2, the blue luminosity can be used to estimate the star formation rate. Adopting a B magnitude of -19.1 from Conti (1991), the Starburst99 models of Leitherer et al. (1999) imply a total star formation rate of 3.8 $M_\odot$ yr^{-1} if the star formation has been occurring over the last 10 Myr (for a Salpeter IMF between 1 and 100 $M_\odot$). Adopting a projected surface area of He 2-10 to be ≈ 2 kpc^2, the star formation rate per unit surface area is 1.3 $M_\odot$ yr^{-1} kpc^{-2}. This star formation rate is among the highest observed for UV-bright starburst galaxies (Meurer et al. 1995), and nearly twice as high as the star formation rate observed for the starburst in NGC 1741 in chapter 1. Given that star formation efficiencies necessary to form bound clusters are on the order of ≈ 0.2 (e.g., Verschueren 1990), an average star formation rate of 3.8 $M_\odot$ yr^{-1} would consume the molecular cloud mass of $\approx 10^8$ $M_\odot$ that appears to be interacting with and fueling the starburst (Kobulnicky et al. 1995) in $\approx 5 \times 10^6$ years. Therefore the molecular cloud is not likely to fuel star formation at such a high rate over a very long time scale.

3.4.3 Implications of Large-Scale Outflow

The mechanical luminosity input from supernova-driven winds, and the resulting mass outflows, can have a significant affect on the evolution of dwarf galaxies and the metal enrichment and ionization of the IGM. In Johnson et al. (2000) we concluded that there is a large-scale outflow of the interstellar medium in He 2-10 with a bulk motion of minimally 360 km s^{-1} and a mass of at least 10^6 $M_\odot$ (based on the spectral analysis done by C. Leitherer and not presented here). This outflow velocity is somewhat larger than the value of 250 km s^{-1} that Méndez et al. (1999) derive from ground-based spectroscopy of the bipolar superbubble centered on region A. This discrepancy is likely due to geometrical effects, as we have spectra of different parts of the galaxy, and therefore different inclination angles of the outflow. While outflows have been observed in a number of galaxies (e.g., Pettini et al. 2000; Gonzalez Delgado et al. 1998; Kunth et al. 1998; Marlowe et al. 1995; Heckman et al. 1995; Meurer et al. 1992), they are typically < 200 km s^{-1}. The outflow we measure in He 2-10 has the one of the highest velocities ever observed in cold gas via metal absorption lines (Lyα and Lyβ absorption components indicate even higher velocities in a few galaxies, however Lyα is a complex line, affected by scattering, and the picture is not clear, Gonzalez Delgado et al. 1998; Kunth et al. 1998).

In order to determine whether this outflow has a velocity high enough to result in mass loss from He 2-10, an estimate of the escape velocity (v_e) needs to be obtained. The most simplistic approach is to assume the escape is from a point source mass, implying

$$v_e > \left(\frac{2GM}{r}\right)^{1/2} \text{ km s}^{-1}, \tag{3.1}$$

where M is the dynamical mass and r is the current radius of the outflowing shell. Here I assume the radius of the outflow is approximately the projected radius of the outflow of ≈ 1 kpc found by Méndez et al. (1999). Baas et al. (1994) estimated the dynamical mass of He 2-10 to be $6.7 \pm 3.4 \times 10^9$ M$_\odot$, and Kobulnicky et al. (1995) found the mass of He 2-10 to be $> 2.7 \times 10^9$ M$_\odot$ (uncertain by a factor of $1/(\sin i)^2$, where i is the inclination angle of the bulk rotation). This issue is somewhat complicated by the complex rotation curve, but here if I adopt the dynamical mass of $6.7 \pm 3.4 \times 10^9$ M$_\odot$, the escape velocity for He 2-10 is $\approx 240 \pm 30$ km s^{-1}.

I can also estimate the the v_e using the more sophisticated relation derived for dwarf galaxies by Ferrara & Tolstoy (2000);

$$v_e \approx 20 M_{D,7} \times h^{1/3}\ \mathrm{km\ s^{-1}}, \tag{3.2}$$

where $M_{D,7}$ is the dynamical mass in units of 10^7 M$_\odot$ and $H_0 = 100h$ km s^{-1}Mpc^{-1}. Again I adopt the dynamical mass of $(6.7 \pm 3.4) \times 10^9$ M$_\odot$ and $h = 0.75 \pm 0.2$, implying the escape velocity for He 2-10 is $\approx 160 \pm 30$ km s^{-1}. This value is in agreement with the the low end of the range of escape velocities presented by Méndez et al. of 110 to 425 km s^{-1}. Adopting the range $v_e = 160 \pm 30$ km s^{-1} to $v_e = 240 \pm 30$ km s^{-1}, it is clear that the measured outflow velocity of $>$ 360 km s^{-1} is more than adequate to escape the gravitational potential well of He 2-10.

Once the outflow has escaped He 2-10, it will be able to enrich the local IGM. Ferrara & Tolstoy (2000) find the oxygen yield (the mass fraction of the stellar mass to be converted into oxygen and expelled) to be 0.0871 for a Salpeter IMF, with lower and upper mass cutoffs of 1 M$_\odot$ and 120 M$_\odot$, although this value may be an order of magnitude lower for low metallicity stars in the $z > 3$ universe (Woosley & Weaver 1995). (It is also important to bear in mind that since stellar mass loss is primarily radiatively driven through metal lines, a low metallicity may also inhibit the outflow to begin with.) From the UV spectrum, Johnson et al. (2000) estimated the total stellar mass locked up in the current starburst episode in regions A and B to be ≈ 2 to 3×10^6 M$_\odot$ (based on the spectral analysis done by C. Leitherer and not presented here);

this value is a *lower* limit as it does not include the contributions from the galaxy outside these regions. We can roughly estimate this additional mass from the V_{ST} magnitudes of SSCs not included in the GHRS apertures as $\approx 10^6$ M$_\odot$. This total mass implies an expelled oxygen mass of $\approx (3-4) \times 10^5$ M$_\odot$. The models of Mac Low & Ferrara (1999) for metal ejection efficiency for starburst-driven mass loss from dwarf galaxies indicate that virtually all of the metals ejected by massive stars in He 2-10 will be lost from the galaxy. This mass in metals would be enough to raise primordial metal abundances in 1 Mpc^3 to approximately 10^{-3} to 10^{-2} solar.

If the outflow continues to expand at > 360 km s^{-1}, it would take ≈ 2 Gyr to travel 1 Mpc. However, one should note that the outflow is likely to be stopped before a radius of 1 Mpc due to pressure from the IGM. Following Venkatesan et al. (2001), the radius at which the outflow will stall is given by

$$r_{st} \approx (0.5\ \mathrm{Mpc}) \times \left[\left(\frac{\dot{M}}{M_\odot/\mathrm{yr}} \right) \left(\frac{v}{10^3 \mathrm{km/s}} \right) \left(\frac{10^4\ \mathrm{K}}{\mathrm{T_{IGM}}} \right) \left(\frac{10}{1+z} \right)^3 \right]^{1/2}, \tag{3.3}$$

where $\dot{M}$ and v are the mass outflow rate and velocity, respectively. For a mass outflow rate of ≈ 1 M$_\odot$ yr^{-1}, velocity of $\gtrsim 400$ km s^{-1}, redshift of $z = 5$, and IGM temperature of $\sim 10^4$ K, this outflow would be stalled by a radius of ≈ 0.7 Mpc. This outflow from He 2-10 may be quite typical of starbursting dwarf galaxies; Heckman (2001) conclude that superwinds are ubiquitous in starburst galaxies with star formation rates $> 10^{-1}$ M$_\odot$ yr kpc^{-2}. Cowie et al. (1995) find that Lyα clouds have a typical metallicity of $\approx 10^{-3}$ to 10^{-2} solar, and it is possible that starbursting dwarf galaxies, like He 2-10, could be a major source of these pollutants in the early universe.

He 2-10 could also be responsible for ionizing a volume of the IGM. For our estimated starbursting mass of a few $\times 10^6$ M$_\odot$, the number of photons emitted below 912 Å is approximately 10^{52} to 10^{53} s^{-1}. Dove et al. (2000) find the fraction of Lyman continuum photons which escape from disc galaxies via "chimneys" to be $f_{esc} \approx 0.05 - 0.15$, although the lower limit of this range seems to be in better agreement with observations (Tumlinson et al. 1999;

Leitherer et al. 1995). Therefore we adopt $f_{esc} \approx 0.05$ as a lower limit. If we estimate the mean hydrogen density of the IGM to be 1.7×10^{-7} cm$^{-3}(1+z)^3$, and the recombination time to be 2 Gyr (assuming a clumping factor of 10) (Madau et al. 1999), He 2-10 could possibly ionize a sphere with radius $\approx$ 1 Mpc for $z = 1$, although this value is uncertain due to the uncertainty in the value of f_{esc}.

The outflow in He 2-10 may also have a role in regulating star formation. If the mass of 10^6 M$_\odot$ observed in the outflow was expelled over a few Myr, then the mass-loss rate is comparable to the star formation rate. Pettini et al. (2000) also found the wind mass-loss approximately equal to the star formation rate in the z $\approx$ 3 object cB58. Are stellar winds the ultimate limit to star formation in starburst galaxies? In a Schmidt-type star formation law, the star formation rate is proportional to the gas density. However, both star formation itself, and the ensuing mass outflows, will tend to decrease the gas density, thereby decreasing the star formation rate. While the extent to which outflows will affect ongoing star formation is unclear, it is plausible that they may serve as a kind of regulation mechanism in starburst galaxies.

3.4.4 A Note of Caution

It is evident in Figures 3.1 and 3.3 that the distribution of the Hα light in He 2-10 is not centered on the SSCs; instead, there is diffuse emission throughout the inner parts of the galaxy (see section 3.3.1). In fact, there is a hole in the Hα emission near the main star forming region A (Figure 3.5), and it is clear that the ambient gas has been blown away from the central SSCs. Furthermore, due to the presence of an older, underlying stellar population, the W(Hα) may be diluted. While it is tempting to use nebular line emission (such as Hα) as a diagnostic tool, the HST image of He 2-10 serves as a caution that nebular emission measures may not always be a good quantity for evaluating the precise age and stellar content of young SSCs. Many of our SSCs have broad band colors indicating ages $<$ 10Myr, yet weak or absent Hα emission; these SSCs are most likely leaking Lyman continuum photons. The starburst regions may also be porous, but here the quantitative effect is smaller (§4.3).

Chapter 4

The Discovery of "Ultradense HII Regions": The Early Stages of Massive Star Cluster Evolution

4.1 Background

In the previous two chapters, super star clusters visible in optical light have been discussed at great length. Some of these clusters are unambiguously young (where I define young to mean $<$ 10 Myr) compared to the age of a typical globular cluster in the Milky Way. However, once these clusters have emerged from their birth cocoons and are visible in optical light, they are well into their adolescence. If massive star cluster formation follows a process similar to that of individual massive star formation, then the earliest stages of clusters evolution will be hidden from optical and UV observations by large amounts of dust and molecular material from which the clusters were formed. Hence, studies of this early phase of cluster evolution require observations at longer wavelengths which are relatively immune to the effects of dust scattering and absorption by the natal material.

If young SSCs are indeed hidden at ultraviolet and optical wavelengths as the result of absorption by surrounding dust, the bulk of their bolometric luminosities should be radiated in the mid- to far-infrared regimes due to the re-processing by dust. With this in mind, it is logical to predict that the youngest SSCs should not be visible at wavelengths shortward of infrared, they should be extremely luminous in the mid- to far-infrared, and they should have radio emission consistent with very dense H II regions.

In this chapter the detection of five such embedded ultra-young clusters discovered in the radio continuum and confirmed with mid-infrared imaging is presented. The analysis of the radio data was originally in collaboration with H. Kobulnicky, and here I present my own analysis of the radio data and only highlight aspects for which H. Kobulnicky was primarily responsible.

4.2 Observations and Data Reduction

4.2.1 VLA Radio Continuum Observations

Aperture synthesis radio continuum observations were carried out by H. Kobulnicky with the NRAO Very Large Array using a variety of frequencies and array configurations from 1995 through 1996. Observations of 2 cm (15.0 GHz) and 6 cm (4.58 GHz) were obtained with the B and A arrays, respectively, allowing for relatively well matched synthesized beams at the two wavelengths. Lower resolution observations were also made in the C and D arrays which are not discussed here. The uv [1] coverage for the 2 cm and 6 cm observations produced a clean beam size of $0.''82 \times 0.''40$, highly elongated in the north-south direction due to the southern declination of He 2-10 (declination ≈ -26 degrees). Five radio knots were identified, which are labeled 1-5 from west to east. The uncertainty in the absolute flux calibration is $\sim$5%, based on variability of the standard sources used for calibrations (0834-201 and 3C273). For the assumed distance of 9 Mpc, 1 mJy corresponds to a luminosity of 9.2×10^{25} erg s^{-1} Hz^{-1} or 9.2×10^{18} W Hz^{-1}. The resulting fluxes are shown in Table 4.1.

4.2.2 Gemini Mid-Infrared Observations

Observations in the mid-infrared were made using the OSCIR imager on the Gemini North telescope during the scheduled OSCIR mini-queue in February 2001. Unfortunately, due to high winds, only a total of 10 minutes of “on source” integration time was possible

---

[1] Note that here “uv” does *not* stand for “ultraviolet”. Because the spatial resolution of observations is dependent on the wavelength and spacing of the radio antennae, radio observations taken with multi-element arrays are only sensitive to discrete spatial scales. The Fourier transform of these spatial scales are commonly mapped onto two orthogonal directions, u and v, and therefore “uv coverage” refers to how well the range of possible physical scales is sampled by a given set of observations.

Table 4.1: Properties of Individual Radio Knots

Parameter	Knot 1	Knot 2	Knot 3	Knot 4	Knot 5
R.A. (2000)	08 36 15.01	08 36 15.06	08 36 15.13	08 36 15.23	08 36 15.31
Dec. (2000)	-26 24 33.81	-26 24 33.98	-26 24 34.13	-26 24 34.00	26 24 34.61
$S_{\rm 2cm}$ (mJy)	0.94 ± 0.19	1.06 ± 0.21	0.89 ± 0.18	1.73 ± 0.34	1.04 ± 0.21
$S_{\rm 6cm}$ (mJy)	0.82 ± 0.16	0.56 ± 0.11	0.89 ± 0.18	1.10 ± 0.22	0.57 ± 0.12
α_2^6	0.11 ± 0.14	0.53 ± 0.14	0.00 ± 0.14	0.38 ± 0.14	0.51 ± 0.14
$Q_{Lyc} \times 10^{51}$	8.9	10.0	5.4	9.9	6.5
N_* 07V	890	1000	540	990	650

using only a single filter. Two sets of 5 minute observations (with small offsets in pointing) were made of He 2-10 using the N-band ($\bar{\lambda} \sim 10.8$ μm) filter. Throughout the observations, standard chopping and nodding techniques were employed in order to subtract the thermal sky background. The FWHM of the standard stars was in the range of $0.''7 - 0.''8$ throughout the observations. The field of view of the Gemini images presented in this paper is $9.''4 \times 9.''4$, and the pixel scale is $0.''089$.

The images were reduced using the OREDUCE task in the GEMINI/OSCIR package available via the Image Reduction and Analysis Facility (IRAF). The data were calibrated using the standard stars α CrB, β Leo, and γ Pix. I adopted the N-band magnitudes given by Tokunaga (1984) for α CrB and β Leo. The N-band magnitude of γ Pix was calculated using the absolutely flux calibrated spectrum given by Cohen et al. (1999) and the OSCIR filter transmission curve. The flux density in mJy was then computed using the zeropoint values found on the OSCIR webpage (ZP$= 37.8$ Jy). Point spread functions (PSFs) were build using the standard star observations, and photometry was obtained by using psf-fitting in the IRAF task DAOPHOT. The absolute uncertainty in the source fluxes are $\sim$ 20% and dominated by the uncertainties in the N-band magnitudes of the standard stars [2] . However, the relative uncertainties in the source fluxes are significantly smaller ($\lesssim$ 5% for the brightest two sources).

The total N-band flux found from this image is 660 ± 130 mJy. This value is in reason-

---

[2] As these fluxes become better characterized, it may be possible to reduce this absolute error in the coming years. At present, mid-infrared standard stars are generally not well characterized.

able agreement with that given by Telesco et al. (1993), who measured the integrated N-band flux of He 2-10 to be 600 ± 40 mJy. Both of these values, however, are substantially smaller than that found by Sauvage et al. (1997) who find an N-band flux of 1.06 Jy. This discrepancy is probably due to three factors: (1) large differences in the N-band filter transmission profiles; (2) an attempt by Sauvage et al. to incorporate a color term in their photometric calibration; and (3) non-photometric conditions during the observations of Sauvage et al. With regard to point (2), the color term correction applied by Sauvage et al. is almost certainly incorrect. They extrapolated their observed 10.1 μm flux to the N-band assuming a spectral energy distribution of $f_\nu \propto \nu$; however, the spectral energy distribution of He 2-10 near 10 μm is actually decreasing rapidly with frequency. Note also that Sauvage et al. assumed the thermal-IR emission is coincident with the optically visible starburst. As can be seen in Figures 4.1 and 4.2, the thermal-IR emission coincides with the thermal radio emission and is *not* associated with the optically visible SSCs.

Given these issues with the Sauvage et al. N-band flux and the agreement between the value I derive and the value of Telesco et al., I do not believe the discrepancy with this data and the Sauvage et al. data is a concern. Furthermore, if a blackbody spectrum is fit to the IRAS 12 μm and 25 μm data points and extrapolated to 10.8 μm, the predicted flux is 640 mJy, in excellent agreement with the observed value presented here.

It is also necessary to point out that the extent to which emission from fine structure nebular lines (e.g., [Ar III] 8.9 μm, [S IV] 10.5 μm, and [Ne II] 12.8 μm) and polycyclic aromatic hydrocarbons (PAHs, at 8.6 μm, 11.3 μm, and 12.6 μm) might be contaminating the observed fluxes in the N-band filter is not known. Starburst galaxies are known to exhibit a wide range of strengths for these features (Madden 2000). A recent mid-IR spectrum of the dwarf starburst galaxy NGC 5253 presented by Crowther et al. (1999) shows virtually no sign of PAH emission (this is the only other galaxy known to host similar radio sources which has been studied in the mid-IR to date). Therefore, I tentatively assume that these features do not contribute substantially to the N-band flux, but follow-up mid-IR spectroscopy is planned to investigate this

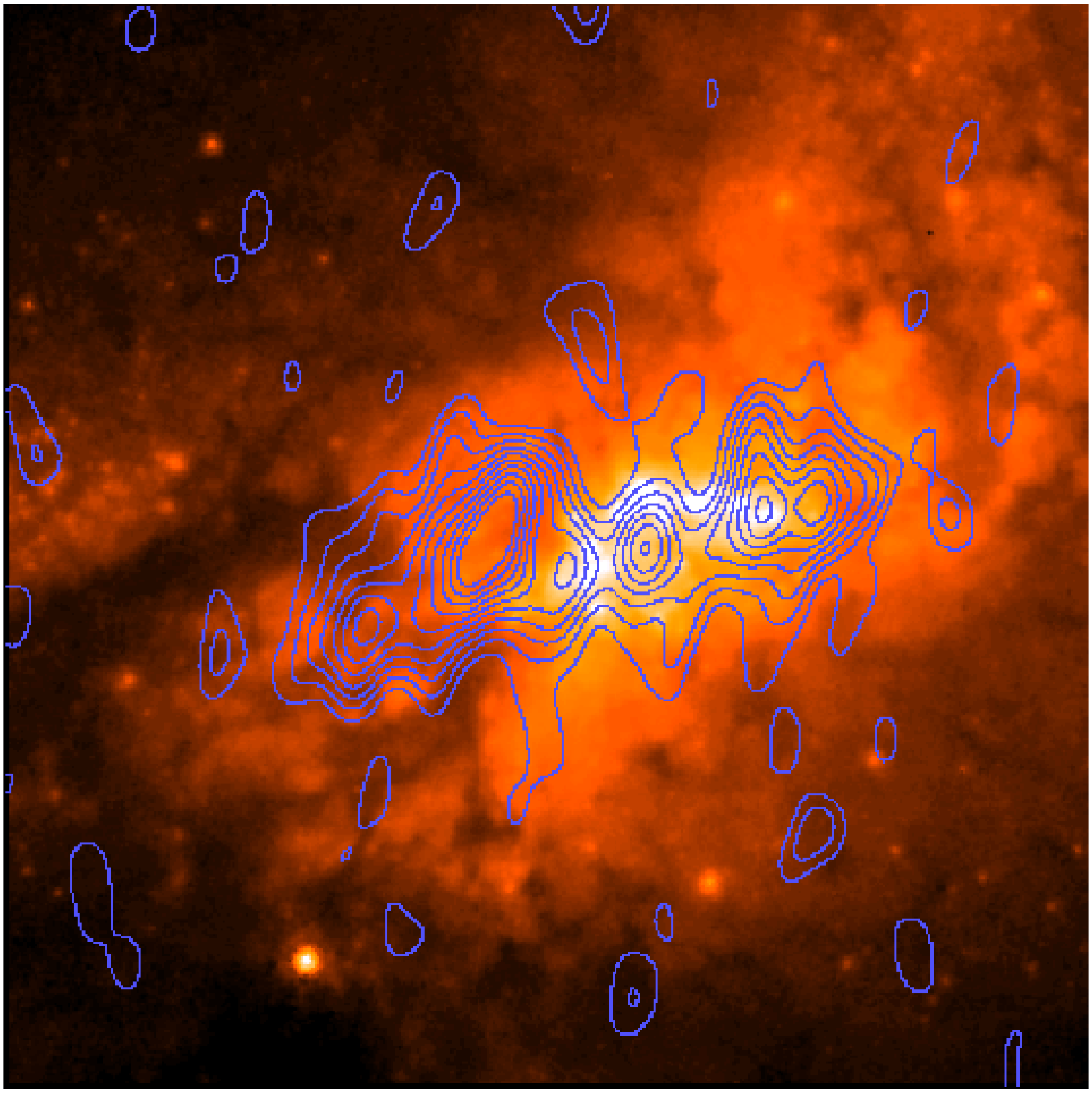

Figure 4.1: HST WFPC2 F555W (V-band) image of He 2-10 in colorscale overlaid with VLA B-array 2 cm radio continuum contours with a synthesized beam of $0.''82 \times 0.''40$ FWHM. This image is approximately $9.''4 \times 9.''4$, and shown at the same scale and orientation as Figure 4.2. It is clear that the 2 cm radio sources do not correspond to the optical SSCs.

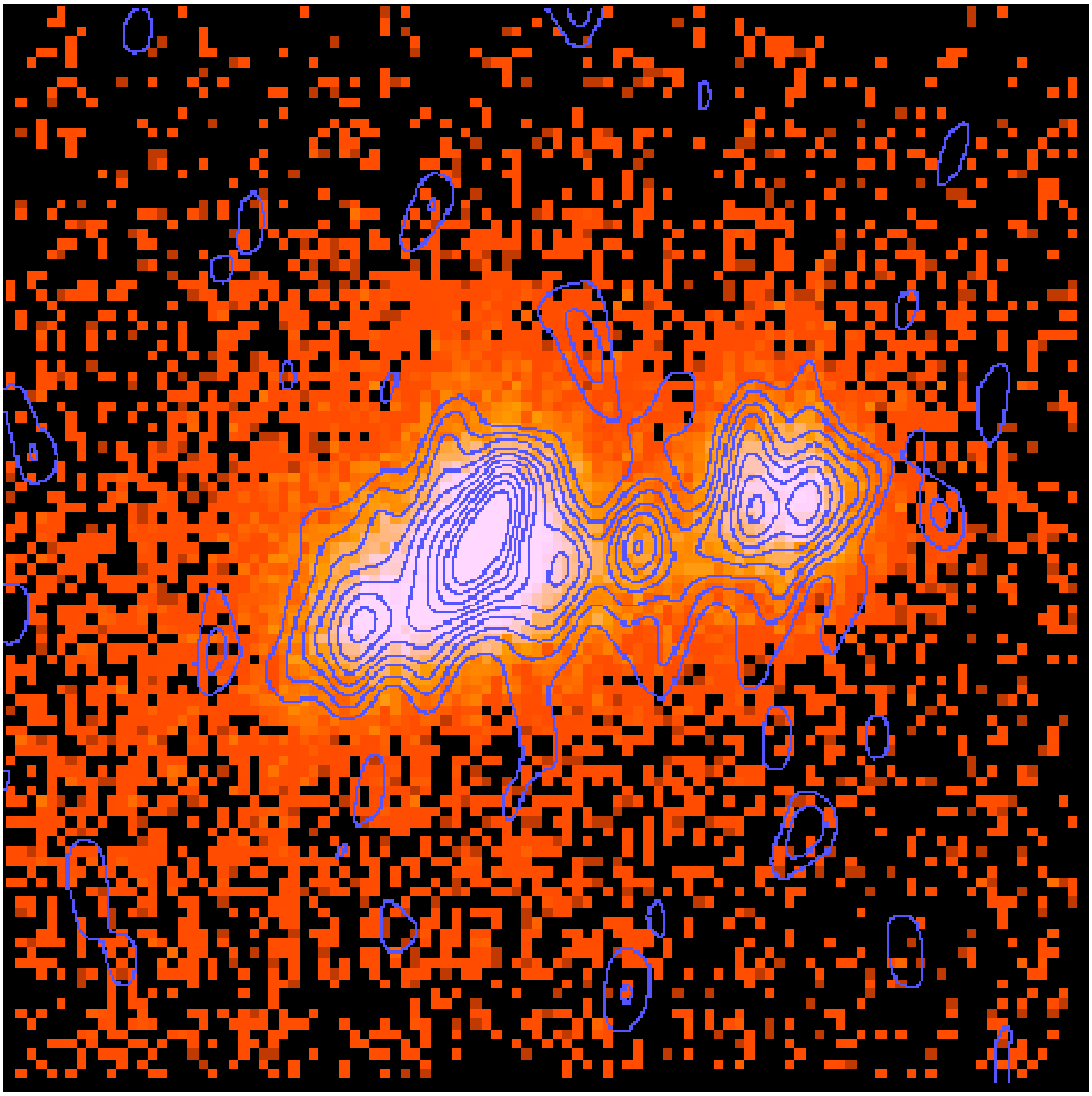

Figure 4.2: Gemini N-band image of He 2-10 in colorscale overlaid with the same 2 cm contours as Figure 4.1. At least three of the five radio sources are also strong mid-IR sources. The mid-IR morphology is strongly correlated to the radio morphology, but quite dissimilar from the optical morphology.

possibility.

The combined N-band flux of the three “detected” radio sources compared with the total N-band flux of He 2-10 (as derived in this chapter, quoted in Telesco et al. 1993, or estimated from the IRAS flux) suggests that at least $\sim 60\%$ of the 10.8 μm flux of the *entire* galaxy can be attributed to only these three objects. Based on the relative morphologies of the diffuse N-band flux seen in the Gemini image, is appears that very little of the remaining flux is due to dust heated by the starburst component seen in the UV and optical bands. Most of the diffuse background has a morphology similar to that of the radio sources, but on a larger scale. Therefore, it is possible that some of this diffuse background flux in the N-band arises from dust which is heated by radiation escaping from the embedded H II regions. If this is indeed the case, then nearly all of the observed N-band flux, and by extension nearly all of the observed flux from He 2-10 in the IRAS bands would be attributable to these enshrouded stellar clusters. Given the vigorous recent star formation throughout He 2-10, as discussed in Chapter 3, this result is rather remarkable.

4.3 Comparison of Optical, Radio, and Mid-IR Images

Figures 4.1 and 4.2 show the 2 cm radio contours overlaid on both the optical V-band HST image (from Chapter 3) and the Gemini N-band image. The morphology of the radio emission and the mid-IR emission are nearly identical. However, these images reveal a striking *dissimilarity* between the optical morphology and that of the radio and mid-IR. Five radio knots are apparent (labeled knots 1 through 5 from west to east), three (possibly four) of which are also extremely bright N-band sources — knots #1, 4, and 5 are readily detected and #2 is likely to be blended with #1 (the remaining radio source may also have mid-IR emission not detected in the signal to noise allowed for in only the 10 minutes of integration time achieved).

The absolute coordinates of the radio map are accurate to $0.''05$, while the HST image are uncertain by $\sim 0.''5$, limited by the positional uncertainties of the guide stars from the Guide Star Catalog (Lasker et al. 1990). This leads to a relative positional uncertainty between the radio and optical image of $\sim 0.''5$. Although there is a relative uncertainty of $0.''5$ between the radio and optical image, there is no obvious correlation between the morphology 6-8 optical/UV star clusters in the nuclear region of He 2-10 (distributed in a chevron configuration) and the radio point sources. Given any possible $0.''5$ translation of the optical image, no more than 2 of the radio sources would have a corresponding optical counterpart. Given the high extinction in the core of this galaxy, it is not surprising that the optical and radio morphologies are so different.

4.4 The Nature of These Radio Sources

In order to determine the nature of these radio sources, let us first review the observational constraints which must be satisfied. (1) There appear to be at least five such sources in He 2-10 at sufficient signal to noise to be detected with these radio observations. (2) Each of these sources has a *positive* spectral index ($\alpha > 0$, where $S_\nu \propto \nu^\alpha$: higher fluxes at shorter wavelengths). (3) The sources have 2 cm and 6 cm luminosities of $\sim (5-10) \times 10^{25}$ erg s^{-1} Hz^{-1}. (4) Based on a comparison with lower quality data from 1984 and 1985, these same radio sources are present with the same fluxes (within the relative error) over roughly ten years. (5) These radio sources each have corresponding 10 μm fluxes of ~ 100 mJy at 9 Mpc. With these constraints in mind, possible types of radio sources can be put to the test.

4.4.1 Could These Objects be Supernovae Remnants?

Some of the most "conventional" radio objects are supernovae (SNe) and supernovae remnants (SNR). He 2-10 has recently undergone a great deal of star formation (Chapter 3), therefore it would be quite surprising if this galaxy were not prodigiously producing SNe. This expected multiplicity easily passes criterion (1).

The first clue that these objects are not SNR is their positive spectral index; typical SNR have $\alpha < -0.4$, although not all SNR obey this "rule" — in particular, there is a class of "composite" or "plerionic" SNR (as coined by Weiler & Panagia 1978) that are known to have atypically flat spectral indices ($-0.3 < \alpha < 0.0$). In fact, in the first few hundred days after an SNe explosion, α can actually be positive (Weiler et al. 1986). Consequently, the positive spectral indices of the radio objects in He 2-10 make it extremely unlikely that they could be SNR, failing criterion (2). Since the radio fluxes of SNe have typical decay times of a few years (Weiler et al. 1986), criterion (4) is almost certainly failed.

Criterion (5) is also failed by SNR. In the survey of Arendt (1989), he found that only $\sim$ 1/3 of SNR in the galaxy are even visible in the IRAS observations. The SNR which are apparent in the IRAS observations have 12 μm fluxes which are almost exclusively less than 10^3 Jy at galactic distances of $\sim$ 10 kpc. At the distance of He 2-10, these SNR would have 10 μm fluxes $\lesssim$ 1 mJy (two orders of magnitude fainter than the 10 μm fluxes observed for the objects in He 2-10).

Finally, is it possible that these objects could be old SNR which are fading at a slower rate than bright young SNR? The luminosities of typical SNR in the Milky Way are several orders of magnitude less luminous, ranging from 8×10^{21} erg s^{-1} Hz^{-1} for 1000 yr old remnants to 7×10^{24} erg s^{-1} Hz^{-1} for Cas A (330 yr old remnant). At the distance of He 2-10, a bright young SNR like Cas A would be only a $\sim 2\sigma$ detection in these observations, thus failing criterion (3). In this case, 4 out of 5 observational criteria were failed, and SNR are ruled out as a plausible origin for the radio objects in He 2-10.

4.4.2 Could These Objects be AGN?

Active galactic nuclei (AGN), such as radio loud quasars, can be quite luminous radio sources. From the sample of Kellermann et al. (1989), such quasars can be brighter than $\sim$ 10 mJy at 6 cm, easily passing criterion (3). Some AGN are also known to have flat to slightly positive spectral indices ($\alpha \gtrsim -0.3$, e.g., Nagar et al. 2000, although some of these “AGN” are not conclusively ruled out as star forming nuclei). Therefore, criterion (2) is not necessarily failed in this case. It is also not possible to rule out AGN based on criterion (4); while AGN are known to have variations in their radio luminosities, these variations are not necessarily monotonic. An AGN could very plausibly be observed at roughly the same luminosity in observations separated by 10 years. The mid-infrared luminosities of AGN (dominated by the reprocess of radiation in their dust tori) could also easily surpass criterion (5) (Urry & Padovani 1995).

Criterion (1) presents the real hurdle for AGN as candidates for the radio objects in He 2-10. While in some galaxy mergers involving large spiral galaxies which each hosted its own AGN, the young merger remnants may still have two discrete nuclei and therefore may also contain two AGN. However, even a single AGN is unlikely to be found in a dwarf galaxy, and five AGN in a single dwarf galaxy even more unlikely. As a result AGN are ruled out as a possibility for the radio sources in He 2-10.

4.4.3 Could These Objects be Enshrouded H II Regions?

Compact H II regions are strong sources of free-free emission and represent most plausible option for the origin of the radio sources in He 2-10. From Chapters 2 and 3, it is clear that massive star clusters are formed in starburst galaxies such as He 2-10. If the star formation in He 2-10 has been roughly continuous over the last 10 Myr, then for $\sim$ 80 SSCs formed in this time period, we should expect $\sim$ 8 SSCs to be formed every million years. Therefore, it is entirely plausible that several radio sources attributable to SSC formation should be present, and criterion (1) is easily passed.

Flat or positive spectral indices like the ones observed in He 2-10 are common for compact H II regions in the Galaxy on sub parsec scales (e.g, see the compilation of Wood & Churchwell 1989a for ultra-compact H II regions, UCH IIs). This type of spectral energy distribution is well understood in the case of UCH IIs as thermal bremsstrahlung emission which has a high turnover frequency due to extremely high electron densities, thereby meeting criterion (2).

Criterion (3) could not be met by individual massive stars embedded in dense H II regions, as is the case for UCH IIs, but rather would require several hundred massive stars to create such luminous H II regions at radio wavelengths. However, this is exactly what one should expect to observe when massive star clusters, such as SSCs, are early in their evolution.

Criterion (5) can also be met in this way; individual UCH II regions in the Galaxy have typical 10 μm fluxes of 10^{2-3} Jy (Wood & Churchwell 1989b), which is not sufficient to match the observed 10 μm fluxes. However, several hundred to a thousand UCH II regions (which we might expect to find in extremely young clusters) would easily meet this requirement.

Finally, we come to criterion (4); ten years is an extremely short timescale in terms of SSC evolution, and any measurable change in the observed flux over this timescale is not expected (e.g., Leitherer et al. 1999). I will discuss the timescale on which we might expect to find such dense embedded H II regions in §4.6.1.

The most plausible conclusion is that the radio sources in He 2-10 are extremely dense H II regions powered by massive star clusters (SSCs) early in their evolution. In fact, perhaps we should even *expect* to find such objects in starburst galaxies.

4.5 Physical Properties of the Dense H II Regions

Given the luminosities and radio spectral energy distributions of H II regions, their physical parameters such as emission measure, size, and electron density can be estimated. In Figure 4.3 the 2 cm (14.9 GHz) and 6 cm (4.8 GHz) fluxes of each point source are plotted to show the rising nature of the radio spectrum toward higher frequencies. Since the absorption coefficient for optically thick free-free absorption, κ_ν, is proportional to ν^{-2}, there is a turnover frequency ν_t below which a plasma becomes optically thick to radiowave frequencies and the spectral index changes from $\alpha = -0.1$ to positive values, approaching the blackbody limit of $\alpha = 2$ as $\tau \to \infty$.

The spectral energy distribution for each of the three objects detected with Gemini are shown in Figure 4.4. In these plots, the radio and mid-IR data points are combined with the estimated IRAS fluxes for each knot. Since the IRAS observations are not at a sufficient spatial resolution to isolate the individual sources, these fluxes were derived for each knot by multiplying the total IRAS fluxes for He 2-10 by the fractional contribution of each knot to the total N-band flux (in other words, it was assumed that the fraction of light each source contributed to

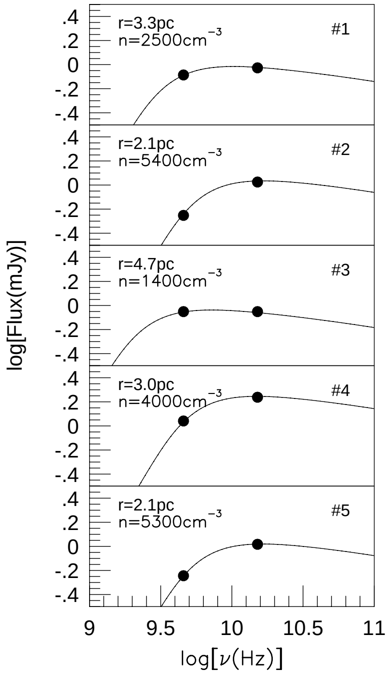

Figure 4.3: VLA 6 cm and 2 cm fluxes for the five radio knots in He 2-10. Model spectral energy distributions are shown for an ionized sphere of hydrogen with uniform temperature and density. The radius and density used to model each source are listed in the upper left corner.

the N-band will be the same relative fraction in the IRAS observations). These spectral energy distributions bear a remarkable resemblance to those for ultracompact H II regions (e.g., Wood & Churchwell 1989b).

4.5.1 Emission Measures

Using the analytical approximation of Mezger & Henderson (1967), the emission measure, $EM = \int n_e^2 dl$, can be estimated given an electron temperature, T, the observing frequency, ν, and the optical depth at that frequency, τ.

$$EM(\mathrm{cm}^{-6}\ \mathrm{pc}) = 12.2 \left[\frac{T_e}{(\mathrm{K})}\right]^{1.35} \left[\frac{\nu}{(\mathrm{GHz})}\right]^{2.1} \tau. \tag{4.1}$$

The positive spectral index for these sources arises from free-free emission where $\tau \gtrsim 1$, therefore I assume $\tau = 1$ as a lower limit. Adopting T_e=6000 K based on the spectroscopy of Kobulnicky et al. (1999), the resulting emission measures are in excess of $\sim 5 \times 10^7$ cm^6 pc at 6 cm (for $\tau > 1$ these emission measures will be correspondingly higher).

4.5.2 Comparison With Model H II Regions

In order to better constrain the properties of these sources, I have created model H II regions (spherical, uniform electron density and electron temperature) of radius, R, electron temperature, T_e, and electron density, n_e. Only free-free emission and absorption processes are considered, and a temperature of 6000 K is assumed, based on the work of Kobulnicky et al. (1999). The models are somewhat insensitive to variation in temperature in a reasonable range about this value; since the optical depth goes as $\tau \propto \mathrm{T}^{-3/2}$, the main effect of changing the assumed temperature is to shift the turnover frequency. For a reasonable range in temperatures (e.g., 5000 - 8000 K), the turnover frequency could only shift by $\lesssim 0.5$ GHz.

In Figure 4.3 the resulting spectral energy distributions are shown for a range of models. The luminosities and spectral indices of these compact sources are well-fit by model H II regions with a radius of 2—5 pc, and electron densities of 1400-5400 cm^{-3} at a distance of 9 Mpc. In

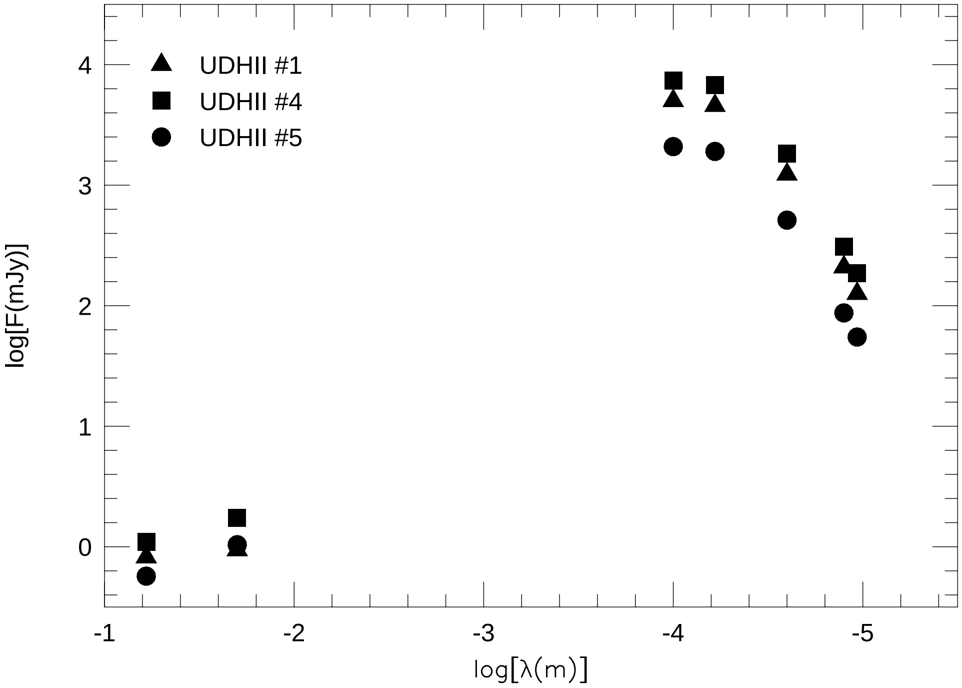

Figure 4.4: The spectral energy distribution of the UDH II s in He 2-10. The 12 μm, 25 μm, 60 μm, and 100 μm have been estimated by multiplying the total IRAS flux of He 2-10 by the fractional percentage of the total N-band flux for each UDH II.

reality, we might expect that the radio structures are not single monolithic H II regions, but a collection of smaller H II regions with higher densities embedded in a lower density medium, however this picture is not yet clear.

4.5.3 Limits on the Contribution From SNe

In § 4.4 it was clear that these radio sources could not be SNe or SNR, but rather are most likely to be embedded H II regions. Never the less, it is possible that non-thermal flux from SNe and SNR might be contributing to the observed fluxes. The lowest frequency observed (in this case 4.58 GHz) can be used to place an *upper* limit on both the SN frequency and the fraction of the highest frequency flux (in this case 15 GHz) which might be due to non-thermal emission. In order to make these estimates, it is necessary to examine the case, as an *upper* limit, that all of the 4.8 GHz flux is due to synchrotron radiation. The maximum amount of non-thermal emission at 15 GHz is given by,

$$S_{15\ \mathrm{GHz}} \leq \left(\frac{15\ \mathrm{GHz}}{4.58\ \mathrm{GHz}}\right)^{\alpha} S_{4.58\ \mathrm{GHz}}. \tag{4.2}$$

Adopting $\alpha \sim -0.8$ (typical of synchrotron sources in the Galaxy, Condon 1992), the maximum amount of non-thermal flux which could be contaminating the 15 GHz observations is $\lesssim 0.4\ S_{4.58\ \mathrm{GHz}}$.

Following Condon & Yin (1990) and Condon (1992), the SN frequency can also be constrained. The relation between the SN frequency and non-thermal luminosity is given by,

$$\frac{L_{\mathrm{non-thermal}}}{10^{22}\mathrm{W\ Hz^{-1}}} \approx 13\left(\frac{\nu}{\mathrm{GHz}}\right)^{\alpha}\left(\frac{\nu_{\mathrm{SN}}}{\mathrm{yr^{-1}}}\right). \tag{4.3}$$

As an example using knot 4 (the brightest knot in this sample), and again adopting $\alpha \sim -0.8$ (Condon 1992), the maximal SN frequency is given by $\nu_{\mathrm{SN}} \lesssim 2 \times 10^{-4}\ \mathrm{yr^{-1}}$. Using the Starburst99 models of Leitherer et al. (1999), this SN frequency is almost an order of magnitude less that the SN frequency expected when SN begin to occur at an age of $\sim$ 4 Myr for a model cluster. Therefore, it is unlikely that SNe have begun to occur in significant numbers, if at all, and we expect the non-thermal contamination in these data to be insignificant. Moreover, the paucity of SNe puts an absolute upper limit on the ages of these clusters of $\sim$ 4 Myr (although, as we will see in § 4.6.1 the ages can be constrained to much younger values with other methods).

4.5.4 Ionizing Radiation

The production rate of Lyman continuum photons, and thus the stellar content of each of the embedded H II regions can be estimated from the thermal radio luminosity following Condon (1992),

$$Q_{Lyc} \geq 6.3 \times 10^{52}\ \mathrm{s}^{-1} \left(\frac{T_e}{10^4\ \mathrm{K}}\right)^{-0.45} \left(\frac{\nu}{\mathrm{GHz}}\right)^{0.1} \left(\frac{L_{thermal}}{10^{27}\ \mathrm{erg\ s^{-1}\ Hz^{-1}}}\right). \tag{4.4}$$

Since the non-thermal component becomes weaker at higher frequencies, the luminosity measured at the highest radio frequency (in this case 15 GHz) is used to determine Q_{Lyc}. The resulting values determined from this method are presented in Table 4.1.

One should also bear in mind that the Q_{Lyc} values determined with this method could suffer from two different problems: (1) if the source is, in fact, optically thick even at the highest frequency measured, this method will *underestimate* the actual ionizing luminosity, and (2) if there is contamination from non-thermal emission in the beam at the frequency used, the ionizing luminosity will be *overestimated*. However, the overall non-thermal background of the galaxy will tend to be resolved out with the small synthesized beams used in these observations. Therefore the only non-thermal flux which might boost the 15 GHz luminosity would be SNe within the objects themselves. I estimate the maximum affect this might have in § 4.5.3, and do not expect any significant contribution.

Further evidence for deriving the ionizing luminosity from this method comes by comparing the total Q_{Lyc} calculated for He 2-10 using the 15 GHz flux with the total Q_{Lyc} calculated from optical Hα observations; Q_{Lyc} determined in the radio should include the ionizing flux apparent in optical light, the ionizing flux which is optically obscured, and any non-thermal contamination. As a result, if there is non-thermal contamination, the radio Q_{Lyc} cannot be less than the optically determined Q_{Lyc}. Conversely, if the radio Q_{Lyc} is less than the optically determined Q_{Lyc} that implies that the radio value is *underestimating* the ionizing luminosity. Kobulnicky & Johnson (1999) find $Q_{Lyc} = 2.0 \times 10^{53}$ s^{-1} for the entire galaxy using the 15 GHz luminosity. The Méndez et al. (1999) Hα measurement yields $Q_{Lyc} = 2.1 \times 10^{53}$ s^{-1}, which is only marginally larger than the value determined in the radio. Therefore, I conclude that non-thermal contamination is *not* significantly contributing to the 15 GHz flux, and this method for deriving Q_{Lyc} will not be an overestimation, but rather is quite possibly an underestimation.

4.5.5 Stellar Content

The production rate of Lyman continuum photons from these sources can be used to estimate the number of massive stars powering the observed emission. Following the convention of Vacca (1994) and Vacca et al. (1996), a “typical” O-star (type O7V) produces $Q_{Lyc} = 1.0 \times 10^{49}$ s^{-1}. Using this method, 20,000 such O stars are required to power the total observed radio ionizing luminosity from He 2-10. Each of the individual embedded clusters require between 500 and 1000 equivalent O7V stars in order to produce their ionizing luminosities (see Table 4.1). Thus, each embedded cluster contains more O stars than are found in the entire 30-Doradus nebula in the LMC (~ 200, Vacca et al. 1995). Using the Starburst99 models of Leitherer et al. (1999) with solar metallicity, Salpeter IMF, an upper mass cutoff of 100 M$_\odot$, and a lower mass cutoff of 1 M$_\odot$, starburst knots producing this range of Lyman continuum photons at an age of 1 Myr would have masses of 0.8 - 1.6$\times 10^5$ M$_\odot$ (if the lower mass cutoff is $<$ 1 M$_\odot$, these mass estimates will be correspondingly higher). These masses are consistent with those found for the optical SSCs in He 2-10 (Chapter 3) which have already emerged from their birth material, thus strengthening the connection between UDH IIs and SSCs.

Since the star-forming regions seen in these radio observations are not seen even faintly on the HST V- or I-band images (or even in the near-infrared, Vacca et al. in preparation), their visual extinctions must be quite large. Such large extinction values are consistent with the column density of molecular gas observed in this region (Kobulnicky et al. 1995) and the extinction estimates from the infrared silicate features ($A_V \simeq 30$, Phillips et al. 1984). Given that He 2-10 was already known to contain 31,000 O stars (Conti & Vacca 1994) the additional ∼4000 O stars contained in these five dense, heavily obscured H II regions represent a significant faction of the massive stars in He 2-10.

4.6 Discussion

The major result of this chapter is the discovery of multiple optically thick free-free sources, most plausibly dense H II regions powered by extremely young embedded massive star clusters. The majority of these sources do not coincide with features visible in the optical HST images, leading to the conclusion that they are heavily obscured by dust. The combination of high obscuration and high density inferred from the free-free optical depth is consistent with very dense H II regions. While such dense, optically-thick, inverted-spectrum H II regions exist in abundance around *individual* stars in the Galaxy (i.e., ultracompact H II regions; Wood & Churchwell 1989b) this phenomenon had not been previously seen on such large spatial and energetic scales. Because of their similar densities to ultracompact H II regions in the Galaxy, we might term them “ultra dense H II regions” (UDH IIs).

4.6.1 On the Lifetimes of UDH IIs

If UDH IIs are similar to (albeit vastly scaled up) from UCH IIs, it seems likely that the fraction of time a super star cluster spends in the UDH II phase is a small fraction of the massive star lifetime. In accord with the estimated lifetimes of individual UCH II regions based on the number of UCH II regions compared with the number of optically visible O stars in the Galaxy (e.g., Wood & Churchwell 1989a) is $\approx 10 - 15\%$. Indeed, UCH II region lifetimes have been a topic of much discussion since Wood & Churchwell (1989b) introduced the “lifetime problem”; in short, if UCH II regions are significantly overpressured with respect to the surrounding ISM, they should expand and dissipate on time scales $\approx 10^4$ years. However, the number of UCH II regions observed is greater than is allowed for by this time scale.

Several mechanisms have been proposed to address this issue, most of which are also likely to be applicable to UDH IIs. Wood & Churchwell (1989b) proposed that infalling matter or bow shocks might act to increase the external pressure, thus extending the UCH II phase. It is also possible that the ambient pressure is typically significantly higher than the value used by Wood & Churchwell (1989b), as proposed by de Pree et al. (1995). The lifetimes of UCH II regions could also be extended if they are replenished by material photoevaporated from the surrounding circumstellar disks (e.g., Hollenbach et al. 1994).

The first argument for the extreme youth of UDH II regions is simply by analogy to UCH II regions in the Galaxy. If UDH IIs are composed of individual UCH II regions, we should expect them to have similar lifetimes provided that star formation is relatively instantaneous over the massive star cluster. As is the case for UCH II regions, the densities in UDH IIs are likely to be extremely high, and the implied pressures constitute an over-pressure compared to typical ISM pressures. If the surrounding ISM has typical densities of $n_e \sim 100$ cm^{-3}, then these embedded H II regions with densities of $n_e \sim 5000$ cm^{-3} are at an overpressure of ~ 50. To first order, such over-pressed regions must rapidly expand and disperse on time scales comparable to the sound-crossing time scale which is a few$\times10^5$ years for $c_s \approx 10$ km s^{-1}. However, as discussed above for UCH II regions, it is entirely possible that the ambient pressure around UDH IIs is not "typical" of the global ISM and might present a mechanism for extending the lifetime of the UDH II phase.

The second method to estimate the lifetimes of UDH IIs is to compare the fraction of ionizing stars in UDH II regions with the total number of ionizing stars in the galaxy. The total Lyman continuum photon production rate, Q_{Lyc}, of the UDH II regions in He 2-10 is 4.7×10^{52} s^{-1} (provided there is no leakage from the enshrouding cocoon that would likely result in associated Hα emission). The Q_{Lyc} determined optically for the entire galaxy He 2-10 is 2.1×10^{53} s^{-1} (Méndez et al. 1999), implying a total $Q_{Lyc} \sim 2.5\times10^{53}$ s^{-1}. Thus, the UDH II regions contain $0.18\times$ the total ionizing photons. It then follows that if the star formation has been reasonably continuous in this system over the last 10 Myr, a plausible estimate for the typical duration of the UDH II phase is $\sim$ 18% times the typical massive star lifetime ($\times10^7$ yr), remarkably in accord with the estimates for individual UCH II regions. This method implies a mean lifetime of roughly 1 – 2 Myr for UDH II regions, although if strong star formation has been occurring over less than 10 Myr, this estimate will be correspondingly lower. A similar method to estimate the lifetimes of UDH IIs is simply to compare the number of clusters which are no longer enshrouded (~ 76 from Chapter 3) to the number of UDH IIs. Given that the optical clusters in He 2-10 are typically less than 10 Myr old, this method implies the UDH II phase only lasts a few$\times10^5$ years, which is slightly lower than the lifetimes estimated with the first method. While these estimates are very crude, a reasonable lifetime for the UDH II phase is perhaps $\lesssim$ 1 Myr.

Perhaps the weakest argument in favor of the extreme youth of UDH II regions comes from their high visual extinctions. In §4.3 it is clear that the UDH II regions are not visible at optical wavelengths. This picture is consistent with UDH IIs being extremely young H II regions still hidden from view by the dust associated with their natal molecular clouds. However, one must also bear in mind that we cannot rule out screens of dust not physically associated with the regions of optically thick free-free emission.

4.6.2 UDH IIs in Other Starburst Systems?

It would be quite surprising if the UDH II phenomenon was unique to He 2-10. If UDH IIs do indeed represent the early stages of SSCs evolution, then they ought to be present in most (if not all) starburst galaxies. High resolution 2 cm and 6 cm radio observations of a large sample of starburst systems acquired in scaled B and A-array configurations with the VLA will be required to examine this issue. To date, such high spatial resolution data generally exist only for more luminous systems like quasars and AGN. In some cases (as will be discussed in the following chapter) perhaps other star-forming galaxies contain dense, heavily obscured H II regions like the five in He 2-10, but they have simply not been identified as such. Never the less, very little data currently exists which can adequately address the ubiquity of UDH IIs, and this area of research will benefit from an extensive observing campaign.

Turner et al. (2000) detected one such object in the nucleus of the galaxy NGC 5253. NGC 5253 is a dwarf starburst galaxy in the Centaurus group of galaxies at a distance of $\sim$ 4.1 Mpc (Sandage et al. 1994). The radio object in NGC 5253 has estimated properties which are fully consistent with it being a genuine UDH II. In fact, follow-up work by Gorjian et al. (2001) has also confirmed this UDH II with mid-IR Keck observations. Turner et al. estimate that this object has a radius of ~ 2 pc, and has an ionizing photon rate of $Q_{Lyc} \sim 10^{51-52}$ s^{-1}, in close agreement with the results of this chapter. My own analysis of this system, using the 2 cm fluxes from Turner et al. (1998) and the 1.3 cm fluxes from Turner et al. (2000), indicate a best-fit radius of 3.6 pc and an electron density of $n_e \approx 5000$ cm^{-3} (Figure 4.5) for an electron temperature of 11,000 K (as derived by Kobulnicky et al. 1997). These values are remarkably close to the electron densities and radii found for the UDH IIs in He 2-10 in § 4.5.2.

Arguably the most well known starburst in the local universe is M 82, making it an obvious object for comparison. With a distance of only ~3.6 Mpc (Freedman et al. 1994), it can be studied at higher spatial resolution than He 2-10. Radio continuum maps presented in Allen & Kronberg (1998) show 26 compact sources with linear diameters of 3.5 pc ($0.''2$) and 2 cm spectral luminosities of 2.9$\times 10^{24}$ erg s^{-1} Hz^{-1} to 7.3$\times 10^{25}$ erg s^{-1} Hz^{-1} (fluxes of 0.2 mJy to 5 mJy). Of the 26 sources in M 82, 22 show distinctly non-thermal spectral indices and are consistent with supernova remnants. Their radio spectra often show turnovers, but only at low frequencies ($\nu < 1$ GHz), due to free-free absorption in the surrounding ionized gas. Only one source has a thermal spectrum typical of an H II region, but it is quite flat with no indication of a turnover due to free-free absorption. de Grijs et al. (2001) suggest that M 82 has possibly undergone several starburst episodes and hosts sites of “fossil” starbursts. Perhaps M 82 is between starburst events, or even possibly post-starburst, and therefore not producing UDH IIs in large numbers.

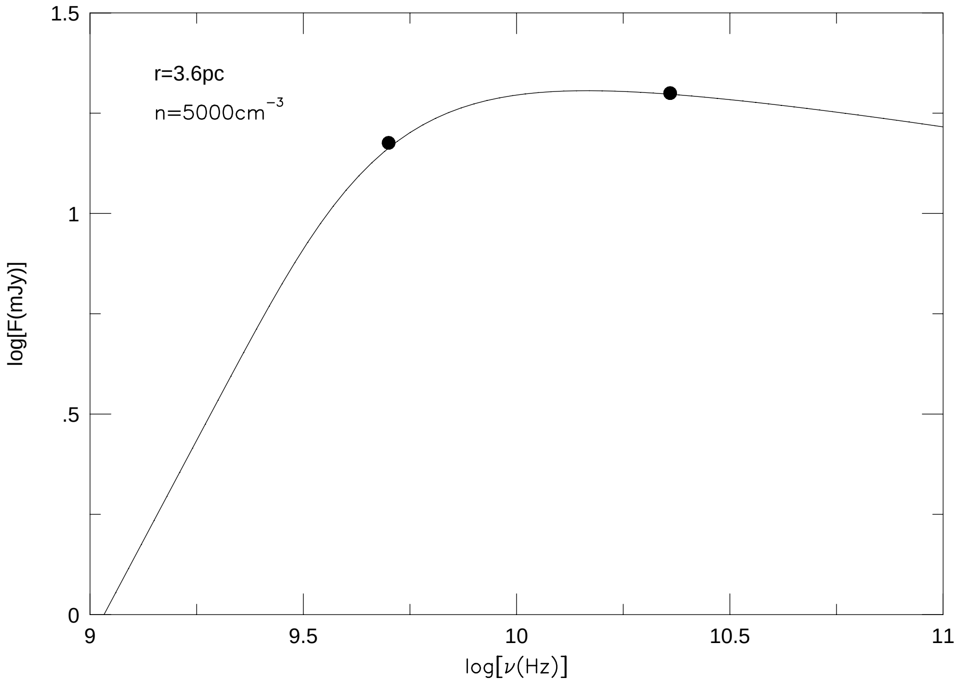

Figure 4.5: Best fit electron density and radius for the UDH II in NGC 5253 detected by Turner et al. (2000). The models are the same as described in § 4.5.2 and use an electron temperature of 11,000 K as derived by Kobulnicky et al. (1997).

4.6.3 Implications for the Infrared-Radio Correlation?

There is a well-known correlation between the infrared and radio fluxes of galaxies over a wide range of Hubble types as first reported by van der Kruit (1971). This relation is typically represented by the logarithmic far-infrared(FIR)-to-radio flux ratio

$$q \;\equiv\; \log\,[(\mathrm{F_{FIR}}\;/\;3.75\times10^{12}\;\mathrm{Hz})\;/\;S_{1.49\mathrm{GHz}}], \tag{4.5}$$

where $\mathrm{F_{FIR}}$ is an approximation of the flux between ~ 40 and ~ 120 μm as

$$\mathrm{F_{FIR}}\;(\mathrm{W\;m^{-2}})\;\equiv\;1.26\times10^{-14}\;(2.58S_{60\mu m}+S_{100\mu m}), \tag{4.6}$$

where $S_{1.49\mathrm{GHz}}$, $S_{60\mu m}$, and $S_{100\mu m}$ are the flux densities (in units of W $\mathrm{m^2}$ $\mathrm{Hz^{-1}}$) at 1.49 GHz, 60μm, and 100μm, respectively.

Over a range of spiral, irregular, and starburst galaxies (see Sanders & Mirabel 1996, and references therein), q is very robust with a small standard deviation; $\langle q\rangle = 2.35 \pm 0.2$. [3] For starbursts selected from the IRAS Bright Galaxy Survey, Condon et al. (1991b) find an average value of $q = 2.34 \pm 0.19$. They also find q tends to be higher for the more infrared luminous galaxies. Furthermore, *these galaxies with high q values also tend to have compact radio sources*. Condon et al. hypothesize that this class of ultraluminous infrared galaxies (ULIGs) are powered by dense, compact starbursts which are optically thick at 1.49 GHz, and whose radio flux density is therefore suppressed relative to the FIR. Correcting for the optical depth at 1.49 GHz yields a tighter FIR-radio correlation.

In the extreme case that a galaxy were entirely in the UCH II/UDH II phase, what would its q value be? To answer this question, let us use W49A as an analogy. W49A is one of the most well-studied UCH II complexes in the Galaxy and has been resolved into at least 30 UCH IIs (de Pree et al. 1997). From the Ward-Thompson & Robson (1990) values for $S_{60\mu m}$ and $S_{100\mu m}$, FIR $= 2.6\times10^{-9}$ W $\mathrm{m^{-2}}$ for W49A. From Mezger et al. (1967), F_ν(1.41 GHz)$= 30 \pm 3$ Jy.

---

[3] Notable exceptions to this correlation are radio galaxies and radio-loud QSOs, which have q values typically lower by a factor of $\sim 2-4$ (see Sanders & Mirabel (1996) and references therein).

These values yield $q = 3.36$, which is significantly higher than the average value found in normal galaxies and starbursts, and even higher than the typical q values obtained for ULIRGs.

Given the high q value derived above for W49A, which is *entirely* dominated by extremely young and embedded massive stars, we might also expect to find a high q value for the galaxies in which we have detected UDH IIs. Using the IRAS Point Source Catalog fluxes, we find that He 2-10 has $\mathrm{FIR} = 1.12 \times 10^{-12}$ W m^{-2} and NGC 5253 has $\mathrm{FIR} = 1.39 \times 10^{-12}$ W m^{-2}. From Kobulnicky & Johnson (1999), F_ν(1.42 GHz)$= 70 \pm 7$ mJy for He 2-10, and from Turner et al. (1998) F_ν(1.49 GHz)$= 76 \pm 2$ mJy for NGC 5253. The resulting q values are 2.63 and 2.69 for He 2-10 and NGC 5253, respectively, and are both significantly higher than the average value derived for starburst galaxies, but consistent with the typical value of ULIRGs. Even after correcting the radio flux from He 2-10 for self-absorption according to the prescription given by Condon et al. (1991b), q is still significantly higher than the canonical value with the corrected value of $q = 2.5$.

The most straightforward interpretation is that bulk of the star formation in He 2-10 is so young that it has not yet begun to produce SNe in the relative numbers typical in most galaxies, in agreement with the result for the embedded clusters in § 4.5.3. In other words, while the five embedded clusters in He 2-10 are largely (or solely) responsible for the mid- to far-infrared flux, they are not yet mature enough to produce synchrotron radiation in amounts necessary to obtain the standard q value.

How does the q value of the nearby starburst M82 (where there currently don't appear to any UDH IIs) compare? From Kuehr et al. (1981), the 1.4 GHz flux of M82 is 8.6 Jy, and from Soifer et al. (1989) values for the 100 μm and 60 μm fluxes are 1355 Jy and 1313 Jy, respectively. I calculate $\mathrm{FIR} = 5.98 \times 10^{-11}$, which results in $q = 2.27$. This q value is in excellent agreement with those derived for other galaxies by Condon et al. (1991b), but significantly lower than the values derived above for He 2-10 and NGC 5253, both of which are known to host UDH IIs, while M82 does not.

Although we have a sample size of only two galaxies hosting UDH IIs, they both have

$q > 2.6$, while the local starburst M82 which does not host UDH IIs have a q value significantly lower. This trend is exactly what we would expect for galaxies undergoing vigorous star formation and hosting massive UDH IIs. This tentative result lends itself two main implications: (1) q values might be useful for identifying galaxies which are most likely to host UDH IIs, and (2) because high q values are typical of ULIRGs, UDH IIs might have a significant role in powering their infrared luminosities.

Chapter 5

A Sample of Clusters of Extragalactic Ultracompact H II Regions

5.1 Background

In the previous chapter I discussed the discovery of very young massive star clusters still embedded in their birth material in He 2-10. Subsequently, a handful of other such objects have also appeared in the literature in NGC 5253 (Turner et al. 2000), NGC 2146 (Tarchi et al. 2000), and NGC 4214 (Beck et al. 2000). Embedded in these heavily enshrouded objects are hundreds of young massive stars that create surrounding H II regions and manifest themselves as optically thick free-free radio sources.

Similar dense, inverted-spectrum H II regions exist around individual stars in our galaxy (i.e., ultracompact H II regions, UCH IIs, Wood & Churchwell 1989), albeit on a vastly smaller scale. Because of their apparent spectral similarity to galactic UCH IIs, we have dubbed these extragalactic objects "ultradense H II regions" (UDH IIs). The physical properties of these clusters are truly remarkable; the estimated sizes (a few parsecs), stellar masses (a few $\times 10^{5-6}$ $M_{\odot}$), ionizing luminosities ($Q_{Lyc} \sim 10^{51-53}$ s^{-1}), and ages (possibly as young as a few $\times 10^{5}$ years) of the newly discovered UDH IIs imply that we may be witnessing the birth process of super star clusters, and therefore possibly the genesis of globular clusters. The discovery of these UDH IIs allows us to begin observing the earliest stages of the massive star cluster formation for the first time. Moreover, if UDH IIs are indeed scaled-up versions of individual UCH II regions, then perhaps we ought to find a continuous range of embedded cluster sizes, spanning the gap between a single O-type star and a thousand or more O-type stars.

We have made some progress understanding the early stages of massive star evolution in the Galaxy, but the current knowledge about the early stages of massive star evolution in other environments is mediocre at best. The present state of the research on the early stages of massive star evolution now includes both individual massive stars in the Galaxy (UCH II regions) and massive star clusters in a handful of other systems (UDH IIs, Chapters 4 and 5). However, little is known about individual massive stars in other galaxy systems. Perhaps the most logical place to study individual massive stars early in their evolution is in the galaxies closest to our own, the Large and Small Magellanic Clouds. However, data with sufficient angular resolution to disentangle individual massive stars in the Magellanic Clouds is not yet available. Despite this instrumental contraint, it is still possible to find “candidate” UCH IIs even with large-beam data. In Appendix A, I present the results of a search for UCH II region candidates in the Magellanic Clouds using previously published radio data in combination with sources cataloged by IRAS. The large beamsizes in these surveys do not allow us to accurately estimate the physical properties of these candidate UCH II regions; however I include this list for completeness.

Because UDH IIs have only recently been identified, one of the primary goals in this new field of study is simply to expand the sample of known objects in order to understand their properties in a statistical sense. To this end, I have searched for previously published radio observations that may have also serendipitously detected UDH IIs. Multiwavelength radio observations taken to study supernovae remnants in nearby galaxies are particularly useful for this purpose. In most cases, the original authors have identified the candidate UDH IIs I present here as “thermal sources” or “H II regions.” I seek sources with positive radio spectral indices ($\alpha > 0$, where $S_\nu \propto \nu^\alpha$), implying an optically thick free-free origin. In this chapter, I utilize previously published radio observations of M33, NGC 253, and NGC 6946 to identify new candidate UDH IIs, determine their number of ionizing stars, and estimate their physical sizes, densities, and masses.

5.2 Galaxies in This Sample

Here I overview basic properties of the galaxies in this sample and only highlight the radio observations utilized in this paper. I refer the reader to the original papers for more detail on the observations and reduction. Because the observations were compiled from a variety of sources, the observations are heterogeneous in nature, and in some cases, non-ideal for my purposes. For example, in order to obtain accurate relative fluxes at multiple frequencies it is desirable to have well-matched beam sizes; I will discuss the impact of mismatched beams in § 5.3.1. However, these data provide a valuable resource for this fledgling field and will serve as a useful baseline for follow-up observations.

5.2.1 M33

M33 (NGC 598) is a Local Group spiral galaxy (Sc(s)II-III), nearly face-on ($i = 55^\circ$, Garcia-Gomez & Athanassoula 1991), and it is rich in H II regions (Hodge et al. 1999; Courtes et al. 1987; Boulesteix et al. 1974). Young ($< 10^8$ yr) clusters in M33 were recently studied by Chandar et al. (1999), and were found to have masses of $6 \times 10^2 - 2 \times 10^4$ $M_\odot$, smaller than that typical for its old globular clusters. M33 has an areal star formation rate of SFR $=$ $10^{-2.47}$ $M_\odot$ yr^{-1} kpc^{-2} (Kennicutt 1998), making it the least prolific galaxy in this sample. At a distance of 840 kpc (Freedman et al. 1991), it is also the closest of the galaxies in this chapter.

The radio observations of M33 that I use were originally obtained by Duric et al. (1993) and also presented by Gordon et al. (1999). Both Very Large Array (VLA) B configuration and Westerbork Synthesis Radio Telescope (WSRT) observations were made of M33 at 6 and 20 cm (4.84 and 1.42 GHz) in several pointings to obtain good coverage of the galaxy. The primary beams at 20 cm were $30'$ with the VLA and $36'$ with WSRT. At 6 cm both telescopes had primary beams of $9'$. The 6 cm observations had resolutions ranging from $5''$ to $10''$, and the 20 cm observations had resolutions ranging from $5''$ to $15''$, depending on the uv taper used in the cleaning process. Matched beam observations were convolved to identical beams of $7''$

FWHM. All images have an average 3σ rms noise level of ≈ 150 μJy per beam. At the adopted distance of 840 kpc (Freedman et al. 1991), 1 Jy= 8.4×10^{26} erg s^{-1} Hz^{-1}.

5.2.2 NGC 253

At 2.5 Mpc (Turner & Ho 1985), NGC 253 is a member of the Sculptor Group. This galaxy is a nearly edge-on spiral galaxy (Sc(s)), and contains a radio continuum plume emanating from the central starburst region rising perpendicular to the disk (e.g., Carilli et al. 1992). NGC 253 has the highest star formation rate of the galaxies in this sample with SFR $=$ $10^{1.24}$ M$_\odot$ yr^{-1} kpc^{-2} (Kennicutt 1998). Four young SSCs were discovered optically in the central region of NGC 253 by Watson et al. (1996); however, only one of these clusters is apparent in the mid-IR observations of Keto et al. (1999), who propose that it might be exceptionally young. Ulvestad & Antonucci (1997) also discuss the nature of the brightest thermal radio source in NGC 253, a point that I will revisit in § 5.3.

NGC 253 was observed by Ulvestad & Antonucci (1997) with the B configuration of the VLA at 1.3 cm, 2 cm, 3.6 cm, 6 cm, and 20 cm (23.56 GHz, 14.94 GHz, 8.44 GHz, 4.86 GHz, and 1.49 GHz) between 1987 and 1995. Additional observations at 1.3 and 2 cm were made using the A configuration. As the beam sizes at 6 and 20 cm are significantly larger than at 1.3 cm, 2 cm, and 3.6 cm, I have not included this longer wavelength data in my analysis because of the unwanted background contribution from non-thermal emission. The duration of the observations in the B-array were 4.1, 5.6, and 7.0 hours at 1.3, 2, and 3.6 cm, respectively. The A-array observations at 1.3 and 2 cm were 2.8 and 4.2 hours, respectively. The primary beams varied from $2'$ to $5'$ (from 1.3 cm to 3.6 cm, respectively) and easily contain the area of interest. The synthesized beams ranged from $0.13'' \times 0.07''$ to $0.42'' \times 0.24''$ at 1.3 cm, $0.20'' \times 0.10''$ to $0.59'' \times 0.35''$ at 2 cm, and $0.33'' \times 0.19''$ to $0.36'' \times 0.21''$ at 3.6 cm. Ulvestad & Antonucci (1997) estimate the uncertainties in these data as $\sim$ 20% for 1.3 cm, and $\sim$ 10% for the 2 cm and 3.6 cm data. The 3σ rms noise levels are $\approx$ 660, 240, and 150 μJy, respectively, for the 1.3 cm, 2 cm, and 3.6 cm data. At the adopted distance of 2.5 Mpc (Turner & Ho 1985), 1 Jy$= 7.5 \times 10^{27}$ erg s^{-1} Hz^{-1}.

5.2.3 NGC 6946

NGC 6946 is the most distant galaxy in this sample at 5.1 Mpc [1] (de Vaucouleurs 1979), and is a spiral galaxy of type Sc(s)II with an inclination angle of $i = 34^\circ$ (Garcia-Gomez & Athanassoula 1991). The areal star formation rate in NGC 6946 is SFR$= 10^{-1.88}$ M$_\odot$ yr^{-1} kpc^{-2} (Kennicutt 1998). Larsen & Richtler (1999) have detected 107 young massive star clusters, one of which has received particular attention because of its age ($\sim$ 15 Myr) and mass ($\sim$ 5×10^5 M$_\odot$) (Elmegreen et al. 2000b). Sub-mm images obtained by Bianchi et al. (2000) show 850 μm emission which, in some cases, may be associated with radio sources discussed in this here.

The VLA was used to survey NGC 6946 with the B and A arrays at 6 and 20 cm (4.86 and 1.45 GHz), respectively, by Lacey et al. (1997). Approximately 8.6 hours were spent in at each frequency. The primary beams were $9'$ and $30'$ at 6 cm and 20 cm, respectively. The resulting beam sizes at the two wavelengths are very well matched: $1''.9 \times 1''.6$ at 6 cm and $1''.9 \times 1''.7$ at 20 cm. Flux uncertainties are typically $\approx$ 20%, and the 3σ rms noise levels are $\approx$ 60 and 50 μJy for the 20 and 6 cm data, respectively. At the adopted distance of 5.1 Mpc (de Vaucouleurs et al. 1976), 1 Jy $= 3.1 \times 10^{28}$ erg s^{-1} Hz^{-1}. These observations have also been analyzed by Hyman et al. (2000), who derive a luminosity function for H II region candidates with a power-law index at 6 cm of ≈ -1.2, but exclude sources with spectral indices of $\alpha > 0.2$. As result, the most optically thick sources were excluded from their sample. Nevertheless, the seven sources presented in Hyman et al. (2000) with $\alpha > 0$ are also included in this chapter (my sources 1, 2, 4, 6, 7, 8, and 10 in Tables 5.3 and 5.6).

Table 5.1: UDH II candidates in M33

#	R.A. (2000)	Dec. (2000)	L_6 $\times 10^{23}$ erg/s/Hz	L_{20} $\times 10^{23}$ erg/s/Hz	Q_{Lyc} $\times 10^{49}$ s^{-1}	α_6^{20}
1	1:33:02.4	30:46:42.9	11.9±0.8	6.8±1.7	9.7±0.9	0.46±0.11
2	1:33:16.0	30:56:45.9	16.9±1.7	14.4±2.5	13.9±1.6	0.13±0.09
3	1:33:16.5	30:52:50.3	55.9±1.7	35.6± 2.5	45.8±1.4	0.37±0.03
4	1:33:37.5	30:47:19.3	9.3±0.8	7.6±0.8	7.6±6.2	0.17±0.06
5	1:33:39.2	30:38:06.9	9.3±0.8	7.6±1.7	7.6±6.2	0.17±0.10
6	1:33:43.6	30:39:07.1	8.5±0.8	7.6±1.7	6.9±0.8	0.09±0.10
7	1:33:48.2	30:39:17.8	3.4±0.8	2.5±0.8	2.8±0.7	0.25±0.17
8	1:33:59.8	30:32:45.3	3.4±0.8	2.5±0.8	2.8±0.7	0.25±0.17
9	1:34:00.2	30:40:47.7	46.6±0.8	42.4±1.7	38.2±2.2	0.08±0.02
10	1:34:02.2	30:38:40.7	28.8±2.5	26.3±2.5	23.6±2.5	0.07±0.06
11	1:34:06.4	30:41:45.6	11.±0.8	7.6±0.8	9.0±0.9	0.30±0.06
12	1:34:13.7	30:34:51.4	11.±0.8	7.6±0.8	9.0±0.9	0.30±0.06
13	1:34:17.3	30:33:43.4	7.6±0.8	6.8±0.8	6.2±0.8	0.09±0.07
14	1:34:38.9	30:43:59.7	7.6±0.8	5.9±1.7	6.2±0.8	0.21±0.13

[2] These coordinates are accurate to approximately the half beam width of $\approx 3 - 4''$.

5.3 Results

5.3.1 Detection of UDH II Candidates

Our primary tool for distinguishing UDH IIs from other types of radio sources, such as supernovae remnants (SNR), is the radio spectral index α (where $S_\nu \propto \nu^\alpha$). While optically thin sources have $\alpha = -0.1$, optically thick sources have $\alpha > -0.1$ (α approaches 2 in the black body limit), and typical non-thermal objects have $\alpha < -0.4$. Unfortunately, not all SNRs obey this convention — as discussed in Chapter 4, there is a class of "plerionic" SNRs known to have atypically flat spectral indices ($-0.3 < \alpha < 0.0$). A second set of observations taken with adequate time separation, such as those employed in Chapter 4, would by useful determining possible variations in flux, which might be attributable to SNe.

Consequently, in order to select UDH II candidates from the radio data, I have applied the condition that these sources must have radio spectral indices $\alpha > 0$ (higher fluxes at shorter wavelengths). This criterion should exclude most other classes of radio-emitting objects, but it may also exclude genuine UDH II regions depending upon the exact instrumental angular resolution and frequencies observed. For example, low-frequency observations of optically thick thermal sources could be contaminated by steep-spectrum non-thermal sources, such as SNRs, and thus fail the $\alpha > 0$ test, especially at longer wavelengths. Furthermore, more distant sources, or sources observed using beam sizes larger than the thermal emitting region, may be contaminated by steep-spectrum, non-thermal background emission that dominates the disks and halos of most galaxies. Both of these effects will act to disguise an optically thick thermal bremsstrahlung signature. Thermal sources with the lowest emission measure, and thus the lowest free-free optical depth will be disguised the most strongly. Sources with the highest emission measures are more likely to maintain a positive spectral signature and be correctly identified. Fortunately, it is precisely these sources with high emission measures that are most likely to host ultra-young stellar clusters.

---

[1] Distances as high as 10.1 Mpc have been estimated (e.g., Sandage & Tammann 1981).

Table 5.2: UDH II candidates in NGC 253

#	R.A. (2000)	Dec. (2000)	$L_{1.3}$ $\times 10^{24}$ erg/s/Hz	$L_{3.6}$ $\times 10^{24}$ erg/s/Hz	Q_{Lyc} $\times 10^{49}$ 10^{49} s^{-1}	$\alpha_{1.3}^{3.6}$
1	0:47:32.75	-25:17:20.94	6.3±1.3	5.±0.5	60±13	0.19±0.10
2	0:47:32.85	-25:17:20.34	33.6±6.7	20.5±2.0	319±66	0.41±0.10
3	0:47:33.05	-25:17:18.25	59.1±11.8	49.0±4.9	561±120	0.15±0.10
4	0:47:33.05	-25:17:17.65	20.6±4.1	18.1±1.8	196±41	0.11±0.10
5	0:47:33.25	-25:17:15.55	50.4±10.1	29.7±3.	479±100	0.43±0.10

[3] These coordinates are accurate to approximately the half beam width of $\approx 0.1 - 0.2''$.

Because we are relying on relative fluxes at different frequencies to identify UDH IIs, it is critical that we understand the impact of beam sizes on these flux measurements. In some cases (as for NGC 6946), the multifrequency observations were done in different array configurations to match beam sizes at different frequencies. However, in some observations presented here the beam sizes are not well matched (as for M33). In these cases, typically a single configuration is used for all frequencies causing the beam size at the higher frequency to be smaller than the beam size at lower frequency. If the object (UDH II) is point-like with respect to the beams, the larger (lower frequency) beam will contain more non-thermal background contribution (as discussed above), which can only cause these objects to appear *less* thermal. If the object is extended, the lower frequency beam will contain more flux from the same physical environment than the higher frequency beam — again, artificially boosting the relative flux at the lower frequency, and also causing the object to appear *less* thermal. In other words, if the beam size at lower frequencies is larger than the beam size at higher frequencies (as is the case for the mismatched beams in this chapter), it will only disguise the optically thick signature of UDH IIs and *not* artificially imitate an optically thick thermal spectral index.

The condition that UDH II candidates must have positive spectral indices has resulted in the detection of fourteen sources in M33, five sources in NGC 253, and sixteen sources in NGC 6946. These sources are listed in Tables 5.1 – 5.3 along with their spectral indices (α, where $S_\nu \propto \nu^\alpha$). Within the uncertainties, eight of these objects are not inconsistent with

Table 5.3: UDH II candidates in NGC 6946

#	R.A. (2000)	Dec. (2000)	L_6 $\times10^{24}$ erg/s/Hz	L_{20} $\times10^{24}$ erg/s/Hz	Q_{Lyc} $\times10^{49}$ s^{-1}	α_6^{20}
1	20:34:19.79	60:10:06.46	11.3±1.9	10.4±1.3	92.7±16	0.07±0.09
2	20:34:22.58	60:10:34.12	43.6±1.9	33.9±2.2	358.0±26	0.21±0.03
3	20:34:32.35	60:10:12.48	3.8±0.9	1.3±0.9*	30.9±7.9	0.88±0.32
4	20:34:33.89	60:11:25.07	4.7±1.3	3.8±0.9	38.6±11	0.17±0.16
5	20:34:39.70	60:08:22.79	6.0±0.6	1.9±0.6*	49.05±.8	0.94±0.14
6	20:34:49.38	60:08:00.64	4.1±0.6	3.1±0.9	33.5±5.5	0.23±0.14
7	20:34:54.25	60:08:53.62	5.6±1.3	5.3±0.9	46.3±11	0.05±0.13
8	20:34:54.52	60:07:39.73	8.8±0.9	8.2±0.9	72.1±8.7	0.06±0.07
9	20:34:56.49	60:08:20.25	2.5±0.6	1.9±0.9*	20.6±5.3	0.23±0.23
10	20:35:03.67	60:10:59.66	3.4±0.9	3.1±1.3	28.3±7.9	0.08±0.22
11	20:35:04.35	60:09:46.09	3.8±1.3	2.2±1.3*	30.9±10	0.45±0.30
12	20:35:05.08	60:10:57.44	1.3±0.9*	0.9±0.6*	10.3±7.7	0.30±0.42
13	20:35:13.95	60:08:52.14	6.6±1.3	4.1±0.9	54.0±11	0.39±0.13
14	20:35:18.06	60:09:06.17	10.4±1.3	6.6±1.9	85.3±11	0.37±0.14
15	20:35:22.09	60:07:22.90	5.3±1.3	3.80±.9	43.8±11	0.27±0.15
16	20:35:24.12	60:08:42.61	3.8±0.9	2.2±0.6*	30.9±7.9	0.45±0.15

[4] These coordinates are accurate to approximately the half beam width of $\approx 1''$. [5] * These luminosities represent less than a 4σ detection.

having $\alpha \lesssim 0$, and I cannot rule out an optically thin H II region as the source. The remaining twenty-seven objects are only consistent with having an optically thick origin, and I consider these sources to be strong candidates for having an UCH II-like origin. Ulvestad & Antonucci (1997) have previously discussed the brightest of these five sources in NGC 253 (source #3 in this paper). Their derived properties ($Q_{Lyc} = 5.2 \times 10^{51}$ s^{-1}, size $= 2.4 \times 1.2$ pc, $EM = 2 \times 10^{8}$ cm^{-6} pc, and $n_e = 1.3 \times 10^{4}$ cm^{-3}) are in excellent agreement with the values I derive for this object in this section. However, the properties of the other four sources were not discussed, and I wish to add these sources to the current sample of UDH IIs available in the literature.

5.3.2 Comparison to Optical Images

As the gas and dust associated with UDH IIs dissipates and the extinction lessens, these objects will become more easily visible in optical light. On the other hand, UDH IIs will become less obvious in radio observations as their ambient densities decrease and their thermal bremsstrahlung emission decreases as a result. *Consequently, optical surveys of H* II *regions will be biased against detecting the youngest H* II *regions and radio surveys will tend to miss the older H* II *regions.*

Therefore, in order to understand how these UDH II candidates are related to star formation, past or present, it is useful to examine optical images near the source positions. In most cases, this comparison reveals whether the UDH II regions are associated with star formation visible in optical light, diffuse H II emission, or are completely obscured in this wavelength regime. In making such comparisons in crowded fields, we must keep in mind that the radio positions are no better than about half a beam width, e.g., $3 - 4''$ in M33, $1''$ in NGC 6946, and sub-arcsecond in NGC 253. To make these comparisons, I have tied the coordinate system of the optical images to the *HST* Guide Star "system." This leads to small internal errors ($0''.3$ RMS) within a galaxy, but it is well known that the same star will have coordinates that may differ by $2''$ or more from plate to plate in the Guide Star Catalog. We thus expect systematic

Table 5.4: Comparison with optical images of M33

Source #	B-band Counterpart?	H II Counterpart?	GDKG #
1	point source offset?	HBW 193 ?	15
2	diffuse, point source offset?	BCLMP 638	33
3	diffuse, point source	BCLMP 623	34
4	no	BCLMP 611 ?	67
5	diffuse emission	BCLMP 35/36	71
6	diffuse emission	BCLMP 39/40	82
7	no, dust lane?	BCLMP 43 ?	91
8	diffuse emission	BCLMP 703 ?	128
9	no, dust lane?	Z 171/179	129
10	diffuse emission offset?	BCLMP 87	137
11	point source	BCLMP 77	142
12	point source offset?	BCLMP 714	151
13	diffuse emission	BCLMP 712	161
14	complex source	BCLMP 749/750	178

[6] HBW refers to the Hodge et al. (1999) catalog. [7] BCLMP refers to the Boulesteix et al. (1974) catalog. [8] Z refers to the Courtés et al. (1987) catalog.

Table 5.5: Comparison with optical images of NGC 253

Source #	I-band Counterpart?	Hα Counterpart?	UV #
1	complex source	complex source	5.45-42.8
2	complex source	complex source	5.54-42.2
3	complex source?	diffuse emission?	5.72-40.1
4	complex source?	diffuse emission?	5.73-39.5
5	diffuse emission?	diffuse emission	5.90-37.4

[9] UV # refers to the reference number in Ulvestad & Antonucci (1997).

offsets between the optical and radio positions by as much as $3''$. This is possibly an overestimate, but I cannot rule out the physical correspondence of optical and radio sources within the astrometric uncertainty.

The locations of the UDH II regions in M33 were compared with B-band images from the 0.9 meter telescope on Kitt Peak; see Massey et al. (1996) for a complete description of the observations. I also searched the catalogs of H II regions in M33 given by Boulesteix et al. (1974), Courtes et al. (1987), Hodge et al. (1999). M33 is rich in H II regions, and all of the UDH IIs are possibly associated with previously known H II regions, although in some cases the connection is insecure (Table 5.4). However, only about half of the UDH IIs appear to be associated with stellar light apparent in the B-band image. The locations of the detected UDH IIs with respect to the B-band image are shown in Figure 5.1.

The radio observations of NGC 253 were compared to archival F656N (narrow-band Hα) and F814W (I-band) Hubble Space Telescope images (Figure 5.2). While there is diffuse emission in the vicinity of all five UDH IIs in this galaxy, only one of them (source #2) is clearly identified with a compact optical object. These results are presented in Table 5.5.

For NGC 6946, I compare the locations of the thermal radio sources with optical R-band and Hα images previously published by Larsen & Richtler (1999) (Figure 5.3). However, because of the large angular size of the galaxy ($\sim 10' \times 10'$) this image does not have a wide enough field to contain all of the radio sources. Therefore, I also use images from the the STScI Digitized Sky Survey [10] for comparison in these cases (Figure 5.4). About half of the sources in NGC 6946 have possible optical counterparts or diffuse emission, and the remaining half have neither.

While the sources for which there are no obvious optical counterparts must be deeply enshrouded (although it is not possible to rule out screens of dust not physically associated with the region of optically thick radio emission), and therefore are likely to be extremely young, it

---

[10] The compressed files of the Space Telescope Science Institute Quick-Survey of the northern sky are based on scans of plates obtained by the Palomar Observatory using the Oschin Schmidt Telescope.

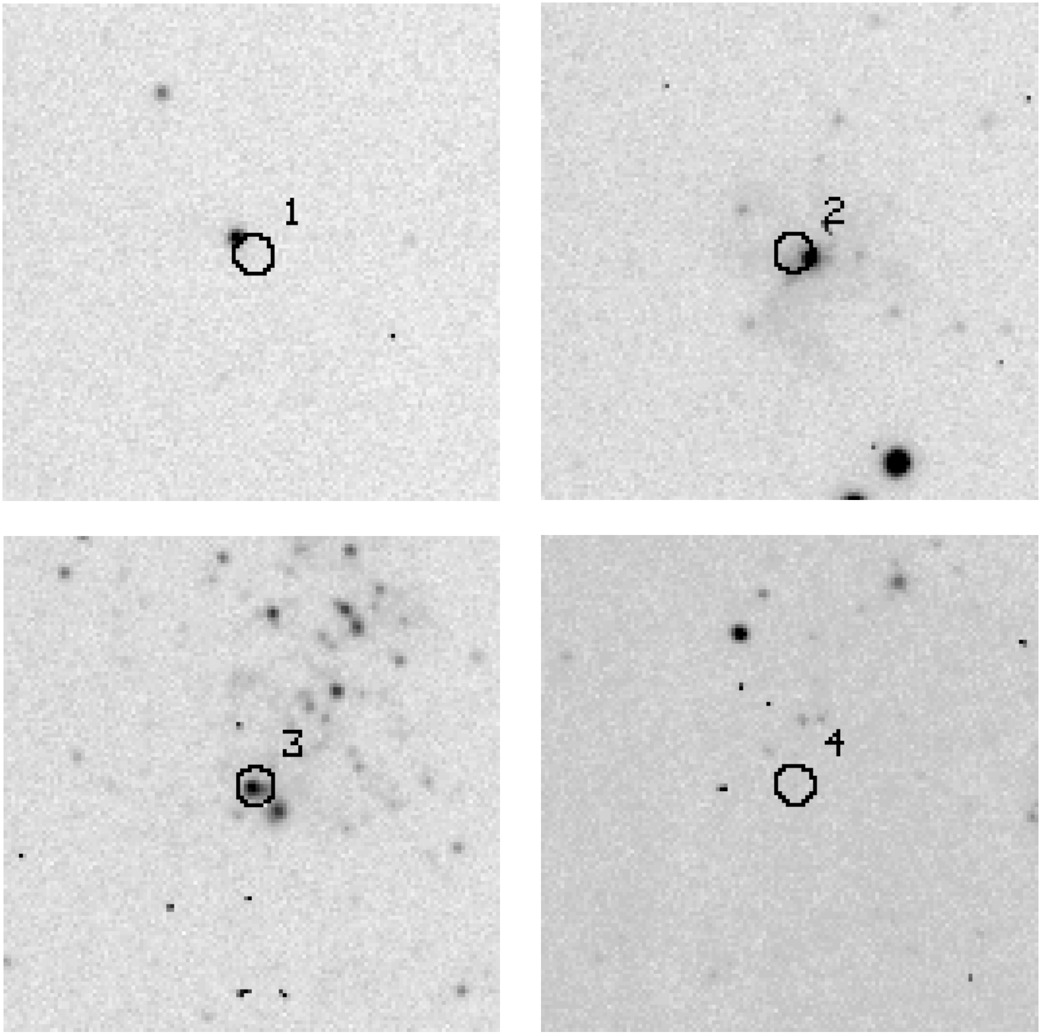

Figure 5.1: Locations of the detected UDH IIs in M33 are shown (along with their number in Table 5.1) with respect to the B-band images (shown in gray scale). The identification circles are $\sim 7''$ in diameter, reflecting the beam size of the radio observations. North is up and East is left. These images are all approximately $1'.5$ on a side.

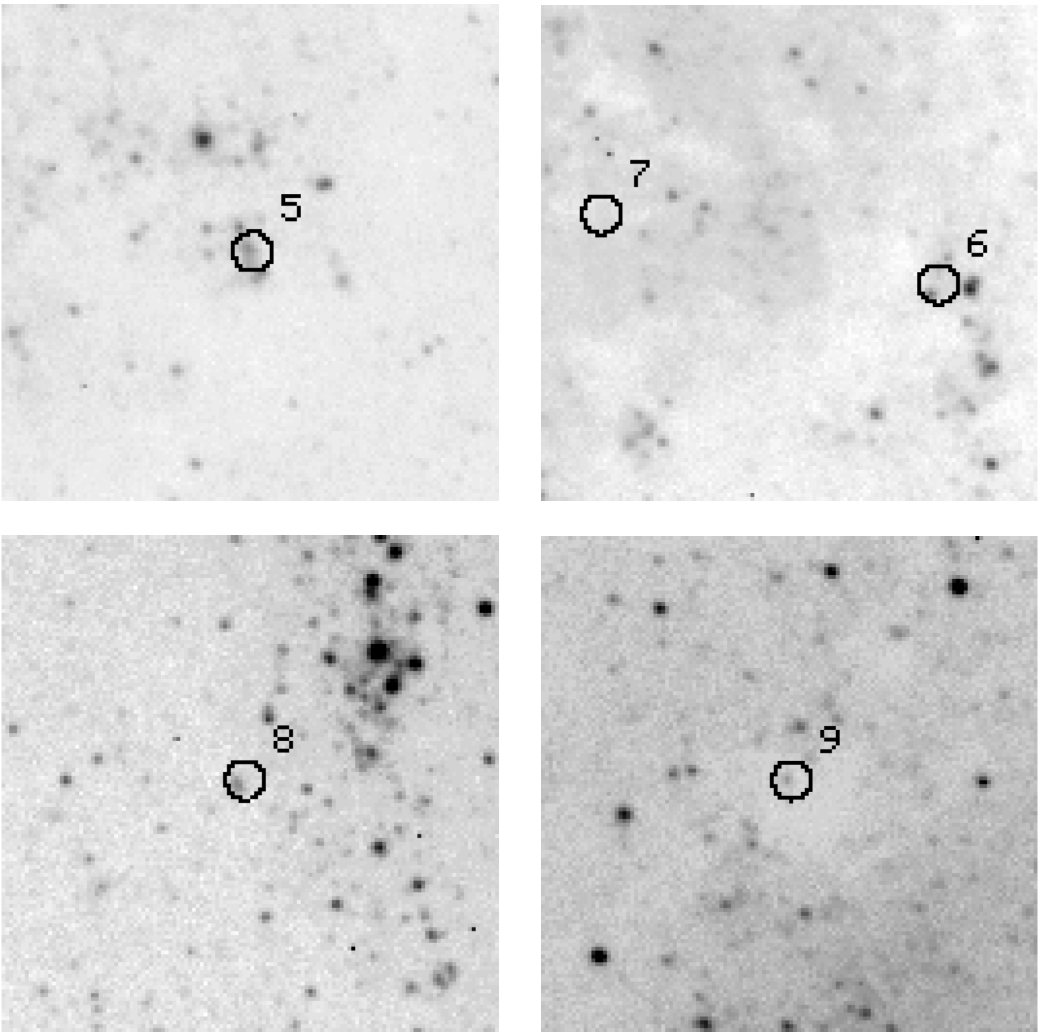

Figure 5.1 continued.

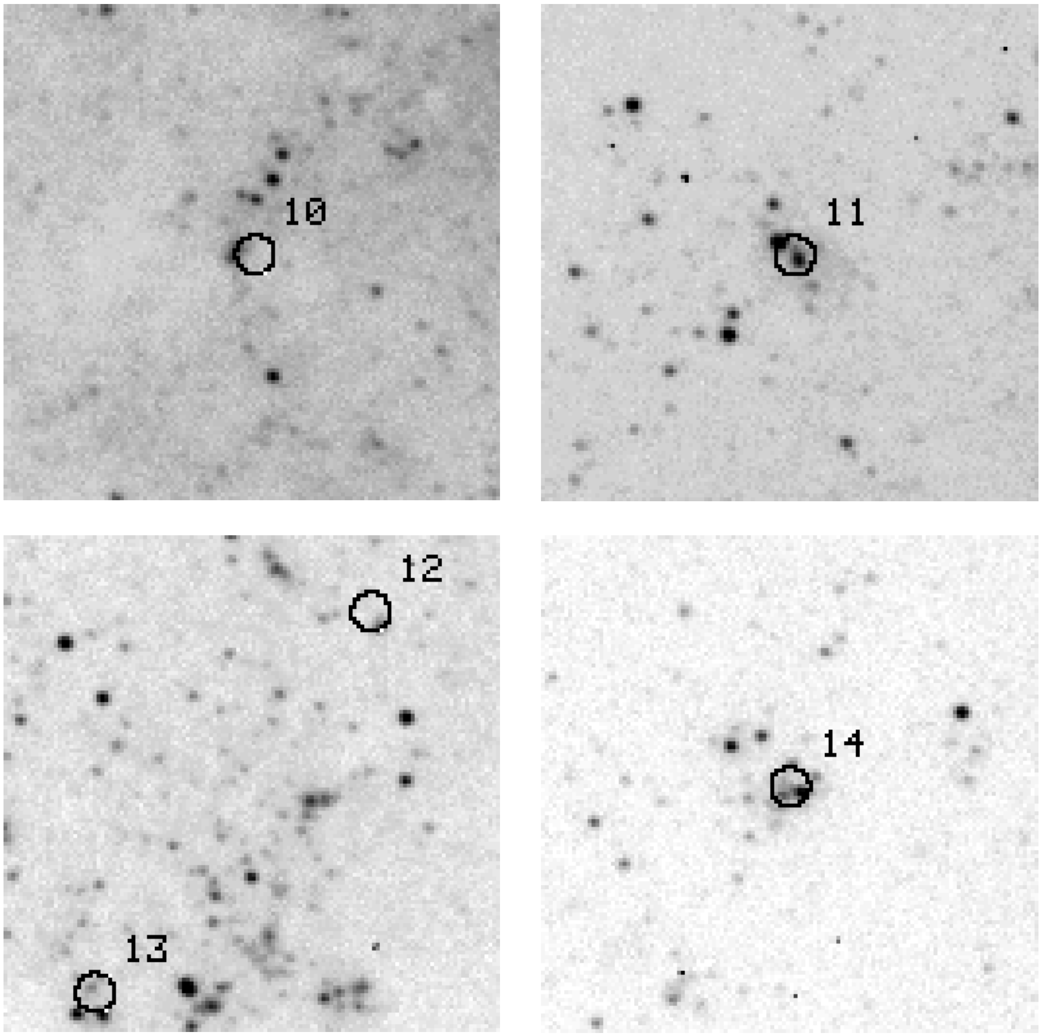

Figure 5.1 continued.

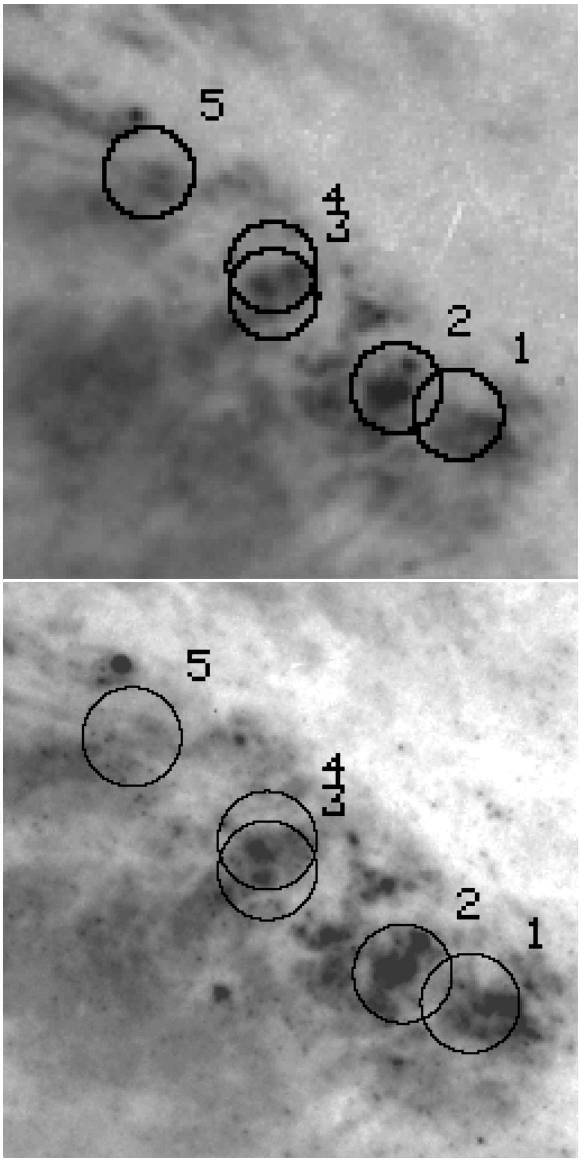

Figure 5.2: Locations of the detected UDH IIs in NGC 253 are shown (along with their number in Table 5.2) with respect to the Hα image (top) and I-band image (bottom). The identification circles are $\sim 2''$ in diameter, reflecting the astrometric precision of *HST*. North is up and East is left. The Hα image is approximately $12''.7 \times 12''.7$, and the I-band image is approximately $11''.6 \times 11''.6$.

Table 5.6: Comparison with optical images of NGC 6946

Source #	R-band Counterpart?	Hα Counterpart?	LDG #
1	diffuse emission	—	3
2	no	—	5
3	diffuse emission	faint source?	10
4	diffuse emission	diffuse emission	11
5	no	no	24
6	point source	point source	42
7	no	no	73
8	complex source	complex source	76
9	no	no	79
10	no	no	87
11	no	no	90
12	diffuse emission	diffuse emission	94
13	diffuse emission	diffuse emission	109
14	diffuse emission	—	111
15	no	—	113
16	no	—	116

[11] LDG # refers to the reference number in Lacey et al. (1997).

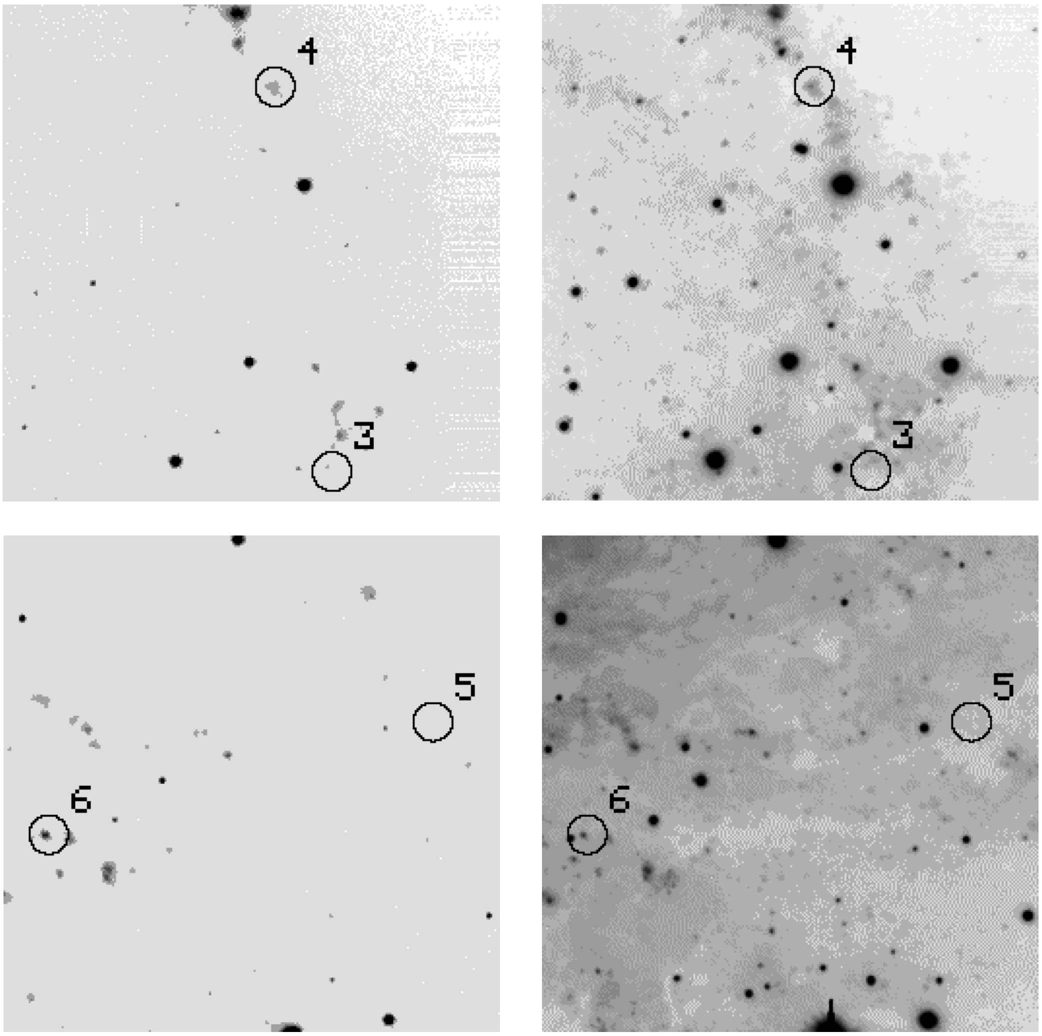

Figure 5.3: Locations of the detected UDH IIs candidates #3–12 in NGC 6946 are shown (along with their number in Table 5.3) with respect to the Hα (left) and R-band (right) images of Larsen & Richtler (1999). The identification circles are $\sim 3''$ in radius, reflecting the relative astrometric uncertainty. North is up and East is left. These images are approximately $1'.6 \times 1'.6$.

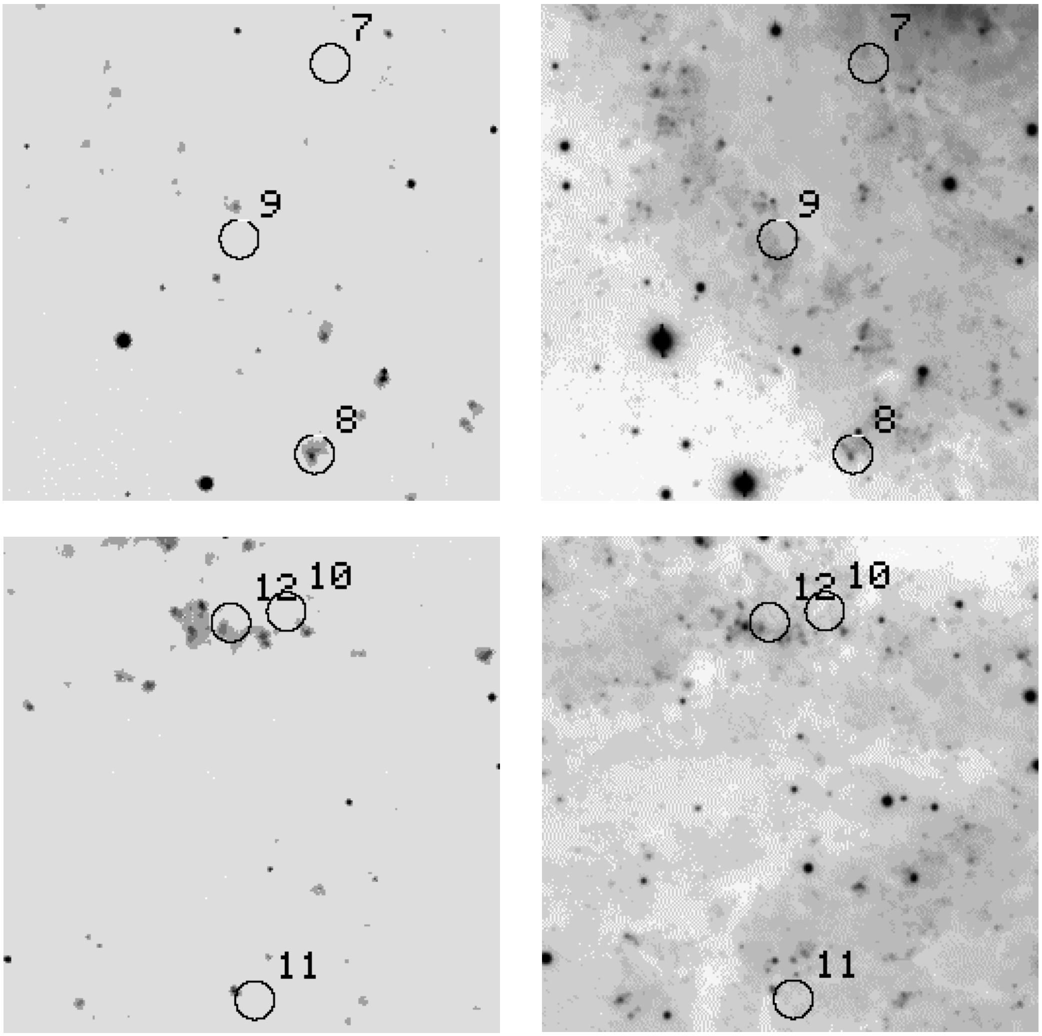

Figure 5.3 continued.

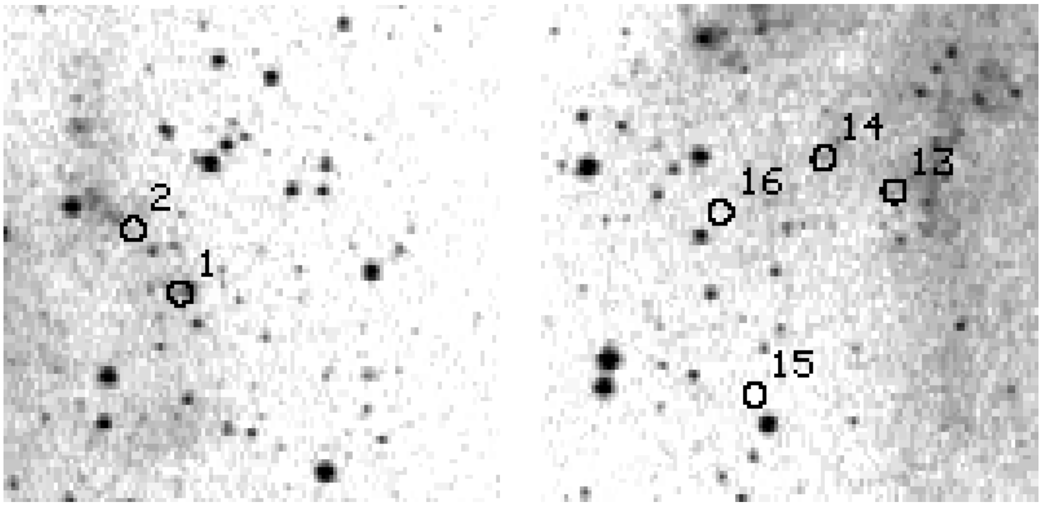

Figure 5.4: Locations of the detected UDH IIs are shown (along with their number in Table 5.3) with respect to the Digitized Sky Survey (sources 1–2 and 13–16). The identification circles are $\sim 3''$ in radius, reflecting the relative astrometric uncertainty. North is up and East is left. These Digitized Sky Survey images are approximately $3'.6 \times 3'.6$.

is not clear whether detection of light in the optical regime rules out extreme youth for UDH II regions. I make this tentative statement for several reasons: (1) in most cases presented in this sample, the identification of an optical counterpart is insecure due to the possible systematics between the optical and radio positions, as well as the relatively large synthesized radio beamwidth for M33; (2) in cases where individual stars are resolved (M33), the *number* of stars required to create the Lyman continuum flux are not apparent in the optical images, suggesting either a misidentification due to pointing uncertainty, or a number of the individual stars are, in fact, still enshrouded. This scenario has actually been observed in the galactic UCH II complex W49A where *some* of the stars in the complex appear to have emerged from their birth cocoons while the rest of the complex remains enshrouded (Conti & Blum 2001) ; and (3) if the dominant source of opacity is Thomson scattering (and not dust), a source with a radius of 5 pc could have electron densities as high as $n_e = 10^5$ cm^{-3} and still have opacities as low as $\tau \sim 1$ (although it is difficult to imagine how newly formed stars could be in an environment absent of dust).

Therefore, I conclude that the possible identification of optical counterparts does not preclude the youth of these objects. However, the sources for which there are no optical counterparts are more likely deeply embedded in their natal molecular clouds, and therefore are more likely to be extremely young.

5.3.3 Modeled Properties

Given the luminosities and radio spectral energy distributions of H II regions, their physical parameters such as size and electron density can be estimated. Again using the analytical approximation of Mezger & Henderson (1967) (as in Chapter 4), I can estimate the emission measure, $EM = \int n_e^2 dl$, given an electron temperature, T, the observing frequency, ν, and the optical depth at that frequency.

$$EM(\mathrm{cm}^{-6}\ \mathrm{pc}) = 12.2 \left[\frac{T_e}{(\mathrm{K})}\right]^{1.35} \left[\frac{\nu}{(\mathrm{GHz})}\right]^{2.1} \tau. \tag{5.1}$$

The positive spectral index for these sources arises from free-free emission where $\tau \gtrsim 1$,

Table 5.7: Estimated emission measures

$\lambda(cm)$	EM(cm^{-6} pc)×10^8
1.3	16 ± 3
2	7 ± 1
3.6	2 ± 0.3
6	0.7 ± 0.1
20	0.05 ± 0.01

therefore we assume $\tau = 1$ as a lower limit. The electron temperature of Galactic UCH IIs is typically $T_e = 8000 \pm 1000$ K (e.g., Afflerbach et al. 1996), which I adopt for this estimate. The resulting emission measures for each of the wavelengths used in this sample range from $\sim 0.05 - 16 \times 10^8$ cm^{-6} pc as in Table 5.7 (for $\tau > 1$ these emission measures will be correspondingly higher). Although the radio maps constrain the size of the emitting region only weakly [12] , it is clear that electron densities in excess of 1000 cm^{-3} are required to produce the observed emission measures. For comparison, typical giant H II regions observed optically have electron densities ≈ 10^2 cm^{-3} (Kennicutt 1984).

In order to better constrain the properties of these UDH II regions, following Chapter 4, I have modeled H II regions as homogeneous spheres of plasma with uniform electron density and temperatures of 8000 K. Only free-free emission and absorption processes are considered. Varying the radius, R, and electron density, n_e, I modeled the radio spectral energy distribution resulting from thermal bremsstrahlung emission and self-absorption. These results are illustrated in Figures 5.5-5.7 along with the data from Tables 1–3.

Figure 5.5 shows the 20 cm and 6 cm observations of UDH II regions in M33 along with the best fit model H II regions spectral energy distributions. Each object from Table 5.4 is shown in a separate panel. Solid lines show H II region models with electron densities in the range of $n_e \approx 1000 - 3000$ cm^{-3} and radii in the range of 0.5 pc and 2.3 pc. Figure 5.6 illustrates that electron densities between 11,000 cm^{-3} and 22,000 cm^{-3} are required to fit the data, while

---

[12] The radio maps constrain the sizes of the emitting regions to diameters ≤ 4 pc in the case of NGC 253, ≤ 28 pc in the case of M 33, and < 50 pc in the case of NGC 6946

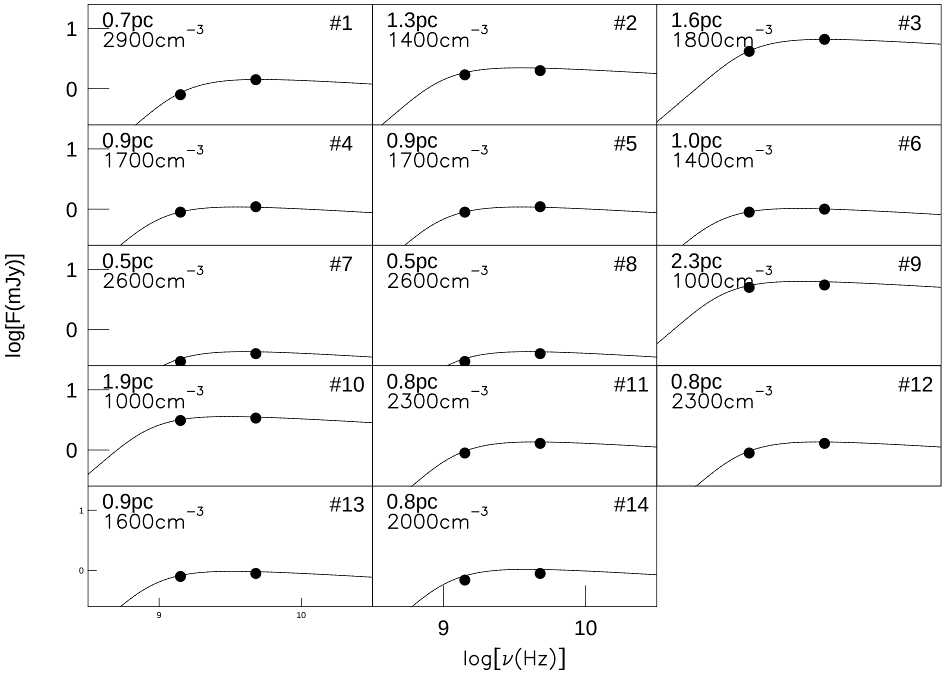

Figure 5.5: The radio fluxes and luminosities for the UDH IIs candidates in M33 from Table 5.1. The radio data are consistent with model H II regions having electron densities $n_e = 1700 - 3000$ cm^{-3} and radii $\sim 1 - 2$ pc.

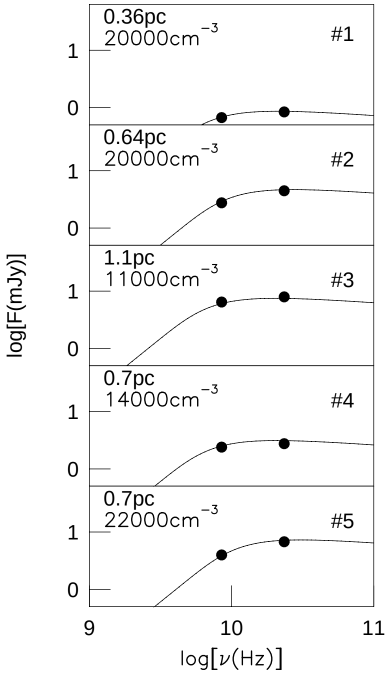

Figure 5.6: The radio fluxes and luminosities for the UDH IIs candidates in NGC 253. The data are consistent with model H II regions having electron densities $n_e = 11,000 - 22,000$ cm^{-3} and radii $\sim 0.3 - 1$ pc.

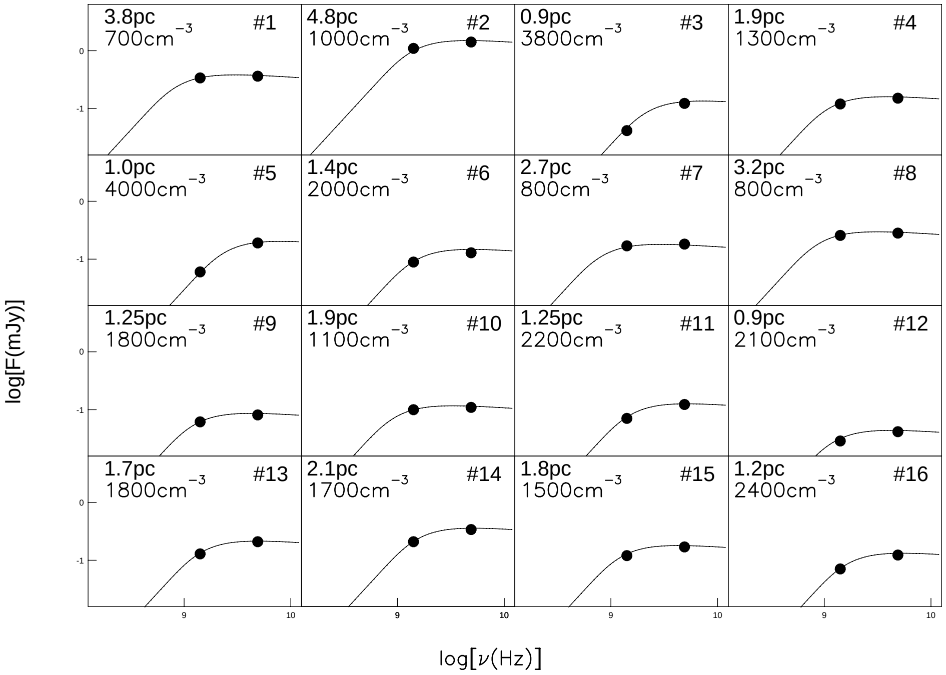

Figure 5.7: The radio fluxes and luminosities for the UDH IIs candidates in NGC 6946 in Table 5.3. The data are consistent with model H II regions having electron densities $n_e \approx 1000 - 5000$ cm^{-3} and radii $R = 1 - 4$ pc.

the best fit radii are all $\lesssim$ 1 pc. Not only are the UDH II regions in NGC 253 intrinsically more luminous than in the other two galaxies, they also have higher densities. In the case of NGC 253, observations reveal that the UDH II regions are optically thick at frequencies as high as 15 GHz. In the case of NGC 6946, densities of 700 cm^{-3} to 4000 cm^{-3} fit the 20 cm and 6 cm data for radii ranging from $\sim$ 1 pc to 5 pc.

It is reasonable to ask whether the simple homogeneous sphere models presented here are sufficient to infer the physical characteristics (sizes, densities) of the UDH IIs. Realistically, we expect that the radio sources identified as UDH IIs are not simply monolithic dense H II regions. Rather, we might expect that they are collections of several hundred ultra-compact H II regions ($n_e = 10^5$ cm^{-3}, $R = 0.1$ pc) embedded in a more tenuous inter-UCH II medium (see § 5.4.2). However, NGC 5253 (Turner et al. 2000) is near enough and have observations with high enough resolution that the radio imaging can directly constrain the sizes of the emitting regions without recourse to model assumptions. In this case, the simple homogeneous spherical models described above produce size estimates in excellent agreement with the high-resolution radio maps. The deconvolved diameters of the radio the single UDH II radio source in NGC 5253 has a deconvolved diameter of ~ 2 pc (Turner et al. 2000), consistent with the expectations of the simple model predictions based on their observed radio luminosities. As further support for our simple models, recently Mohan et al. (2001) have made slightly more sophisticated multi-density models for radio recombination line observations of He 2-10 and and NGC 5253; their results are in excellent agreement with the results obtained with these simple models.

Given the agreement in this cases, I believe that the simple two-parameter models are sufficiently instructive to make meaningful inferences about the sizes and densities of UDH IIs based on radio continuum luminosities. More realistic models would include an arbitrary number of UCH II regions within each UDH II each with its own density profile, and an inter-UCH II medium with a specified density profile and temperature distribution. However, relaxing the simple two-parameter approach results in the number of free parameters and computational complexity growing rapidly.

5.4 Discussion

5.4.1 Stellar Content

The production rate of Lyman continuum photons, and, thus, the stellar content of each UDH II region can be estimated from the thermal radio luminosity following Condon (1992) as in Chapter 4,

$$Q_{Lyc} \geq 6.3 \times 10^{52}\ \mathrm{s}^{-1} \left(\frac{T_e}{10^4\mathrm{K}}\right)^{-0.45} \left(\frac{\nu}{\mathrm{GHz}}\right)^{0.1} \left(\frac{L_{thermal}}{10^{27}\mathrm{erg\ s^{-1}Hz^{-1}}}\right). \tag{5.2}$$

Since the non-thermal component becomes weaker at higher frequencies, for each of the UDH IIs in this sample we use the luminosity measured at the highest frequency in each data set to determine Q_{Lyc}. The resulting values determined from this method are presented in Tables 5.1 – 5.3. One should also bear in mind that the Q_{Lyc} values determined with this method could suffer from two different problems: (1) if the source is, in fact, optically thick even at the highest frequencies measured, this method will *underestimate* the actual ionizing luminosity, and (2) if there is contamination from background non-thermal emission in the beam at the frequency used, the ionizing luminosity will be *overestimated*. While these two issues have an opposite effect on Q_{Lyc}, we might expect the impact of (2) to be negligible as discussed in Chapter 4.

The production rate of Lyman continuum photons from these sources can be used to estimate the number of massive stars powering the observed emission. Following the convention of Vacca (1994), a "typical" O-star (type O7V) produces $Q_{Lyc} = 1.0 \times 10^{49}$ s^{-1}. Therefore, the Q_{Lyc} values in Tables 5.1-5.3 can be directly translated into the number of "equivalent" O7V stars (O7V*). Using this method, we see that the UDH II regions in this sample have $\approx 3 - 46$ O7V* stars in M33, $\approx 60 - 560$ in NGC 253, and $\approx 10 - 360$ in NGC 6946. Moreover, the *total* stellar mass of these objects can be estimated using the Starburst99 models of Leitherer et al. (1999) with solar metallicity, Salpeter IMF, and lower and upper mass cutoffs of 1 M$_\odot$ and 100 M$_\odot$, respectively (decreasing the lower mass limit will increase the total stellar mass estimate). Using these parameters, star clusters producing this range of Lyman continuum photons at ages $\sim 0 - 5$ Myr would have total masses of $\sim 100 - 60000$ $M_\odot$.

These Q_{Lyc} and mass values are smaller than those found for the UDH IIs in He 2-10 and in NGC 5253 (Turner et al. 2000), which have > 750 O7V* stars and masses $> 10^5$ $M_\odot$. This is not a surprising result — it is likely that we will only find massive star clusters forming in intense starburst events; Elmegreen & Efremov (1997) have demonstrated the need for extremely high-pressure environments, such as those found in starburst galaxies, to produce bound massive star clusters. However, in less formidable environments, we should expect to find a continuous range of UDH IIs — from single UCH IIs and UCH II complexes (such as those found in the Galaxy), to the massive bound clusters (such as those found in NGC 5253, He 2-10, and NGC 2146) that may evolve into globular clusters. The sample presented in this chapter is beginning to fill in this continuum of objects for the first time.

5.4.2 Comparison to W49A

One of the most well studied UCH II complexes in the Galaxy is W49A, which makes it well suited for comparison to the UDH II regions in this sample. First detected by Westerhout (1958) in his radio survey, W49A has since been resolved into at least 30 UCH II regions (de Pree et al. 1997), and is estimated to have ~ 100 O7V* stars (Smith et al. 1978; Vacca 1994). It also appears that a few of the stars in W49A have begun to emerge from their birth cocoons while the rest of the cluster remains deeply enshrouded (Conti & Blum 2001). W49A is ~ 13 pc in diameter (de Pree et al. 1997), and would fit within the beam sizes utilized in this chapter if located at the same distances as the galaxies in this sample; W49A would have angular sizes of $\sim 2''.9$, $1''.2$, and $0''.6$, respectively, in M33, NGC 253, and NGC 6946. Because W49A is significantly closer ($D = 11.4$ kpc; Gwinn et al. 1992), than the galaxies presented in this paper, any observations I use for comparison need to be at sufficiently low resolution as to include the entire W49A region. This condition is well-satisfied by the pioneering observations of Mezger et al. (1967), who obtained $\sim 3 - 4'$ resolution radio maps of W49A at several wavelengths.

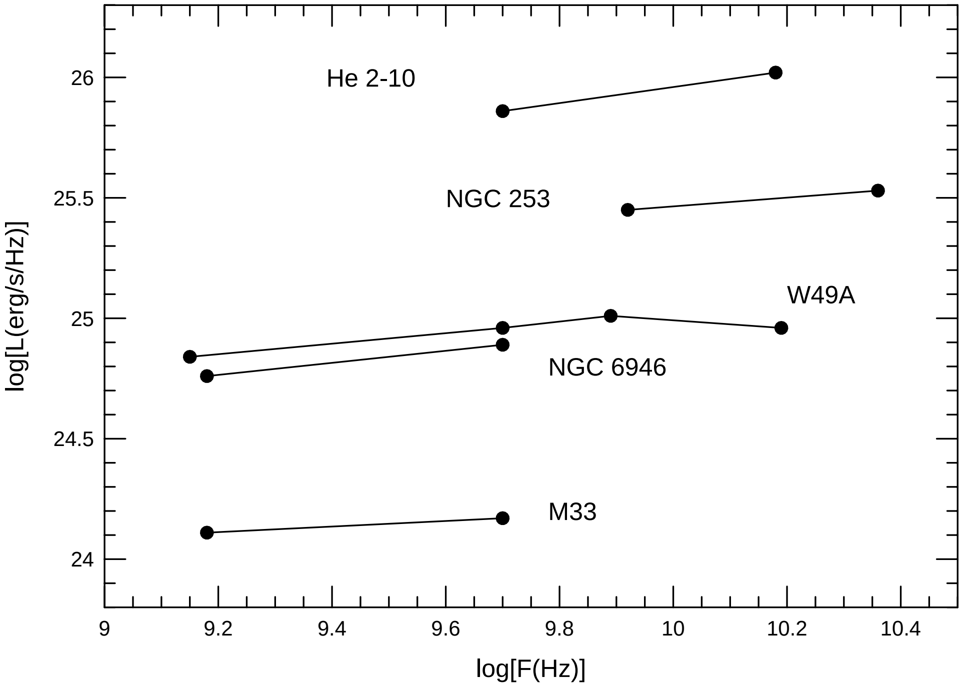

Figure 5.8: A comparison of the luminosity and spectral energy distribution of W49A from Mezger et al. (1967) and the *mean* luminosity of UDH II regions from M 33, NGC 253, and NGC 6946. The luminosity and spectral energy distribution of W49A is similar to the UDH II regions in each of the three galaxies in this study.

In Figure 5.8, I present the radio spectral energy distribution of W49A (Mezger et al. 1967) in comparison to the *mean* UDH II region from M33, NGC 253, and NGC 6946. It is clear that the integrated radio spectral energy distribution of W49A is almost identical to those of the UDH II regions in this sample. Figures 5.9 – 5.11 show histrograms of the 6 cm luminosities for the sources in M33 and NGC 6946 and the 3.6 cm luminosities (6 cm data is not included in this sample) for NGC 253 along with an arrow indicating the luminosity of W49A. Comparing the luminosity of W49A to those of the UDH II regions in M33, it is clear that W49A is up to 10 times *more* luminous than the M33 sources. In NGC 6946 W49A would be one of the more luminous H II regions. However, in the case of NGC 253, W49A would be one of the *least* luminous objects — a magnitude or more fainter than the most luminous UDH II regions detected in this galaxy.

The dotted line in Figure 5.9 illustrates the luminosity function of optically selected H II regions in M33 (Smith & Kennicutt 1989) who find $N(L)dL \propto L^{-2.3}dL$. This comparison shows that the luminosity function of UDH II regions is consistent with the normal H II region luminosity function, suggesting that the UDH IIs are simply a phase in the formation of many, perhaps most, H II regions. Furthermore, if the formation of massive star clusters is primarily related to the intensity of the star formation a galaxy is currently undergoing, it is not surprising that the UDH II regions in M33 and NGC 6946 are similar to the UCH II complexes in the Milky Way which has a similar star formation rate. NGC 253, by contrast, has a much higher star formation rate and it certainly contains a more intense starburst, which is also in accord with the more massive UDH II regions it hosts.

5.4.3 On the Youth of UDH II Regions

As in Chapter 4, we can estimate the typical lifetime of these UDH IIs. If star formation has been relatively continuous over the past 10 Myr, the lifetimes can be estimated using the fraction of ionizing stars in UDH II regions compared to the fraction of ionizing stars in conventional H II regions. For M33 and NGC 6946 the minimum implied total Lyman continuum

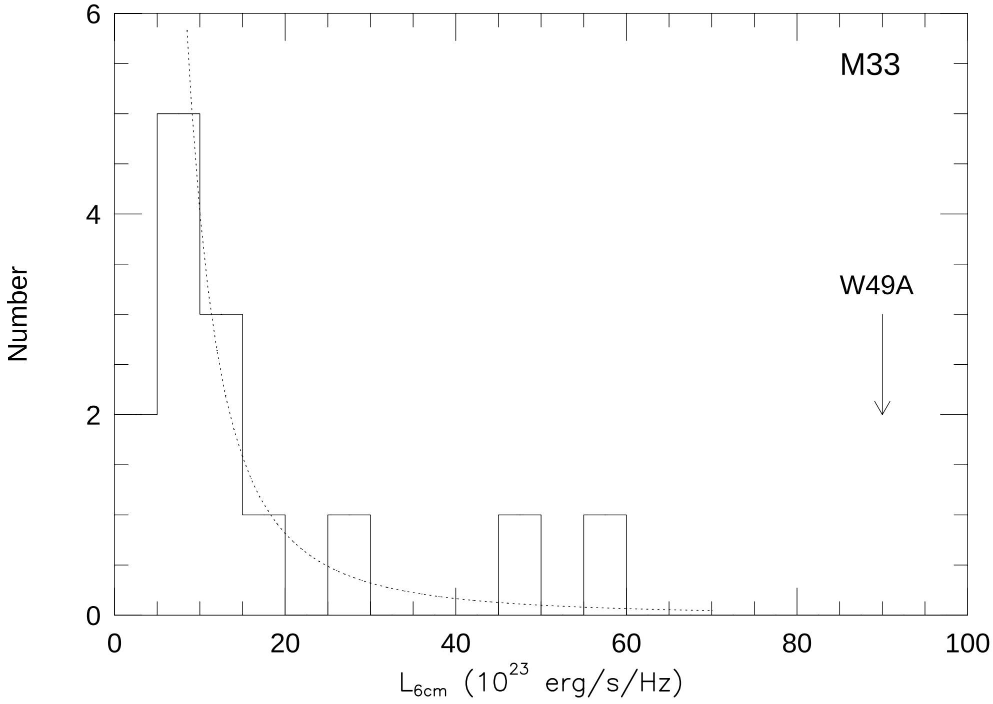

Figure 5.9: Histogram of luminosities for the UDH II candidates in M33. The arrow in the plot marks the luminosity of W49A. The dotted line in illustrates the luminosity function of *optically selected* H II regions in M33 from (Smith & Kennicutt 1989) that find $N(L)dL \propto L^{-2.3}dL$. The completeness limit is not well determined, but the 5σ noise level is $\approx 2{\times}10^{23}$ erg s^{-1} Hz^{-1}.

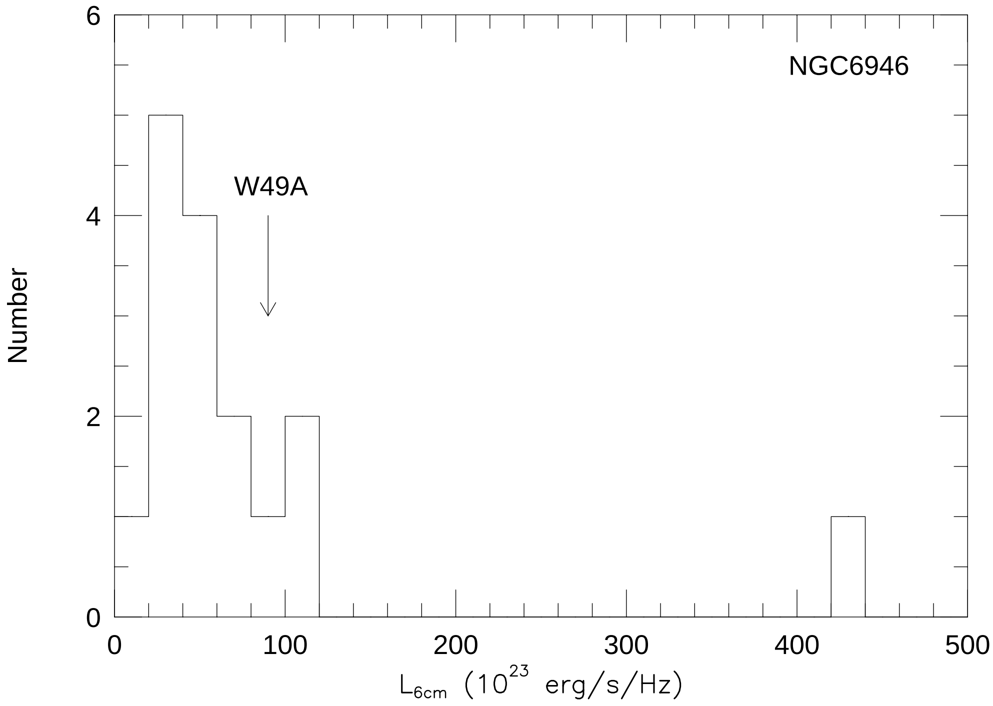

Figure 5.10: Histogram of luminosities for the UDH II candidates in NGC 6946. The arrow in the plot marks the luminosity of W49A.

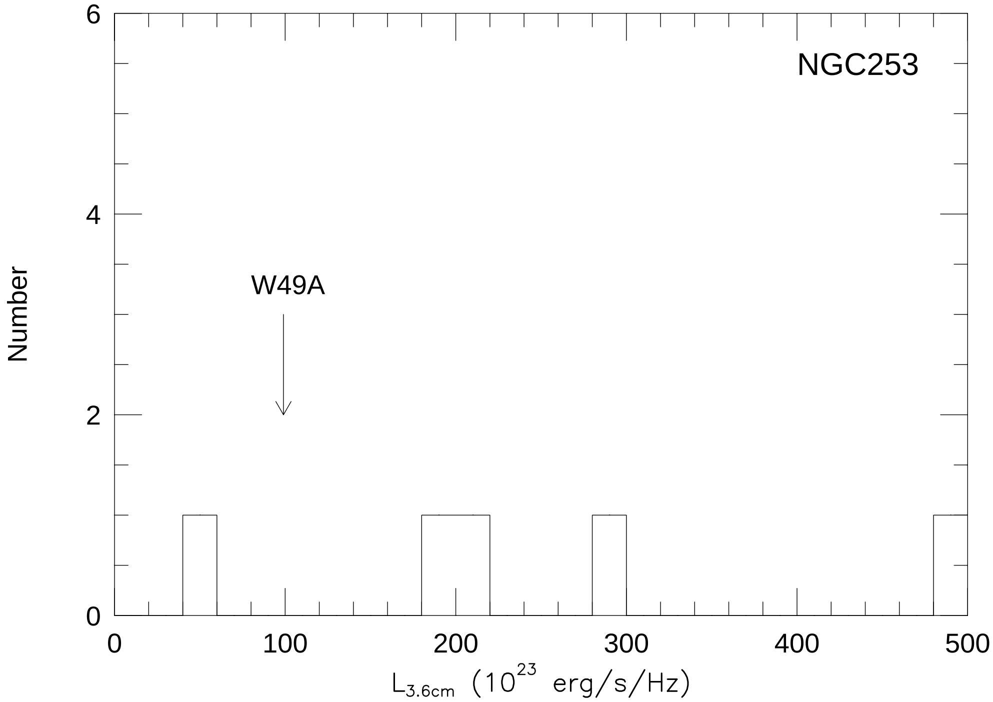

Figure 5.11: Histogram of luminosities for the UDH II candidates in NGC 253. The arrow in the plot marks the luminosity of W49A.

photon production rate, Q_{Lyc}, of the UDH II regions is 1.9×10^{51} s^{-1} and 10×10^{51} s^{-1} respectively (provided there is no leakage from the enshrouding cocoon that would likely result in associated Hα emission). The total Q_{Lyc} for the entire galaxy is 3×10^{53} s^{-1} for M33 and 1.5×10^{53} s^{-1} for NGC 6946 (Kennicutt 1983 scaled to our adopted distance). Thus, the UDH II regions contain 1% and 7% of the total ionizing photons. If the star formation has been reasonably continuous in these systems, a plausible estimate for the typical duration of the UDH II phase is 0.01 to 0.07 times the typical H II region lifetime ($\sim 10^7$ yr). This implies a mean age of less than 1 Myr for UDH II regions, in excellent agreement with the lifetimes estimated in Chapter 4.

Chapter 6

Future Work

The discovery of UDH II s has opened up a new field, allowing us to study the earliest stages of massive star cluster evolution for the first time as well as the influence this mode of star formation has had throughout the universe. As with any fledgling field, there is a great deal of knowledge and understanding yet to be worked out, and many questions remain. Future work will reveal the physical properties of these ultra-young massive star clusters and determine the conditions required for their formation. In addition to studying their earliest developmental stages, we will determine the properties of massive star clusters as they evolve and develop an evolutionary sequence. This work will have a direct impact on our understanding of both stellar and galactic evolution, as well as the origin of globular clusters and the physical conditions in the early universe required to create these massive clusters so prodigiously.

6.1 Expand the Sample of Known UDH IIs

Because UDH IIs have only recently been discovered, one of the most fundamental goals in this field is simply to expand the sample of known objects in order to better understand their properties in a statistical sense. For example, once we have obtained a large enough sample we will be able to construct an initial mass function for clusters and examine its dependence on different physical environments. This result will be absolutely crucial in understanding the physics of star formation via molecular cloud collapse.

High resolution radio telescopes, such as the Very Large Array (VLA), are ideally suited for conducting surveys of starburst galaxies at high radio frequencies (such as 5 and 20 GHz) in order to detect the characteristic optically-thick thermal spectral energy distribution of these compact sources. Because radio wavelengths do not suffer from dust extinction, we will be able to probe even the most dense and obscured star forming regions in starburst galaxies. To this end, I have already begun observing campaigns with the VLA, the Multi-Element Radio Linked Interferometer Network (MERLIN), and the Australia Telescope Compact Array (ATCA) with observations already made of eight additional Wolf-Rayet galaxies (MRK 8, MRK 33, NGC 3395, NGC 3396, IC 4662, NGC 5398, NGC 1705, and NGC 4449). In addition, I have begun a survey with ATCA (at 3 cm and 6 cm) of radio sources in the Magellanic Clouds in order to extend our knowledge of individual UCH II regions beyond the Galaxy.

6.2 Determine the Properties of the Birth Environments of Massive Star Clusters

One of my main objectives for the future is to determine the physical properties required to form massive bound clusters. We know that in the local universe, massive star clusters appear to be formed exclusively in starbursting regions of galaxies. However, we have never directly probed the environmental conditions of their formation. Similar physical conditions must have been present in the early universe in order to create the vast number of old globular clusters we see today (although metallicity is almost certainly an issue here, and studying the lowest metallicity systems available will be critical for this interpretation).

Because massive star clusters in their earliest stages are embedded in their natal molecular clouds, millimeter observations of molecular lines are particularly well suited for observing their birth environments. The highly abundant CO lines can be used to trace the molecular gas associated with UDH IIs, while higher dipole molecules, such as CS or HCN will map out the highest density gas which is expected to be directly correlated with areas of star formation. We can use molecular line diagnostics to provide information on all of the basic physical properties of the natal environments, including their temperatures, densities, and pressures.

I have already obtained two tracks with the OVRO millimeter array (with the equatorial and ultra-high resolution configurations; a track in the high configuration has not yet been observed although the time was granted) to create a high spatial resolution map of the CO(1-0) line in He 2-10, where we discovered five UDH IIs (see Chapter 4). I will also apply for time in the coming semester using the BIMA millimeter array for a project mapping the physical properties of the dense gas in the starburst galaxies known to host UDH IIs. In the more distant future, the proposed (and not quite funded to date) Atacama Large Millimeter Array (ALMA, to be built in the Atacama desert in Chile) will enable superb sub-arcsecond observations (similar to the resolution of HST) to be obtained in the millimeter regime for the first time. This instrument will be ideal for studying the physical properties of UDH IIs.

Another issue I wish to address is the relation between the morphology of warm/hot dust and the UDH IIs. UDH IIs should be embedded in knots of bright and hot dust emission. To date, only minimal mid-infrared data (such as that presented in Chapter 4) exists on UDH IIs, but this dust has not yet been observed in detail. I plan to carry out a mid-infrared imaging and spectroscopy campaign to directly measure the warm and hot dust associated with UDH IIs, allowing us to establish the nature of this relationship.

6.3 Determine the Properties of Massive Star Clusters at Different Evolutionary Stages

As massive star clusters age and begin to emerge from their birth material, their physical properties will evolve rapidly. For example, in the earliest stages of their evolution, their environment will transform from being optically thick to optically thin at radio wavelengths. As the most massive stars begin to evolve, they will dramatically affect the cluster environment via stellar winds and supernovae. After the ambient gas has been dissipated from the cluster, much of the gravitational binding energy is lost and the clusters themselves may begin to dissociate. Throughout these phases, the overall spectral energy distribution of these clusters will also metamorphose. However, since these clusters are only newly discovered, one of the large gaps in our knowledge is the nature of their spectral energy distribution and how it evolves.

There are a number of powerful techniques available in different wavelength regimes to study massive star clusters as they evolve from being completely enshrouded to being dominated by stellar light. For the youngest and most deeply enshrouded clusters, radio recombination lines provide a practical method for observing the spatial structure and physical properties of clusters. Because radio recombination lines do not suffer from the same dust obscuration as hydrogen recombination lines at shorter wavelengths (e.g., Hα, Hβ, etc.), they are naturally suited to observing the properties of the ionized gas in the youngest star forming regions. Over the past decade, the sensitivity of radio telescopes has greatly improved and radio recombination lines have been detected in a number of starburst galaxies (see Anantharamaiah et al. 2000, and references therein). Atomic lines in the mid-IR can also yield information about the properties of enshrouded clusters. Species such as [Ne II], [Ne III], [S III], [S IV], etc. can provide information about the number of ionizing photons (and therefore the number of massive stars), the temperatures, and ages of the clusters.

As UDH IIs become less enshrouded (and eventually completely transparent) to optical wavelengths, stellar light can begin to penetrate a moderate amount of extinction in the near-IR, where spectra are rich in diagnostic lines. In particular, the Paα, Brγ, He I, and [Fe III] lines are strong nebular diagnostics available in this wavelength regime. The installation of the new NICMOS cooling system (currently advertised as being available for cycle 11 with HST) will open up new possibilities for studying UDH IIs at high spatial resolution in the near-IR, particularly for diagnostic lines such as Paα which cannot be observed from the ground due to poor atmospheric transmission.

For diagnostic lines which can be observed through atmospheric windows, the new Gemini telescopes will provide superb defraction limited observations. In the near- to mid-infrared. In addition to the Gemini observations I have already obtained (Chapter 4), I have also been awarded time in the upcoming semester on Gemini South to obtain spectroscopy of the UDH IIs in He 2-10 in the thermal infrared window from 8 μm to 14 μm. These observations will allow us to measure the fine structure emission lines of [Ar III], [S IV], and [Ne II] in addition to establishing the presence or absence of the PAH features at 8.6 μm and 11.3 μm and checking for silicate absorption.

6.4 Identify an Evolutionary Sequence

It is becoming clear that we are seeing a *continuum* of sizes and luminosities for extragalactic massive star clusters in the earliest stages of their evolution. Recognition of the ubiquity of the UDH II phase of massive star formation pushes us one step closer to understanding the genesis mechanisms of all star clusters, from small associations to giant proto-globular clusters. Along with a continuum in sizes, we should also expect to find a continuous range of ages tracing an evolutionary sequence.

In addition to studying the physical conditions in UDH IIs, we can search for an *even earlier* stage of massive star birth in clusters which has not yet been identified; before stars have actually reached the main sequence and begun ionizing the surrounding ISM, they go through a “hot core” phase (see Figure 6.1). Massive star clusters should have an analogous phase, in which the regions will be defined by extremely dense and warm gas which is not associated with strong free-free emission. These sources may be observable for the first time by finding their dense molecular cores and/or associated mid- to far-infrared emission.

The Space Infrared Telescope Facility (SIRTF, the last element of NASA’s Great Observatories Program) is scheduled for launch in the summer of 2002 and will provide lower spatial resolution observations out to the far-infrared (which is a wavelength regime not observable with ground based telescopes). SIRTF observations, especially of nearby galaxies, will be a powerful tool for finding “giant hot core cluster” candidates. To this end, I will do I follow-up radio study of the galaxies in the SIRTF Legacy program SINGS (SIRTF Nearby Galaxy Survey, led by Dr. Robert Kennicutt) primarily accessing publicly available radio archive data.

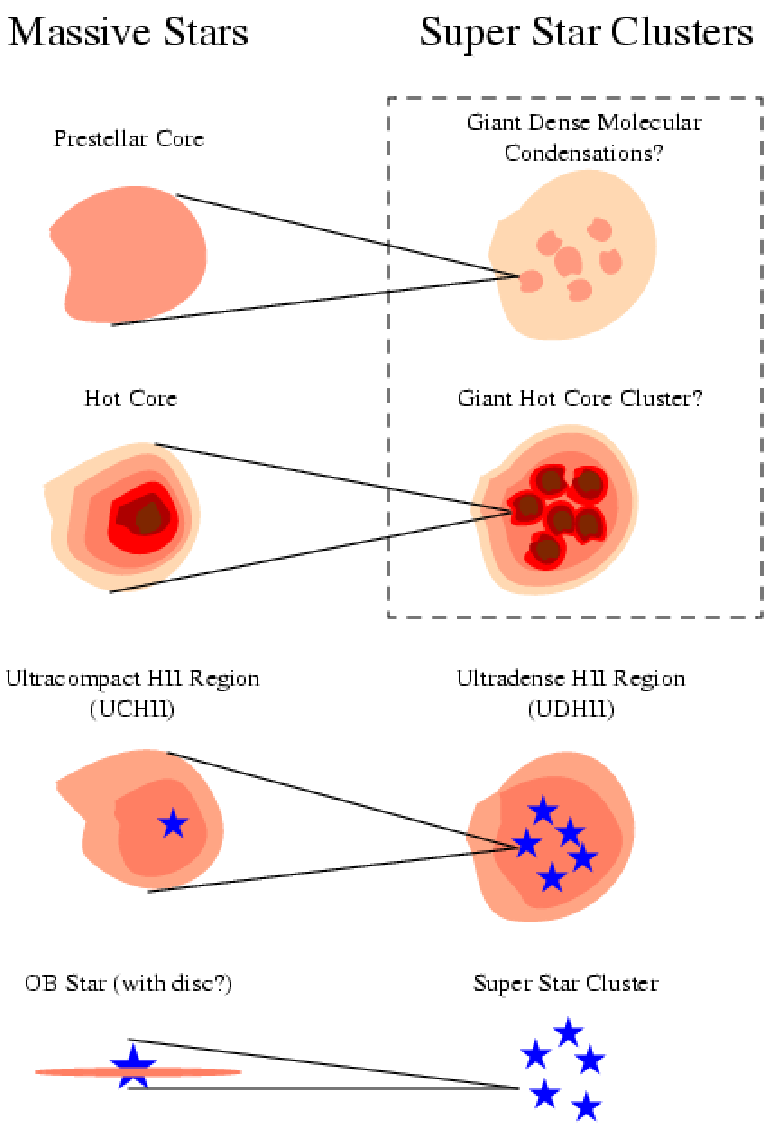

Figure 6.1: Proposed schematic illustrating the formation of massive star clusters (right) in parallel to the precepts of massive star formation (left) from Churchwell (1999). The dashed box indicates of cluster formation which have not yet been observationally identified.

6.5 Develop More Sophisticated Models

While the simple models presented in Chapters 4 and 5 are adequate for estimating mean physical properties, such as density, more sophisticated models would allow us to investigate the detailed dependence of observable quantities on varying physical conditions. More realistic models would need to include an arbitrary number of embedded stars (each with its own density profile and temperature distribution) embedded in a diffuse medium and allowed to evolve in time. Such models could predict the detailed dependence of observables such as the evolution of the spectral energy distribution of the enshrouding dust cocoon and the radio spectral index.

6.6 Summary of Future Possibilities

The origin of globular clusters has eluded researchers for many years, possibly because of the assumption that we would first need to able to observe the early universe in detail in order to find such objects. However, as we learned in Chapters 1 and 2 of this thesis, many young massive star clusters have been found with the Hubble Space Telescope in a number of systems, often in merging galaxies such as the famous Antennae. These clusters had to form *somehow*, *somewhere* in their host galaxies, and the most logical way to look for them is with the same methods used to find UCHII regions in our galaxy — radio, mm, and possibly in the far-IR. Indeed, perhaps we can even ask some of the same questions that we ask about UCH II regions. For example, is maser activity associated with UDH IIs? Do UDH IIs have the same "lifetime problem"? When stellar winds are established, how do they affect the birth environment? The first steps in understanding massive star cluster formation will be to catalog a larger sample of UDH IIs, map out their spectral energy distributions (in so far as current instrumentation will allow), and determine the physical properties of their birth environments. I look forward to providing updates on the progress of this reseach to the community in the coming years.

Ad astra per aspera

Bibliography

Afflerbach, A., Churchwell, E., Acord, J. M., Hofner, P., Kurtz, S., & Depree, C. G. 1996, ApJS, 106, 423

Allen, D. A., Wright, A. E., & Goss, W. M. 1976, MNRAS, 177, 91

Allen, M. L. & Kronberg, P. P. 1998, ApJ, 502, 218

Anantharamaiah, K. R., Viallefond, F., Mohan, N. R., Goss, W. M., & Zhao, J. H. 2000, ApJ, 537, 613

Arendt, R. G. 1989, ApJS, 70, 181

Arp, H. & Sandage, A. 1985, AJ, 90, 1163

Ashman, K. M. & Zepf, S. E. 1992, ApJ, 384, 50

Baas, F., Israel, F. P., & Koornneef, J. 1994, A&A, 284, 403

Balland, C., Silk, J., & Schaeffer, R. 1998, ApJ, 497, 541

Barnes, J. E. 1988, ApJ, 331, 699

—. 1989, Nature, 338, 123

Barnes, J. E. 1997, in ASP Conf. Ser. 116: The Nature of Elliptical Galaxies; 2nd Stromlo Symposium, 469+

Barnes, J. E. & Hernquist, L. 1992, Nature, 360, 715

—. 1996, ApJ, 471, 115

Barnes, J. E. & Hernquist, L. E. 1991, ApJL, 370, L65

Baron, E. & White, S. D. M. 1987, ApJ, 322, 585

Beck, S. C., Kelly, D. M., & Lacy, J. H. 1997, AJ, 114, 585

Beck, S. C., Turner, J. L., & Kovo, O. 2000, AJ, 120, 244

Bianchi, S., Davies, J. I., Alton, P. B., Gerin, M., & Casoli, F. 2000, A&A, 353, L13

Boulesteix, J., Courtes, G., Laval, A., Monnet, G., & Petit, H. 1974, A&A, 37, 33

Burgarella, D. & Chapelon, S. 1998, in ASP Conf. Ser. 133: Science With The NGST, 227

Buta, R., Crocker, D. A., & Byrd, G. G. 1999, AJ, 118, 2071

Calzetti, D., Kinney, A. L., & Storchi-Bergmann, T. 1994, ApJ, 429, 582

Carilli, C. L., Holdaway, M. A., Ho, P. T. P., & de Pree, C. G. 1992, ApJL, 399, L59

Cervino, M. & Mas-Hesse, J. M. 1994, A&A, 284, 749

Chandar, R., Bianchi, L., Ford, H. C., & Salasnich, B. 1999, PASP, 111, 794

Chu, Y. & Kennicutt, R. C. 1994, ApJ, 425, 720

Churchwell, E. 1999, in NATO ASIC Proc. 540: The Origin of Stars and Planetary Systems, 515

Clarke, C. J., Bonnell, I. A., & Hillenbrand, L. A. 2000, in Protostars and Planets IV, 151

Cohen, M., Walker, R. G., Carter, B., Hammersley, P., Kidger, M., & Noguchi, K. 1999, AJ, 117, 1864

Condon, J. J. 1992, ARA&A, 30, 575

Condon, J. J., Anderson, M. L., & Helou, G. 1991a, ApJ, 376

Condon, J. J., Huang, Z. ., Yin, Q. F., & Thuan, T. X. 1991b, ApJ, 378, 65

Condon, J. J. & Yin, Q. F. 1990, ApJ, 357, 97

Conti, P. S. 1991, ApJ, 377, 115

Conti, P. S. & Blum, R. 2001, ApJ, in press

Conti, P. S., Leitherer, C., & Vacca, W. D. 1996, ApJL, 461, L87

Conti, P. S. & Vacca, W. D. 1994, ApJL, 423, L97

Corbin, M. R., Korista, K. T., & Vacca, W. D. 1993, AJ, 105, 1313

Courtes, G., Petit, H., Petit, M., Sivan, J. P., & Dodonov, S. 1987, A&A, 174, 28

Cowie, L. L., Songaila, A., Kim, T., & Hu, E. M. 1995, AJ, 109, 1522

Crowther, P. A., Beck, S. C., Willis, A. J., Conti, P. S., Morris, P. W., & Sutherland, R. S. 1999, MNRAS, 304, 654

de Grijs, R., O'Connell, R. W., & Gallagher, J. S. 2001, AJ, 121, 768

de Marchi, G., Clampin, M., Greggio, L., Leitherer, C., Nota, A., & Tosi, M. 1997, ApJL, 479, L27

de Pree, C. G., Mehringer, D. M., & Goss, W. M. 1997, ApJ, 482, 307 de Pree, C. G., Rodriguez, L. F., & Goss, W. M. 1995, Revista Mexicana de Astronomia y Astrofisica, 31, 39

de Vaucouleurs, G. 1979, ApJ, 227, 729

de Vaucouleurs, G., de Vaucouleurs, A., & Corwin, H. G. 1976, 2nd reference catalogue of bright galaxies containing information on 4364 galaxies with reference to papers published between 1964 and 1975 (University of Texas Monographs in Astronomy, Austin: University of Texas Press, 1976)

Dove, J. B., Shull, J. M., & Ferrara, A. 2000, ApJ, 531, 846

Duc, P. . & Mirabel, I. F. 1994, A&A, 289, 83

Duric, N., Viallefond, F., Goss, W. M., & van der Hulst, J. M. 1993, A&AS, 99, 217

Elmegreen, B. G., Efremov, Y., Pudritz, R. E., & Zinnecker, H. 2000a, in Protostars and Planets IV, 179

Elmegreen, B. G. & Efremov, Y. N. 1997, ApJ, 480, 235

Elmegreen, B. G., Efremov, Y. N., & Larsen, S. 2000b, ApJ, 535, 748

Elmegreen, B. G., Kaufman, M., & Thomasson, M. 1993, ApJ, 412, 90

Elmegreen, D. M., Kaufman, M., Brinks, E., Elmegreen, B. G., & Sundin, M. 1995, ApJ, 453, 100

Fabian, A. C. 1994, ARA&A, 32, 277

Ferrara, A. & Tolstoy, E. 2000, MNRAS, 313, 291

Figer, D. F., Kim, S. S., Morris, M., Serabyn, E., Rich, R. M., & McLean, I. S. 1999, ApJ, 525, 750

Filipovic, M. D., Haynes, R. F., White, G. L., Jones, P. A., Klein, U., & Wielebinski, R. 1995, A&AS, 111, 311

Filipovic, M. D., Jones, P. A., White, G. L., & Haynes, R. F. 1998, A&AS, 130, 441

Filipovic, M. D., Jones, P. A., White, G. L., Haynes, R. F., Klein, U., & Wielebinski, R. 1997, A&AS, 121, 321

Forbes, D. A. & Hau, G. K. T. 2000, MNRAS, 312, 703

Freedman, W. L., Hughes, S. M., Madore, B. F., Mould, J. R., Lee, M. G., Stetson, P., Kennicutt, R. C., Turner, A., Ferrarese, L., Ford, H., Graham, J. A., Hill, R., Hoessel, J. G., Huchra, J., & Illingworth, G. D. 1994, ApJ, 427, 628

Freedman, W. L., Wilson, C. D., & Madore, B. F. 1991, ApJ, 372, 455

Gallagher, J. S., Hunter, D. A., & Tutukov, A. V. 1984, ApJ, 284, 544

Garcia-Gomez, C. & Athanassoula, E. 1991, A&AS, 89, 159

Gonzalez Delgado, R. M., Leitherer, C., Heckman, T., Lowenthal, J. D., Ferguson, H. C., & Robert, C. 1998, ApJ, 495, 698

Gordon, S. M., Duric, N., Kirshner, R. P., Goss, W. M., & Viallefond, F. 1999, ApJS, 120, 247

Gorjian, V., Turner, J. L., & Beck, S. C. 2001, AJ, in press

Gwinn, C. R., Moran, J. M., & Reid, M. J. 1992, ApJ, 393, 149

Harris, W. E. 1991, ARA&A, 29, 543

Harris, W. E. & Pudritz, R. E. 1994, ApJ, 429, 177

Heckman, T. M. 1997, in Star Formation Near and Far, 271

Heckman, T. M. 1998, in ASP Conf. Ser. 148: Origins, 127

Heckman, T. M. 2001, in ASP Conf. Ser.: Gas and Galaxy Evolution, in press

Heckman, T. M., Dahlem, M., Lehnert, M. D., Fabbiano, G., Gilmore, D., & Waller, W. H. 1995, ApJ, 448, 98

Henize, K. G. 1967, ApJS, 14, 125

Hernquist, L. 1992, ApJ, 400, 460

—. 1993, ApJ, 409, 548

Hernquist, L. & Spergel, D. N. 1992, ApJL, 399, L117

Hibbard, J. E. & Vacca, W. D. 1997, AJ, 114, 1741

Hickson, P. 1982, ApJ, 255, 382

Hickson, P., Mendes de Oliveira, C., Huchra, J. P., & Palumbo, G. G. 1992, ApJ, 399, 353

Hickson, P., Richstone, D. O., & Turner, E. L. 1977, ApJ, 213, 323

Hills, J. G. 1980, ApJ, 235, 986

Ho, L. C. & Filippenko, A. V. 1996a, ApJL, 466, L83

—. 1996b, ApJ, 472, 600

Hodge, P. W., Balsley, J., Wyder, T. K., & Skelton, B. P. 1999, PASP, 111, 685

Hollenbach, D., Johnstone, D., Lizano, S., & Shu, F. 1994, ApJ, 428, 654

Holtzman, J. A., Burrows, C. J., Casertano, S., Hester, J. J., Trauger, J. T., Watson, A. M., & Worthey, G. 1995a, PASP, 107, 1065

Holtzman, J. A., Faber, S. M., Shaya, E. J., Lauer, T. R., Grothe, J., Hunter, D. A., Baum, W. A., Ewald, S. P., Hester, J. F., Light, R. M., Lynds, C. R., O'Neil, E. J., & Westphal, J. A. 1992, AJ, 103, 691

Holtzman, J. A., Hester, J. J., Casertano, S., Trauger, J. T., Watson, A. M., Ballester, G. E., Burrows, C. J., Clarke, J. T., Crisp, D., Evans, R. W., Gallagher, J. S., Griffiths, R. E., Hoessel, J. G., Matthews, L. D., Mould, J. R., Scowen, P. A., Stapelfeldt, K. R., & Westphal, J. A. 1995b, PASP, 107, 156

Hunsberger, S. D., Charlton, J. C., & Zaritsky, D. 1996, ApJ, 462, 50+

—. 1998, ApJ, 505, 536

Hutsemekers, D. & Surdej, J. 1984, A&A, 133, 209

Hyman, S. D., Lacey, C. K., Weiler, K. W., & Van Dyk, S. D. 2000, AJ, 119, 1711

Iglesias-Paramo, J. & Vilchez, J. M. 1997, ApJ, 479, 190

Jenkins, E. B., Jura, M., & Loewenstein, M. 1983, ApJ, 270, 88

Johansson, I. 1987, A&A, 182, 179

Johnson, K. E., Leitherer, C., Vacca, W. D., & Conti, P. S. 2000, AJ, 120, 1273

Johnson, K. E., Vacca, W. D., Leitherer, C., Conti, P. S., & Lipscy, S. J. 1999, AJ, 117, 1708

Kawara, K., Nishida, M., & Phillips, M. M. 1989, ApJ, 337, 230

Kellermann, K. I., Sramek, R., Schmidt, M., Shaffer, D. B., & Green, R. 1989, AJ, 98, 1195

Kennicutt, R. C. 1984, ApJ, 287, 116

—. 1998, ApJ, 498, 541

Keto, E., Hora, J. L., Fazio, G. G., Hoffmann, W., & Deutsch, L. 1999, ApJ, 518, 183

Kim, S. S., Morris, M., & Lee, H. M. 1999, ApJ, 525, 228

Kobulnicky, H. A., Dickey, J. M., Sargent, A. I., Hogg, D. E., & Conti, P. S. 1995, AJ, 110, 116

Kobulnicky, H. A. & Johnson, K. E. 1999, ApJ, 527, 154

Kobulnicky, H. A., Kennicutt, R. C., & Pizagno, J. L. 1999, ApJ, 514, 544

Kobulnicky, H. A., Skillman, E. D., Roy, J., Walsh, J. R., & Rosa, M. R. 1997, ApJ, 477, 679

Kolatt, T. S., Bullock, J. S., Somerville, R. S., Sigad, Y., Jonsson, P., Kravtsov, A. V., Klypin, A. A., Primack, J. R., Faber, S. M., & Dekel, A. 1999, ApJL, 523, L109

Krist, J. 1993, in ASP Conf. Ser. 52: Astronomical Data Analysis Software and Systems II, Vol. 2, 536

Kuehr, H., Witzel, A., Pauliny-Toth, I. I. K., & Nauber, U. 1981, A&AS, 45, 367

Kunth, D., Mas-Hesse, J. M., Terlevich, E., Terlevich, R., Lequeux, J., & Fall, S. M. 1998, A&A, 334, 11

Kunth, D. & Schild, H. 1986, A&A, 169, 71

Kurtz, S., Cesaroni, R., Churchwell, E., Hofner, P., & Walmsley, C. M. 2000, in Protostars and Planets IV, 299

Lacey, C., Duric, N., & Goss, W. M. 1997, ApJS, 109, 417

Larsen, S. S. & Richtler, T. 1999, A&A, 345, 59

Lasker, B. M., Sturch, C. R., McLean, B. J., Russell, J. L., Jenkner, H., & Shara, M. M. 1990, AJ, 99, 2019

Leitherer, C. & Heckman, T. M. 1995, ApJS, 96, 9

Leitherer, C., Robert, C., & Heckman, T. M. 1995, ApJS, 99, 173

Leitherer, C., Schaerer, D., Goldader, J. D., Delgado, R. M. G., Robert, C., Kune, D. F., de Mello, D. F., Devost, D., & Heckman, T. M. 1999, ApJS, 123, 3

Lowenthal, J. D., Koo, D. C., Guzman, R., Gallego, J., Phillips, A. C., Faber, S. M., Vogt, N. P., Illingworth, G. D., & Gronwall, C. 1997, ApJ, 481, 673

Méndez, D. I., Esteban, C., Filipović , M. D., Ehle, M., Haberl, F., Pietsch, W., & Haynes, R. F. 1999, A&A, 349, 801

Mac Low, M. & Ferrara, A. 1999, ApJ, 513, 142

Madau, P., Haardt, F., & Rees, M. J. 1999, ApJ, 514, 648

Madau, P. & Shull, J. M. 1996, ApJ, 457, 551+

Madden, S. C. 2000, New Astronomy Review, 44, 249

Maeder, A. & Conti, P. S. 1994, ARA&A, 32, 227

Marlowe, A. T., Heckman, T. M., Wyse, R. F. G., & Schommer, R. 1995, ApJ, 438, 563

Massey, P., Bianchi, L., Hutchings, J. B., & Stecher, T. P. 1996, ApJ, 469, 629

Massey, P. & Hunter, D. A. 1998, ApJ, 493, 180

Massey, P., Johnson, K. E., & Degioia-Eastwood, K. 1995, ApJ, 454, 151

McKee, C. F. & Williams, J. P. 1997, ApJ, 476, 144

Meurer, G. R., Freeman, K. C., Dopita, M. A., & Cacciari, C. 1992, AJ, 103, 60

Meurer, G. R., Heckman, T. M., Lehnert, M. D., Leitherer, C., & Lowenthal, J. 1997, AJ, 114, 54

Meurer, G. R., Heckman, T. M., Leitherer, C., Kinney, A., Robert, C., & Garnett, D. R. 1995, AJ, 110, 2665

Meylan, G. 1993, in ASP Conf. Ser. 48: The Globular Cluster-Galaxy Connection, 588+

Mezger, P. G. & Henderson, A. P. 1967, ApJ, 147, 471

Mezger, P. G., Schraml, J., & Terzian, Y. 1967, ApJ, 150, 807

Mihos, J. C. & Hernquist, L. 1996, ApJ, 464, 641

Miller, B. W., Whitmore, B. C., Schweizer, F., & Fall, S. M. 1997, AJ, 114, 2381

Mirabel, I. F., Dottori, H., & Lutz, D. 1992, A&A, 256, L19

Mirabel, I. F., Lutz, D., & Maza, J. 1991, A&A, 243, 367

Mohan, N., Anantharamaiah, K., & Goss, W. 2001, ApJ

Nagar, N. M., Falcke, H., Wilson, A. S., & Ho, L. C. 2000, ApJ, 542, 186

O'Connell, R. W., Gallagher, J. S., Hunter, D. A., & Colley, W. N. 1995, ApJL, 446, L1

Pettini, M., Steidel, C. C., Adelberger, K. L., Dickinson, M., & Giavalisco, M. 2000, ApJ, 528, 96

Phillips, M. M., Aitken, D. K., & Roche, P. F. 1984, MNRAS, 207, 25

Rubin, V. C., Hunter, D. A., & Ford, W. K. J. 1990, ApJ, 365, 86

Sandage, A., Saha, A., Tammann, G. A., Labhardt, L., Schwengeler, H., Panagia, N., & Macchetto, F. D. 1994, ApJL, 423, L13

Sandage, A. & Tammann, G. A. 1981, A revised Shapley-Ames Catalog of bright galaxies (Washington: Carnegie Institution, 1981, Preliminary version)

Sanders, D. B. & Mirabel, I. F. 1996, ARA&A, 34, 749

Sargent, A. & Scoville, N. 1991, ApJL, 366, L1

Sargent, W. L. W. & Searle, L. 1970, ApJL, 162, L155

Sauvage, M., Thuan, T. X., & Lagage, P. O. 1997, A&A, 325, 98

Schaerer, D., Contini, T., & Kunth, D. 1999a, A&A, 341, 399

Schaerer, D., Contini, T., & Pindao, M. 1999b, A&AS, 136, 35

Schlegel, D. J., Finkbeiner, D. P., & Davis, M. 1998, ApJ, 500, 525

Schweizer, F. 1982, ApJ, 252, 455

Schweizer, F., Miller, B. W., Whitmore, B. C., & Fall, S. M. 1996, AJ, 112, 1839

Schwering, P. B. W. & Israel, F. P. 1990, Atlas and catalogue of infrared sources in the Magellanic Clouds (Dordrecht: Kluwer, 1990, edited by Schwering, P.B.W.; Israel, F.P.)

Secker, J. 1992, AJ, 104, 1472

Selman, F., Melnick, J., Bosch, G., & Terlevich, R. 1999, A&A, 347, 532

Shu, F. H. 1991, The physics of astrophysics. Vol.1: Radiation (A Series of Books in Astronomy, Mill Valley, CA: University Science Books, 1991)

Sirianni, M., Nota, A., Leitherer, C., De Marchi, G., & Clampin, M. 2000, ApJ, 533, 203

Smith, L. F., Mezger, P. G., & Biermann, P. 1978, A&A, 66, 65

Smith, L. J. & Gallagher, J. S. 2001, MNRAS

Smith, T. R. & Kennicutt, R. C. 1989, PASP, 101, 649

Sohn, Y. & Davidge, T. J. 1996, AJ, 112, 2559

Soifer, B. T., Boehmer, L., Neugebauer, G., & Sanders, D. B. 1989, AJ, 98, 766

Steidel, C. C., Giavalisco, M., Pettini, M., Dickinson, M., & Adelberger, K. L. 1996, ApJL, 462, L17

Sugai, H. & Taniguchi, Y. 1992, AJ, 103, 1470

Takahashi, K. & Portegies Zwart, S. F. 2000, ApJ, 535, 759

Tarchi, A., Neininger, N., Greve, A., Klein, U., Garrington, S. T., Muxlow, T. W. B., Pedlar, A., & Glendenning, B. E. 2000, A&A, 358, 95

Telesco, C. M., Dressel, L. L., & Wolstencroft, R. D. 1993, ApJ, 414, 120

Tokunaga, A. T. 1984, AJ, 89, 172

Toomre, A. 1964, ApJ, 139, 1217

Tumlinson, J., Giroux, M. L., Shull, J. M., & Stocke, J. T. 1999, AJ, 118, 2148

Turner, J. L., Beck, S. C., & Ho, P. T. P. 2000, ApJL, 532, L109

Turner, J. L. & Ho, P. T. P. 1985, ApJL, 299, L77

Turner, J. L., Ho, P. T. P., & Beck, S. C. 1998, AJ, 116, 1212

Ulvestad, J. S. & Antonucci, R. R. J. 1997, ApJ, 488, 621

Urry, C. M. & Padovani, P. 1995, PASP, 107, 803

Vacca, W. D. 1994, ApJ, 421, 140

Vacca, W. D. 1997, in The Ultraviolet Universe at Low and High Redshift: Probing the Progress of Galaxy Evolution, 21

Vacca, W. D. & Conti, P. S. 1992, ApJ, 401, 543

Vacca, W. D., Garmany, C. D., & Shull, J. M. 1996, ApJ, 460, 914

Vacca, W. D., Robert, C., Leitherer, C., & Conti, P. S. 1995, ApJ, 444, 647

van Breugel, W. J. M., Stanford, S. A., Spinrad, H., Stern, D., & Graham, J. R. 1998, ApJ, 502, 614

van den Bergh, S. 1971, A&A, 12, 474

—. 1995, Nature, 374, 215

van der Kruit, P. C. 1971, A&A, 15, 110

Vanhala, H. A. T. & Cameron, A. G. W. 1998, ApJ, 508, 291

Venkatesan, A., Giroux, M. L., & Shull, J. M. 2001, ApJ

Verschueren, W. 1990, A&A, 234, 156

Ward-Thompson, D. & Robson, E. I. 1990, MNRAS, 244, 458

Watson, A. M., Gallagher, J. S., Holtzman, J. A., Hester, J. J., Mould, J. R., Ballester, G. E., Burrows, C. J., Casertano, S., Clarke, J. T., Crisp, D., Evans, R., Griffiths, R. E., Hoessel, J. G., Scowen, P. A., Stapelfeldt, K. R., Trauger, J. T., & Westphtptphal, J. A. 1996, AJ, 112, 534

Weiler, K. W. & Panagia, N. 1978, A&A, 70, 419

Weiler, K. W., Sramek, R. A., Panagia, N., van der Hulst, J. M., & Salvati, M. 1986, ApJ, 301, 790

Whitmore, B. 2000, in ASP Conf. Ser. 197: Dynamics of Galaxies: from the Early Universe to the Present, 315

Whitmore, B. C. 1999, in IAU Symp. 186: Galaxy Interactions at Low and High Redshift, Vol. 186, 251

Whitmore, B. C. & Schweizer, F. 1995, AJ, 109, 960

Whitmore, B. C., Schweizer, F., Leitherer, C., Borne, K., & Robert, C. 1993, AJ, 106, 1354

Whitmore, B. C., Zhang, Q., Leitherer, C., Fall, S. M., Schweizer, F., & Miller, B. W. 1999, AJ, 118, 1551

Williams, B. A., McMahon, P. M., & van Gorkom, J. H. 1991, AJ, 101, 1957

Williams, R. E., Blacker, B., Dickinson, M., Dixon, W. V. D., Ferguson, H. C., Fruchter, A. S., Giavalisco, M., Gilliland, R. L., Heyer, I., Katsanis, R., Levay, Z., Lucas, R. A., McElroy, D. B., Petro, L., Postman, M., Adorf, H., & Hook, R. 1996, AJ, 112, 1335

Wood, D. O. S. & Churchwell, E. 1989a, ApJ, 340, 265

—. 1989b, ApJS, 69, 831

Woosley, S. E. & Weaver, T. A. 1995, ApJS, 101, 181

Wray, J. D. 1988, The color atlas of galaxies (Research supported by NSF,. Cambridge and New York, Cambridge University Press, 1988, 201 p.)

Zepf, S. E., Ashman, K. M., English, J., Freeman, K. C., & Sharples, R. M. 1999, AJ, 118, 752

Zhang, Q., Fall, S. M., & Whitmore, B. C. 2000, in American Astronomical Society Meeting, Vol. 197, 2406

Appendix A

UCH II Candidates in the Magellanic Clouds

In the Galaxy, UCH IIs have been identified by their thermal radio spectra and their IRAS colors. Just as the UDH IIs discussed in Chapters 4 and 5 have flat or inverted radio spectra at cm wavelengths, individual UCH IIs are expected to have thermal radio spectral energy distributions as well. However, in the catalog of UCH II regions by Wood & Churchwell (1989b), many of the UCH II regions have radio spectral indices consistent with optically thin thermal free-free emission. Wood & Churchwell (1989a) also found that UCH IIs in the Galaxy strictly obey a set of color criteria in the infrared with $log(F_{60\mu m}/F_{12\mu m}) \geq 1.30$ and $log(F_{25\mu m}/F_{12\mu m}) \geq 0.57$, while very few other types of objects had IRAS colors fitting these criteria. For example, in the sample of Arendt (1989), none of the SNR meet both of these criteria. Therefore, these color criteria appear to be relatively robust for identifying UCH II regions. Wood & Churchwell (1989b) also note that 60% of the brightest IRAS sources ($> 10^4$ Jy at 100 μm) in the range of their survey are UCH II regions. Therefore, we expect UCH II regions to be among the brightest mid- to far-infrared sources in the Magellanic Clouds.

The radio observations used in this appendix were originally obtained by Filipovic et al. (1995, 1997) using the Parkes radio telescope. The beamsize at the frequencies used here are 3.6 arcmin at 8.85 GHz, 5.2 arcmin at 4.85 GHz, and 5.6 at 4.75 GHz. These beamsizes are large compared to the expected size of a UCH II region in the Magellanic Clouds of $\lesssim 0.5$ arcsec. Consequently, these observations are likely to suffer from severe contamination by other radio emitting objects and background radio continuum. The RMS noise for these frequencies was typically $\sim$ 8 mJy/beam, and the flux uncertainties are typically $\sim$ 10%. The infrared observations used in this chapter were taken with the Infrared Astronomical Satellite (IRAS) and published in Schwering & Israel (1990). The IRAS beamsizes are similar to those of the radio observations, with the 12 μm beam ~ 3.7 arcmin. However, unlike their radio fluxes, the IRAS fluxes of UCH II regions should be among the brightest in the Magellanic Clouds, and therefore contamination by other mid- to far-IRAS sources is not likely to be as severe, although we might expect to find *multiple* UCH II regions within a single IRAS beam. The uncertainties in the IRAS fluxes are estimated to be $\sim 10 - 20\%$.

Using these color standards, I have utilized previously published radio data on the Magellanic Clouds in combination with the IRAS Point Source Catalog to identify UCH II region candidates. The data in Filipovic et al. (1998) was used to select objects in the Magellanic Clouds detected in both radio and IRAS observations. These objects were compared to the IRAS colors in order to create the list of objects satisfying both detected in the radio and meeting the IRAS color criteria. It should be noted that *only* objects first identified as radio sources were considered in this process. This process resulted in 56 UCH II region candidates in the LMC and 11 candidates in the SMC which were both detected in radio observations *and* have IRAS colors meeting the selection criteria. The $log(F_{60\mu m}/F_{12\mu m})$ and $log(F_{25\mu m}/F_{12\mu m})$ values are plotted in Figures A.1 and A.2. These sources are listed in Tables A.1 and A.2 along with their radio fluxes. Given the strong contamination possible in the radio observations, I have not imposed a standard on the radio spectral index α as in Chapters 4 and 5. Of the 56 sources in the LMC, only 21 have one or both of the radio indices $\alpha^{8.55GHz}_{4.85GHz}$ or $\alpha^{8.55GHz}_{4.75GHz} \geq -0.1$. For the SMC, only 5 of the 11 sources have $\alpha^{8.55GHz}_{4.85GHz}$ or $\alpha^{8.55GHz}_{4.75GHz} \geq -0.1$.

In order to improve the knowledge of these sources, I have begun an observing campaign with the Australia Telescope Compact Array (ATCA), which is currently the only telescope available which can observe the Magellanic Clouds at sufficient spatial resolution ($1'' - 2''$, two orders of magnitude better than the existing observations presented here). In addition, the upcoming Space Infrared Satellite Facility (SIRTF, scheduled to launch in 2002), will provide higher resolution mid- to far-infrared data on these sources.

Table A.1: UCH II candidates in the LMC.

IRAS ID	100 μm Jy	60 μm Jy	25 μm Jy	12 μm Jy	4.75 GHz mJy	4.85 GHz mJy	8.55 GHz mJy
0449-6917	139.4	62.1	7.99	1.74	0.25	0.32	0.24
0452-6700	191.4	116.7	13.99	3.63	0.22	0.36	0.25
0452-6722	—	10.3	0.78	0.19	0.096	0.079	0.083
0452-6727	353.6	343.6	65.16	9.1	—	—	—
0453-6807	60.3	35.6	4.16	1.0	0.16	0.14	0.13
0454-6716	27.0	8.3	0.5	0.37	0.3	0.28	0.46
0454-6916	280.8	178.	17.2	4.25	0.54	0.87	0.46
0456-6629	520.	244.3	32.74	4.25	2.1	3.4	1.5
0456-6636	93.6	37.3	4.0	0.96	0.68	0.65	1.2
0457-6830	228.8	118.	12.88	2.81	0.45	0.61	0.4
0457-6849	97.8	47.6	4.99	1.26	0.12	0.12	0.12
0458-6626	62.4	33.1	3.88	0.81	0.31	0.27	0.23
0459-6620	20.8	8.3	1.66	0.33	0.081	0.083	—
0503-6722	77.	31.9	3.66	0.93	0.09	0.064	—
0505-6659	43.7	31.9	7.66	0.59	0.11	0.11	0.094
0505-6807	54.1	25.3	2.11	0.41	0.31	0.29	0.35
0505-7010	52.	24.8	2.55	0.59	0.21	0.24	—
0505-7058	85.3	62.9	11.77	1.55	0.064	0.064	0.045
0510-6857	447.2	314.6	52.17	7.14	1.2	1.2	1.1
0513-6729	112.3	60.9	9.43	1.33	0.19	0.2	0.16
0513-6925	301.6	256.7	41.07	6.03	0.64	0.78	0.51
0516-6722	39.5	27.3	2.55	0.37	0.042	0.033	—
0519-6941	249.6	124.2	11.1	2.96	0.87	1.2	—
0520-6655	39.5	27.3	2.55	0.37	0.042	0.033	—
0522-6757	52.	70.4	4.55	1.11	0.24	—	0.16
0522-6800	312.	246.3	32.19	3.96	1.1	2.1	0.77
0523-6806	104.	89.	16.65	3.14	0.58	0.6	0.4
0523-7138	35.4	9.1	1.0	0.26	0.18	0.16	—
0525-6618	228.8	91.1	14.1	2.4	1.2	1.3	1.2
0525-6831	83.2	39.3	4.88	1.11	0.29	0.26	0.39
0526-6731	20.8	8.3	1.44	0.22	1.7	1.2	1.5
0526-6740	20.8	11.6	1.0	0.22	0.38	0.29	0.36
0526-6751	18.7	4.6	0.22	0.26	0.16	0.098	0.15
0528-6730	62.4	41.4	5.22	0.74	0.56	0.5	0.4
0531-7106	243.4	105.6	12.32	2.22	1.1	1.6	0.86
0532-6629	224.6	83.6	6.88	1.07	0.41	0.5	0.31
0532-6743	280.8	113.8	8.88	1.78	0.77	1.1	0.84
0532-6826	62.4	31.9	3.88	0.93	—	—	0.074
0533-6948	87.4	70.4	8.88	1.33	—	0.12	0.096
0534-6847	106.1	64.2	6.88	1.41	0.16	0.14	0.068
0535-6603	97.2	43.3	6.39	1.25	0.7	1.1	0.4

Table A.1: continued.

IRAS ID	100 μm Jy	60 μm Jy	25 μm Jy	12 μm Jy	4.75 GHz mJy	4.85 GHz mJy	8.55 GHz mJy
0535-6736	384.8	265.	35.3	4.74	1.4	2.3	1.3
0536-6735	—	33.1	4.22	0.44	—	—	0.11
0536-6941	208.	78.7	9.99	2.59	0.49	0.48	0.37
0537-6914	104.	41.4	3.33	1.04	—	—	1.5
0538-6911	312.	124.2	22.2	2.96	3.6	—	3.1
0538-7042	74.9	41.4	5.11	1.29	0.14	0.16	0.18
0539-6907	3120.	2794.5	471.75	74.	36.	36.	35.0
0539-6931	312.	248.4	31.08	4.44	1.3	—	1.4
0540-6927	—	41.4	2.77	0.74	—	—	0.27
0540-6940	769.6	662.4	111.	14.98	1.9	1.9	1.7
0540-6946	624.	414.	33.3	4.07	4.2	4.0	4.0
0540-7111	141.4	61.7	8.66	2.	0.081	0.087	0.081
0542-7121	124.8	53.	5.22	1.15	0.26	0.35	0.19
0543-6752	20.8	12.	1.33	0.3	0.25	0.29	0.28
0545-6947	33.3	33.1	4.44	0.56	0.079	0.06	0.084
0549-7004	208.	58.4	4.99	0.96	0.7	0.74	0.55

Table A.2: UCH II candidates in the SMC.

IRAS ID	100 μm Jy	60 μm Jy	25 μm Jy	12 μm Jy	4.75 GHz mJy	4.85 GHz mJy	8.55 GHz mJy
0043-7321	27.	14.	0.89	0.22	0.078	0.09	0.13
0046-7333	128.	56.	9.77	1.07	0.24	0.26	0.41
0047-7343	27.	14.	1.11	0.19	—	0.046	0.079
0050-7329	27.	9.7	0.71	0.19	0.13	0.095	—
0056-7254	17.	9.1	0.78	0.19	0.12	—	—
0057-7226	242.	200.	43.5	5.99	1.6	1.6	1.5
0103-7216	59.	45.	10.9	1.37	0.18	0.17	0.18
0107-7327	27.	18.	2.55	0.44	0.086	0.064	0.051
0112-7333	117.	46.	2.22	0.52	0.5	0.53	0.4
0113-7334	88.	32.	2.22	0.33	—	—	0.38
0122-7324	46.	55.	22.9	2.21	0.12	0.12	—

Figure A.1: The values of the $log(F_{60\mu m}/F_{12\mu m})$ and $log(F_{25\mu m}/F_{12\mu m})$ color selection for the UCH II region candidates in the LMC.

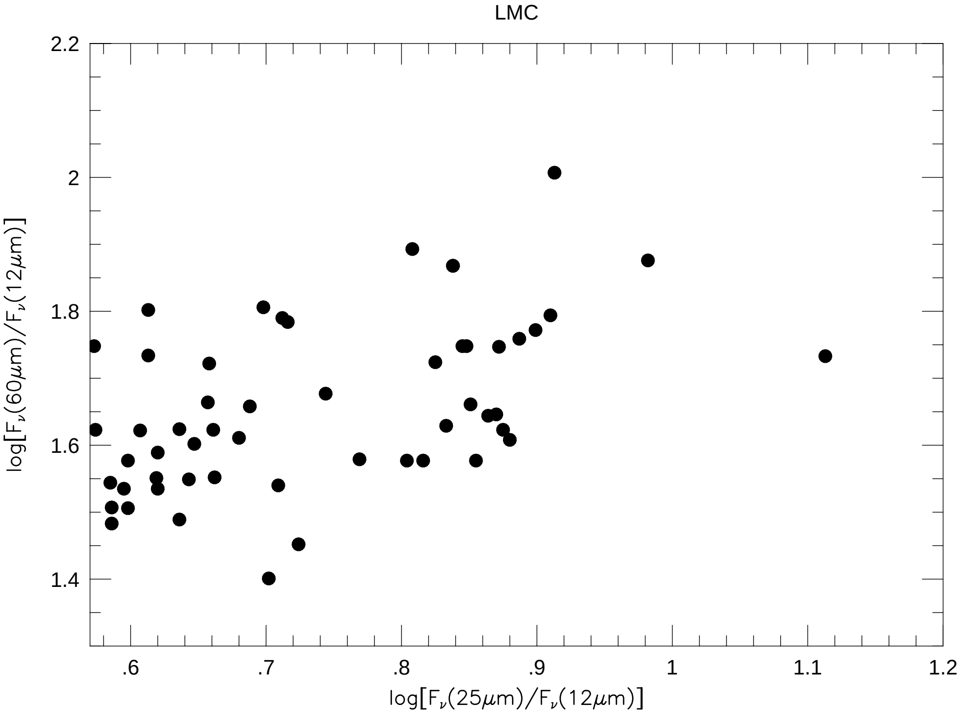

Figure A.2: The values of the $log(F_{60\mu m}/F_{12\mu m})$ and $log(F_{25\mu m}/F_{12\mu m})$ color selection for the UCH II region candidates in the SMC.